INNWIND.EU
D4.2.4: Results of wave tank tests

Description of Floating Wind Model Tests at ECN and DHI
(09/2014 - 01/2015)

Second Submission

Agreement n.:	308974
Duration	November 2012 – October 2017
Co-ordinator:	DTU Wind

Document information

Document Name:	D4.2.4: Results of wave tank tests
Document Number:	Deliverable D4.2.4
Author:	José Azcona, Frank Lemmer (né Sandner), Denis Matha, Florian Amann, Carlo Luigi Bottasso, Pierluigi Montinari, Petros Chassapoyannis, Konstantinos Diakakis, Spyros Voutsinas, Ricardo Pereira, Henrik Bredmose, Robert Mikkelsen, Robert Laugesen and Anders Mandrup Hansen
Document Type	Report
Dissemination level	PU
Review:	V2
Date:	July 31, 2016
WP:	4
Task:	4.2
Approval:	Approved by Task Leader

INNWIND.EU D4.2.4: Floating Wind Model Tests at ECN and DHI

TABLE OF CONTENTS

INNWIND.EU D4.2.4: Floating Wind Model Tests at ECN and DHI

INNWIND.EU D4.2.4: Floating Wind Model Tests at ECN and DHI

INNWIND.EU D4.2.4: Floating Wind Model Tests at ECN and DHI

Nomenclature

DOF	Degree of freedom
FOWT	Floating offshore wind turbine
RNA	Rotor-nacelle assembly
SWL	Still water level

1. INTRODUCTION

The task 4.2 of the INNWIND.EU project is called "Verification and Validation of Design Methods for Floating Structures". The main goal of this task is to validate the existing numerical codes for floating support structures by wave tank tests.

In previous deliverables of the task, the state of development and the capabilities of a set of tools for the analysis and simulation of floating wind turbines were documented [1]. In addition, methods and laws for performing scaled tests were developed, discussed and validated in Deliverable 4.22 [2].

The present deliverable provides a description of the water tank tests that have been performed as part of the activities of task 4.2. This document includes information about the different aspects of the tests as: characteristics of the real scaled floating platform and wind turbine, the scaling rules applied the layout of the tests, the characteristics of the facility, the test load cases and an overview of the test campaign results. The deliverable also presents the database where all the results are stored and how they are accessible and structured. The objective of these tests is the validation of the tools that the task participants are developing in the range of 10MW wind turbines. The results of this validation will be presented in Deliverable 4.25.

Two test campaigns have been carried out during 2014 and 2015 as part of the task 4.2 activities. Together, the campaigns cover tests with two different floater types which are dynamically different, two different methods for aerodynamic forcing, and a large range of wind-wave conditions.

The first test campaign is presented in Chapter 2 and took place at the *LHEEA - Research Laboratory in Hydrodynamics, Energetics and Atmospheric Environment* of the Ecole Centrale de Nantes (ECN) in France. A scaled model of a 10MW wind turbine with a semi-submersible floating substructure has been built at the University of Stuttgart and tested together with a Froude-scaled wind turbine model, built at Politecnico di Milano and also a real-time controlled ducted fan, built by CENER, which simulates the thrust force and works without an external wind generation system.

The second test campaign is described in Chapter 3 and was performed by DTU at the testing facilities of DHI (Danish Hydraulic Institute) in Denmark. In this case, a Froude–scaled rotor model of the INNWIND.EU 10MW wind turbine was installed on a TLP (Tension Leg Platform) floating substructure. The campaign thus extended the results of the first campaign with the modelling of an alternative and dynamically different floater, and tests for directionally spread wave conditions, misaligned wind/ waves and extreme waves.

Chapter 4 presents the experiments executed by CENER at ECN with an isolated submerged chain. The chain was excited with horizontal motions at the fairlead and the tension and also the motion of several markers located in different positions along the line were measured. The purpose of this experiment is the validation of mooring lines dynamics codes.

The denotation "ideal" and "real" in this report refer to the correctly scaled values and the values achieved after model building, respectively.

The data of all these experiments are available at a database prepared by the University of Stuttgart that is described in Chapter 5.

All the partners involved in this deliverable have contributed to different chapters although there has been a leader for each section of the document. The coordination and editing of the deliverable has been performed by CENER. Chapter 2 has been coordinated by the University of Stuttgart and CENER with contributions from DTU, NTUA, POLIMI and GL-RC. NTUA has performed the validation of the scaled model characteristics and GL-RC has contributed with the discussion and definition of the test cases. Chapter 3 has been written by DTU. CENER has written Chapter 4 and the University of Stuttgart has written Chapter 5. The Annex in Chapter 6 has been prepared by DTU.

2. SEMISUBMERSIBLE TEST CAMPAIGN

This campaign consisted of 4 testing weeks (divided in two different time slots) at the *LHEEA - Research Laboratory in Hydrodynamics, Energetics and Atmospheric Environment* of the Ecole Centrale de Nantes (ECN) wave tank. The tests at *LHEEA* were performed between September and November 2014.

The scaled model tested in this campaign represents a 10MW semisubmersible floating wind turbine. As currently there are no publicly existing designs of floating platforms for 10MW wind turbines, a 10MW model was developed based on the upscaling of a 5MW model. Therefore, the campaign will allow accomplishing the objectives of the task based on a large floating wind turbine with an upscaled semi-submersible platform. The development of an optimized 10MW design is part of the task 4.3 and is scheduled for a later stage of the project.

The 10MW platform model is based on the OC4-DeepCWind design [3]. It is composed by a central column with structural function and three columns located at a certain distance from the platform center, one upwind and two downwind, which provide the stability of the platform. Each of these columns has a heave plate at the bottom to damp the vertical platform motion. Figure 1 shows a sketch of the floating offshore substructure and wind turbine.

2.1 Coordinate Systems

The main body-fixed coordinate system used in this test campaign is fixed to the (ideal) overall center of mass of the floating offshore wind turbine (FOWT) system, see Figure 1. The location of the center of mass for the rotor-nacelle assembly (RNA) depends on the rotor system used during the tests, see Section 2.5 and Section 2.6. However, the ballast inside the outer columns was always adjusted so that the vertical location of the model center of mass matches with the ideal center of mass of the overall system, in all the cases and scaled model configurations. This applies also for the platform-only tests in week 1, see Section 2.11.
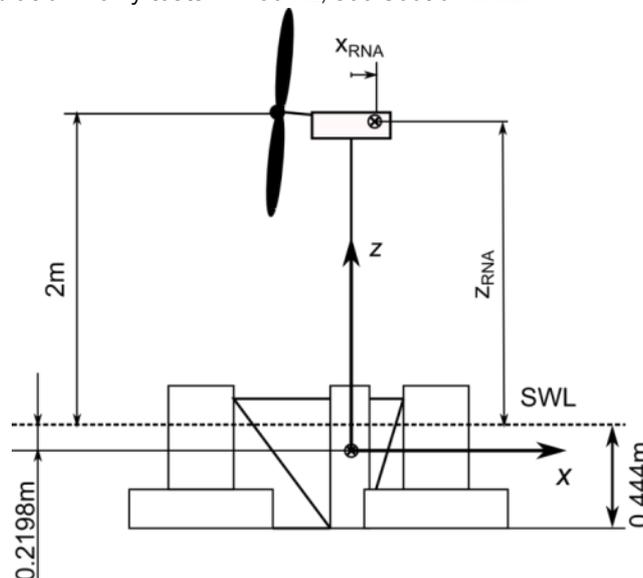
Figure 1 – FOWT sketch with body-fixed coordinate system at overall center of mass.

The columns, fairleads and lines are numbered according to the convention in [3] as follows: the upwind column has number 2; looking downwind, the left column is number 1 and the right column is number 3.

2.2   Scaling Laws

When a scaled model of a floating wind turbine is set up for an experiment, the purpose is to obtain an equivalent dynamic behaviour between the model and the full scale system. To keep this dynamic similarity on a floating rigid body, the ratio between inertial, gravitational and viscous forces must be conserved. The Froude number is defined as the ratio between inertial and gravitational forces, and it reads as:

$$Fr = \frac{u^2}{gl} \tag{1}$$

Where u is the characteristic velocity, g is the gravity and l is a characteristic length.
Froude scaling is discussed in detail in references [2], [4] and [5]. A deduction of the scaling factors for different parameters such as mass, inertia, or time, as they were applied to the model in this campaign is included in Annex I. These scaling laws take into account the different water densities for the prototype (salt water) ρ_{wp} and the model (sweet water) ρ_{wm}. Table 1 summarizes the different factors applied to each parameter. For the coefficient for the compensation of the different water densities, $\frac{\rho_{wp}}{\rho_{wm}}$, it has been assumed a salt water density, ρ_{wp} , of 1025 kg/m³ and a sweet water density, ρ_{wm}, of 998.2kg/m³.

Table 1 - Froude Scaling Factors, [5]

Property	Scaling Factor
Length	λ
Mass	$\frac{\rho_{wp}}{\rho_{wm}}\lambda^3$
Mass moment of inertia	$\frac{\rho_{wp}}{\rho_{wm}}\lambda^5$
Velocity	$\sqrt{\lambda}$
Acceleration	1
Time	$\sqrt{\lambda}$
Frequency	$\frac{1}{\sqrt{\lambda}}$
Force	$\frac{\rho_{wp}}{\rho_{wm}}\lambda^3$
Moment	$\frac{\rho_{wp}}{\rho_{wm}}\lambda^4$
Stiffness	$\frac{\rho_{wp}}{\rho_{wm}}\lambda$
Power	$\frac{\rho_{wp}}{\rho_{wm}}\lambda^{7/2}$
Thrust coefficient	$\frac{\rho_{wp}}{\rho_{wm}}$

INNWIND.EU D4.2.4: Floating Wind Model Tests at ECN and DHI

For the platform this means that the correctly scaled mass distribution needs to be obeyed when designing the model in order to achieve a correct center of mass and correct mass moments of inertia. For the rotor the same holds and additionally the rotational frequency has to be scaled correctly as well as the wind speed, which yields a constant tip-speed ratio if the rotor radius scaling is maintained. The platform and the rotor are considered rigid. The tower has certain flexibility and its natural frequencies have been estimated in Section 2.4.

As the scaling of forces is the central objective for this test the thrust force needs to scale correctly in order to introduce the correct aerodynamic forces into the floating system. The Reynolds number is defined as the ratio between inertial and viscous forces:

$$Re = \frac{ul}{\mu} \qquad\qquad (2)$$

Where μ is the kinematic viscosity. Aerodynamic forces similarity can be guaranteed by keeping the Reynolds number constant. However, it is generally not possible to keep the Reynolds number constant when Froude scaling is applied. This conflict causes that the aerodynamic forces on the scaled rotor are not representative of the full scale rotor if Froude scale is directly applied. In consequence, an alternative solution has to be found. This is explained in more detail in Chapter 2.5.

2.3 Platform Scaled Model

2.3.1 General Characteristics

As has been already mentioned, the platform geometry and mass distribution is aligned with the OC4-DeepCwind semi-submersible, see [3], if a scaling factor of $\lambda = 45$ were applied. The platform design has been upscaled to hold the 10MW INNWIND.EU wind turbine. The scale factor used in the tests for this 10MW system is 1/60. Table 2 shows the main mass and inertial properties of the baseline design in which our 10MW floating platform is based, the upscaled properties for the 10MW platform design and also the ideal properties for the scaled model.

Table 2 – Baseline design, 10MW prototype and scaled model ideal properties

Target Property	Baseline 5MW Prototype	10MW Prototype	Scaled Model	
Overall mass, including ballast	1.41E7	3.34E7	150.39	Kg
Platform mass, including ballast	1.348E7	3.20E7	144.06	Kg
Overall CM location below SWL	9.893	13.19	0.22	m
System roll inertia about overall CM	1.13E10	4.76E10	59.64	kgm^2
System pitch inertia about overall CM	1.13E10	4.76E10	59.64	kgm^2
System yaw inertia about overall CM	1.23E10	5.18E10	64.91	kgm^2

In order to achieve the correct mass distribution while ensuring structural integrity for the struts, braided carbon fibre tubes are used. The central column has been built with a PVC tube with an additional coating of braided carbon fibres. Figure 2 shows the scaled model in the basin and a sketch with the different parts that compose the model and the materials used in the construction. For the ballast, dumbbell disks on a threaded rod are used, which allow an adjustable center of gravity. The model platform is expected to behave as a rigid body without noticeable deformations for the tested load cases. Compared to the rather flexible tower this seems to be a valid assumption also on prototype scale.

INNWIND.EU D4.2.4: Floating Wind Model Tests at ECN and DHI
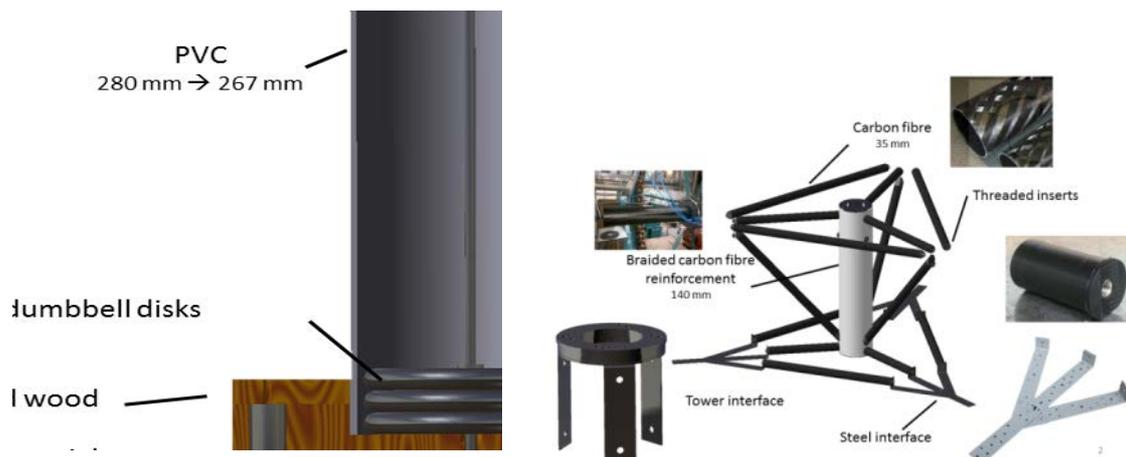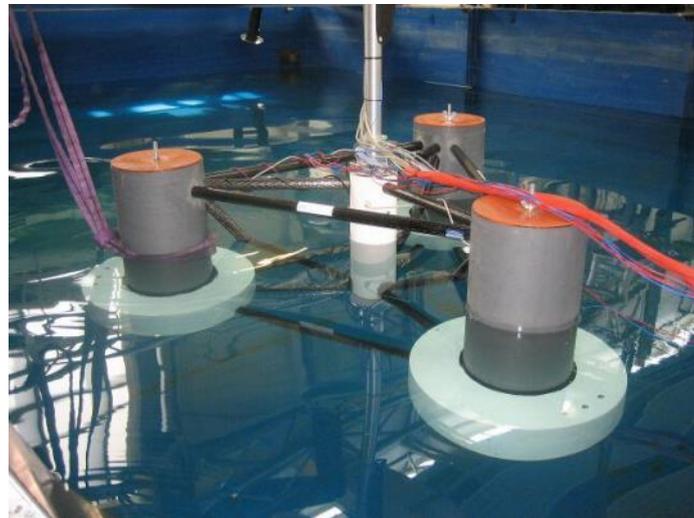
Figure 2 - Platform Model.

2.3.2   Geometry

The geometrical properties of the platform are collected in Table 3. For reasons of the structural integrity and the manufacturability of the platform model some dimensions differ slightly from the scaled properties of the OC4-model. The table summarizes the geometrical properties of the original 5MW full scale platform (in which our 10MW design is based), the 10MW full scale prototype and the scaled model dimensions. The scale factor between the 10MW prototype and the scaled model is 1/60.

Table 3 – Model scale platform geometry (real)

Property	Baseline 5MW Prototype	10MW Prototype	Scaled Model	
Depth of platform base below SWL (total draft)	20	26.67	0,4444	m
Elevation of main column (tower base) above SWL	10	13.33	0,2222	m
Elevation of offset columns above SWL	12	16	0,2667	m
Spacing between offset columns	50	66.67	1,1111	m
Length of upper columns	26	34.67	0,5778	m
Length of base columns	6	8	0,1333	m
Depth to top of base columns below SWL	14	18.67	0,3111	m
Diameter of main column	6.5	8.67	0,1444	m
Diameter of offset (upper) columns	12	16	0,2667	m
Diameter of base columns	24	32	0,5333	m
Diameter of pontoons and cross braces	1.6	2.13	0,0356	m

2.3.3 Mass and Inertial Properties of the Different Model Configurations

Three different configurations of the platform and the scaled wind turbine have been used during the test campaign. The reason to have different configurations is the different system used to include the aerodynamic thrust during the tests, and also that during the first week, the platform was tested without the tower and the rotor. Nevertheless, in all the configurations, ballast was adjusted to have the same overall mass and the same position of the global center of gravity for all the configurations, though it was not possible to match the ideal roll and pitch inertias for the scaled model that have been specified in Table 2 in all the model configurations.

The first configuration was used during the first week and consists of tests with the platform only with no rotor, fan or tower, as can be seen in Figure 3.

INNWIND.EU D4.2.4: Floating Wind Model Tests at ECN and DHI
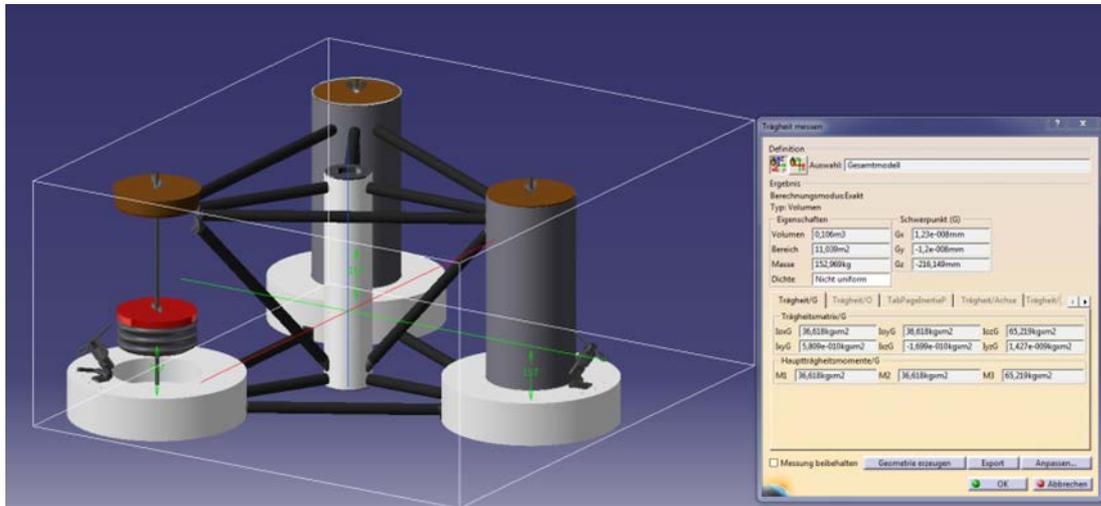
Figure 3 – CAD-Model of platform-only configuration (week1).

The second configuration was tested during the weeks 2 and 3. In this configuration, Froude-scaled rotor (see Section 2.5) was installed to include the aerodynamic thrust. The Froude-scaled rotor is a complex system with equipment, sensors and actuators on the tower top. In consequence, the weight of the rotor exceeded the objective weight to represent the tower top weight in full scale. For this reason, ballast was added to the platform to locate the overall center of gravity in the position corresponding to the full scale platform. This introduced an error in the the pitch and roll inertia of the system.
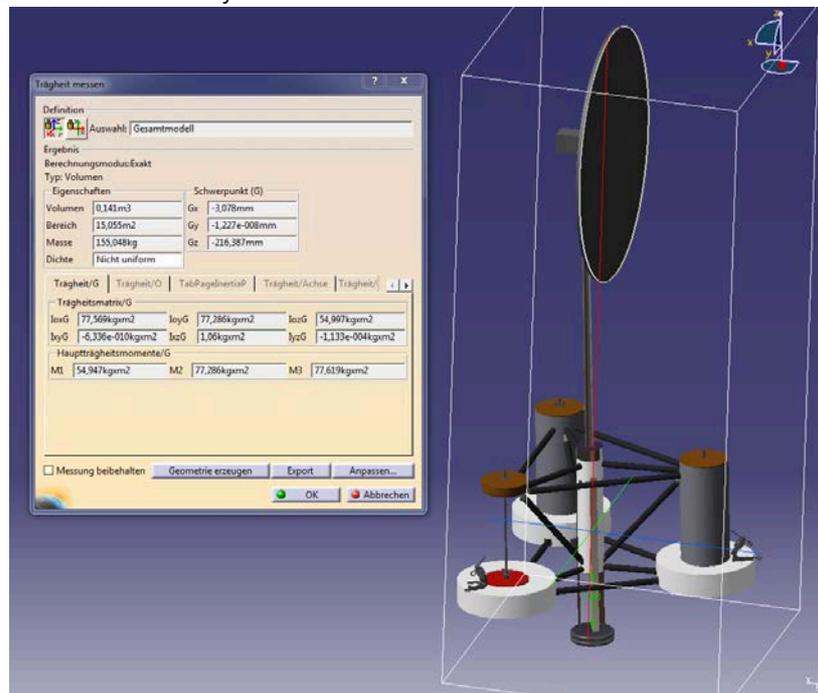
Figure 4 – CAD-model of platform with shifted ballast (week2/3).

INNWIND.EU D4.2.4: Floating Wind Model Tests at ECN and DHI

The extra ballast consisted in two dumbbell disks shifted to 34.8cm below the keel of the platform, see Figure 3 The properties of the aluminum rods and the ballast below the platform keel can be found in Table 4 Due to the additionally displaced water mass ballast had to be added in order to maintain the target draft of the model.
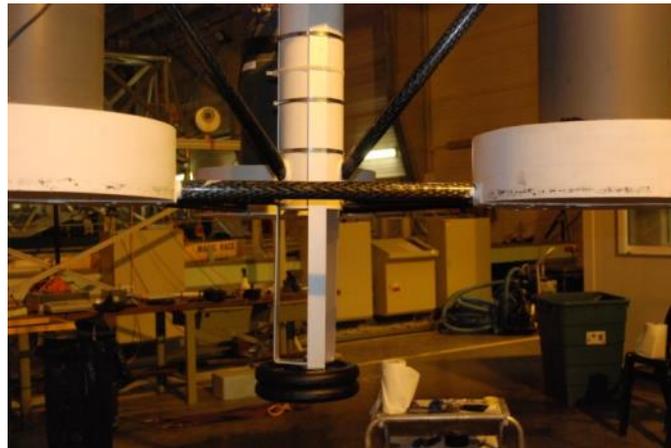
Figure 5 – Shifted ballast.

Table 4 - Shifted ballast.

Property	Value	
Vertical distance from platform lower end to top of dumbbell disks	34.8	cm
Lower dumbbell disk mass	7.432	kg
Upper dumbbell disk mass	7.432	kg
Dumbbell disk volume	0.0009455	m^3
Dumbbell disk radius	0.12	m
Rod mass (one of three)	0.359	kg
Rod length (vertical)	0.9	m
Rod width	0.04	m
Total mass of additional ballast including rods and bolts	16.785	kg

Finally, a third configuration was used during part of the 4th week, where instead of a Froude-scaled rotor, a ducted fan was installed on top of the tower to introduce the aerodynamic force during the tests using the Software-in-the-Loop (SIL) methodology, that is explained in Chapter 2.6. As the weight of the ducted fan is reduced, an extra weight was added to the tower top to match the objective full scale weight of the prototype and the ballast below the keel was removed. A CAD model of the configuration is shown in Figure 6 – CAD-model of platform with ducted fan (week4).
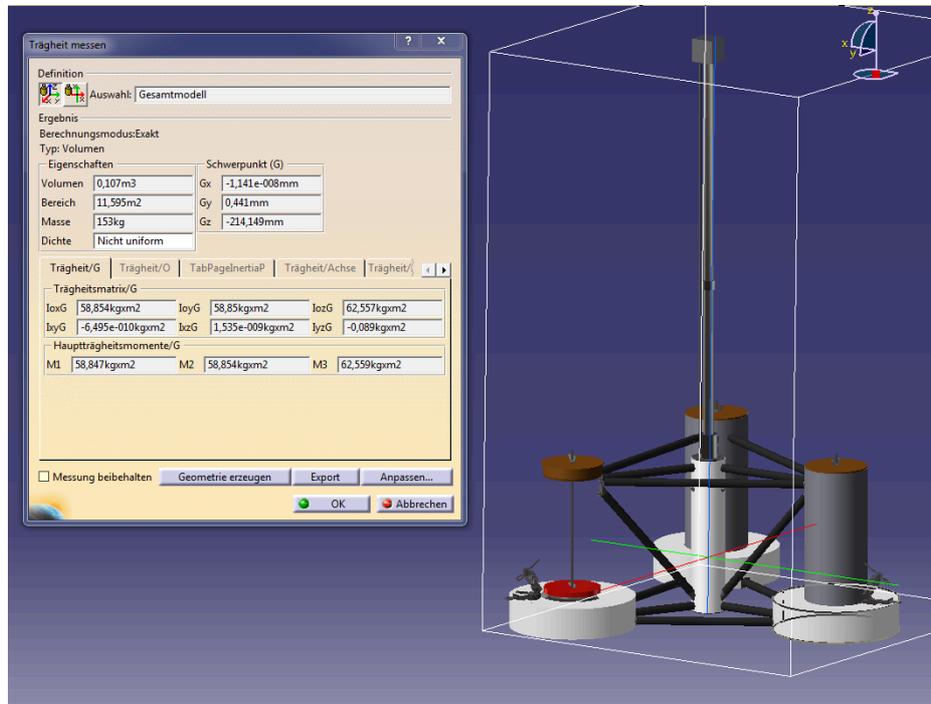
Figure 6 – CAD-model of platform with ducted fan (week4).

A CAD model of the platform has been set up and updated along with the model building process. This allowed keeping track of the change of the target mass, center of mass and the mass moment of inertia during model construction.

The mass distribution is given by the mass scaling factor 93571.5538, see Section 2.2, and the OC4-DeepCwind design, see [3]. Finally, pendulum tests were conducted with the platform only and also with the Froude-scaled rotor mounted on the platform. Using two different pendulum lengths, it is possible to identify the center of mass and also the mass moment of inertia in the considered direction, see Figure 7. The comparison between the CAD data and the identified data from the pendulum experiments can be found in Table 5: the agreement between the CAD computed data and the experimental results are very good, with errors well below 1%. The details on the identification can be found in [6].

Figure 7 – Pendulum tests for mass identification.

Table 5 – Results of benchmark pendulum tests for mass identification (not final configuration).

	Platform only		Platform & Fr-scaled rotor	
	CAD	Experiment	CAD	Experiment
Mass	141.59	141.53	153.14	153.08
Vertical distance from SWL to center of mass [m]	-0.293	-0.293 (about x) -0.295 (about y)	-0.162	-0.162
Roll inertia [kgm²]	34.33	34.14	74.24	74.67
Pitch inertia [kgm²]	34.33	34.22	74.24	74.70
Yaw inertia [kgm²]	60.75	60.83	64.75	61.63

The mass properties of the platform in all different configurations can be found in Table 6. It has been matched to the target mass of $m_{FOWT} = 150.395$kg. With the different attachments below SWL, like fairleads sensors the displaced water volume has been modified from the original OC4 hull shape. Therefore, ballast has been added to the model floating in the basin, such that the waterline is the target one, see Table 6. The center of mass is for all configurations very slightly above the scaled center of mass. This is because small masses were added once the platform was placed in water in order to assure a correct (horizontal) waterline on the platform.

Table 6 – Model scale structural properties (real)

	Week 1	Week 2/3	Week 4
Overall mass, including ballast [kg]	152.97	155.05	153.00
Platform mass, including ballast [kg]	152.97	143.50	146.26
Overall CM location below SWL [m]	0.216	0.216	0.214
System roll inertia about overall CM (incl. shifted ballast and WT) [kgm²]	36.62	77.57	58.85
System pitch inertia about overall CM (incl. shifted ballast and WT) [kgm²]	36.62	77.29	58.85
System yaw inertia about overall CM (incl. shifted ballast and WT) [kgm²]	65.22	55.00	62.56

For the tests with yawed inflow, see Chapter 2.11, the tower interface, see Figure 2, has been modified in order to mount the tower with a yaw angle of +13.5deg.

2.4   Tower properties

The tower mounted on the platform has been used for both, the Froude-scaled rotor (weeks 2 and 3) and the ducted fan (week 4). It has a uniform radius and wall thickness over the entire length. As opposed to the platform, the tower is considered flexible with an approximate eigenfrequency of 2.6Hz. The center of mass of the tower is exactly at its midpoint at $z_{cm,twr} = 1m$ from the tower base. All properties are listed in Table 7. The load cell at tower base is also considered a part of the tower.

Table 7 – Tower properties.

Property	Value
Tower length [m]	1.7205
First eigenfrequency [Hz]	2.6
Fore-aft and side-side stiffness [Nm^2]	1.8957×10^3
Torsional stiffness [Nm^2]	1.4082×10^3
Mass [(including cables traveling within it and along its external surface, i.e. approximately 0.7 Kg/m) [kg]	2.276
Center of mass above SWL [m]	1
Young's modulus [N/m^2]	7×10^{10}
Shear modulus [N/m^2]	2.6×10^{10}
Outer diameter [m]	0.042
Inner diameter [m]	0.04

The eigenfrequencies of the model also scale according to Table 1. The values collected in Table 8 are the scaled eigenfrequencies obtained from full-scale simulations, see [6]. The tower eigenfrequency does not correspond to the original NREL 5MW Baseline wind turbine but to a shortened tower, adapted for the OC4 semisubmersible platform, see [1]. For the calculation of these eigenfrequencies, it has been considered cantilevered on a fixed foundation.

Table 8 – Ideal model scale Eigenfrequencies.

Degree of freedom	Frequency [Hz], Prototype scale	Frequency [Hz], $\lambda = 60$	Frequency [Hz], $\lambda = 45$
Surge	0,00927	0,0718	0,0622
Heave	0,05814	0,4504	0,3900
Pitch	0,03916	0,3033	0,2627
Tower	0,3711	2,8745	2,4894

2.5   Wind Turbine: Low-Reynolds Rotor

As was explained in Section 2.2, when Froude scaling is applied, the Reynolds number is not kept constant, provoking that the aerodynamic loads are out of scale. One solution to obtain representative rotor loads during the tests, is to redesign a scaled rotor with airfoils for low Reynolds numbers as the one designed by Politecnico di Milano for this test campaign, see Figure 8
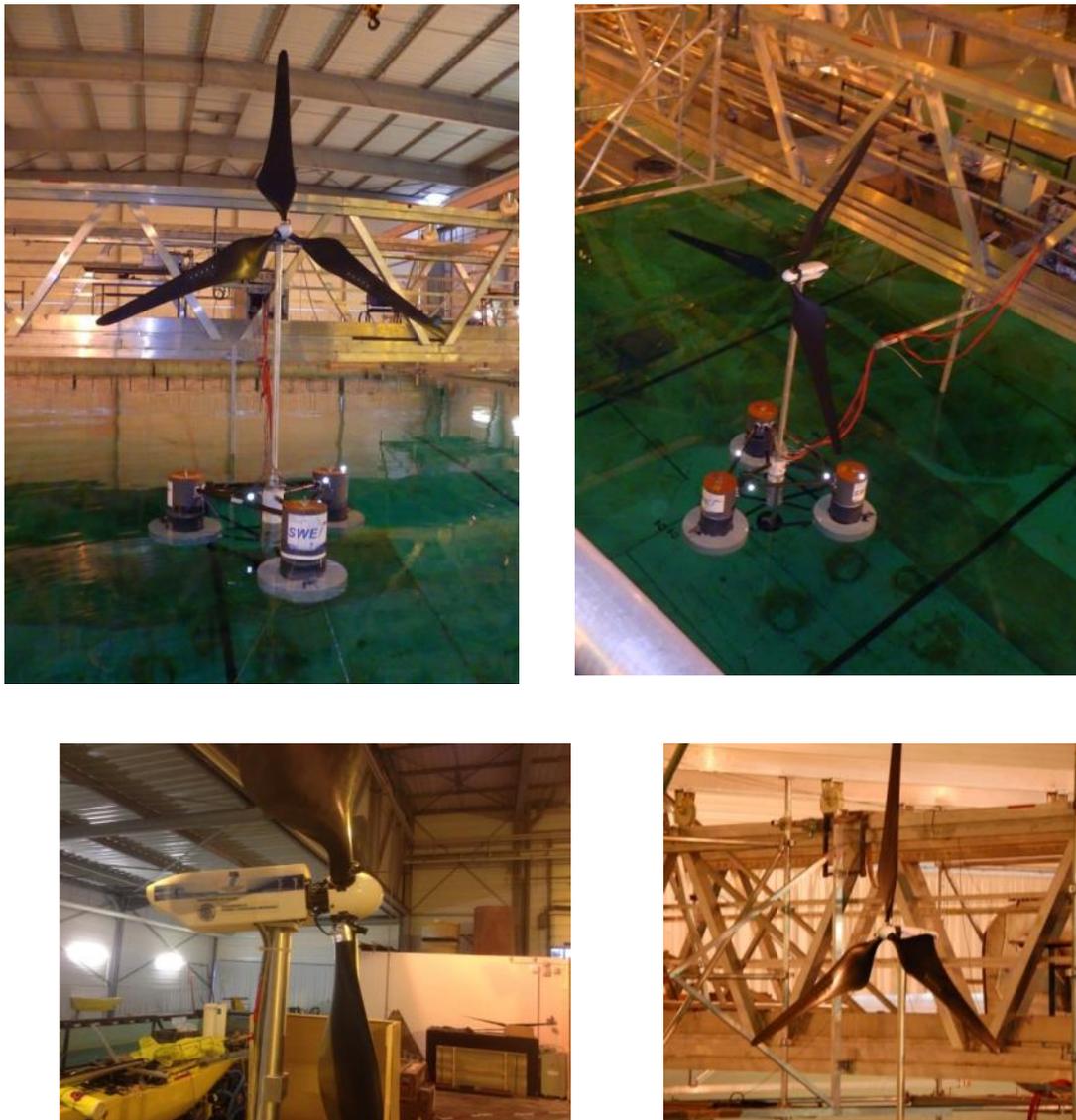
Figure 8 – Froude-scaled rotor.

The rotor has been designed such that mainly the aerodynamic thrust force is correctly reproduced in model scale. The aerodynamic torque and therefore the power have only a second priority as it has a smaller influence on the overall system dynamics. This means that the model

INNWIND.EU D4.2.4: Floating Wind Model Tests at ECN and DHI

torque and power will not allow an estimation of the corresponding values in prototype scale. The main properties of the rotor can be found in Table 9. The blade characteristics are plotted in Figure 9 and Figure 10.

Table 9 - Parameters Froude-scaled rotor.

Parameter	Value
Rotor radius [m]	1.4
Root length [m]	0.054
Rated rotor speed [rpm]	83
Rated rotor torque [Nm]	0.83
Rated rotor thrust [N]	8.779
Optimal tip speed ratio (TSR) [-]	7
Blade Chord @ 0.5 r/R [m]	0.154
Airfoil	RG14
Pitch angle at v_{rated} [deg]	4
Re @ 0.5 $\frac{r}{R}$ & v_{rated}	6E4
Nacelle tilt [deg]	6
Rotor pre-cone [deg]	-2.5
Total blade mass [kg]	0.58
Blade inertia about rotor axis [kgm^2]	0.191
Blade center of gravity along blade span [m]	0.485
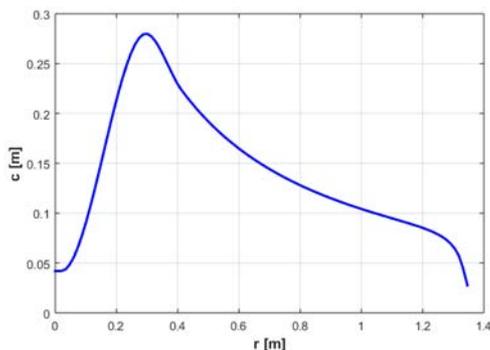
Figure 9 – Model blade chord
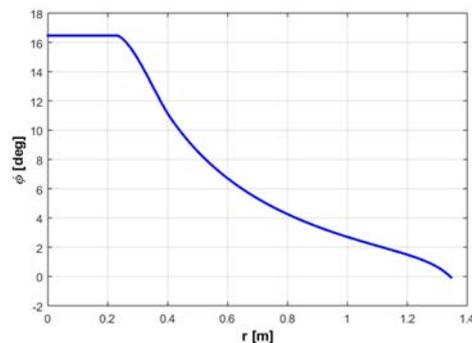
Figure 10 – Model blade twist

The properties of the nacelle, the hub, the generator and the pitch actuator can be found in Table 10, Table 11, Table 12 and Table 13 respectively. The 3D shape of the nacelle can be found in an attached CAD file "nacelle.stp".

Table 10 - Parameters of the nacelle

Parameter	Value
Length [m]	0.29
Height [m]	0.1
Width [m]	0.1
Drag coefficient [-]	2.22
Mass [kg]	3.34
Vertical distance of center of mass above SWL [m]	0.005 + tower length+0.267m
Horizontal distance of center of mass downwind from tower centerline [m]	0.03
Nodding inertia (about center of mass) [kgm^2]	0.0305
Rolling inertia (about center of mass) [kgm^2]	0.0212
Yaw inertia (about tower axis) [kgm^2]	0.0145

Table 11 - Parameters of the hub

Parameter	Value
Mass [kg]	1.824
Hub vertical offset from tower top [m]	0.058
Horizontal distance of center of mass upwind from tower centerline [m]	0.109
Inertia about rotor axis [kgm^2]	0.0028
Spinner diameter [m]	0.095

INNWIND.EU D4.2.4: Floating Wind Model Tests at ECN and DHI

Table 12 - Parameters of the generator

Parameter	Value
Gearbox ratio [-]	28
Generator inertia [m]	3.3163×10^{-6}
LSS stiffness [Nm/rad]	577.1
LSS damping [Nms/rad]	0.2669
Power electronics time constant [s]	0.125×10^{-3}
Maximum demanded generator torque [Nm]	0.83
Mechanical losses	Ω [rpm] $\quad$ M_l [Nm] 0 $\quad\quad$ 0 50.0 $\quad\quad$ 0.1702 100.0 $\quad\quad$ 0.2619 150.0 $\quad\quad$ 0.3214 200.0 $\quad\quad$ 0.3603 250 $\quad\quad$ 0.3929 300 $\quad\quad$ 0.4149 350 $\quad\quad$ 0.4248 400 $\quad\quad$ 0.4198

Table 13 - Parameters of the pitch actuator

Parameter	Value
2nd system (frequency [Hz], damping factor):	19.6, 0.85
Pitch rate upper, lower limits [deg/s]	+160, -160 (week2) +60, -60 (week3)
Pitch position upper, lower limits [deg]	-5, +30

INNWIND.EU D4.2.4: Floating Wind Model Tests at ECN and DHI
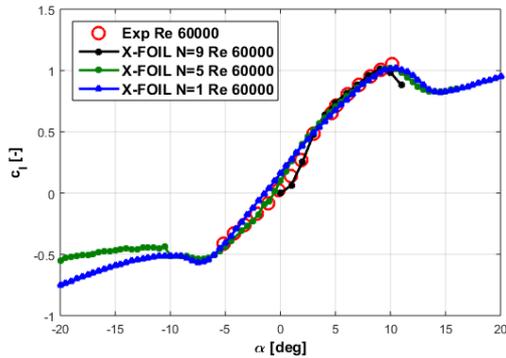
Figure 11 – Experimental and numerical RG14 lift coefficients wrt. AoA
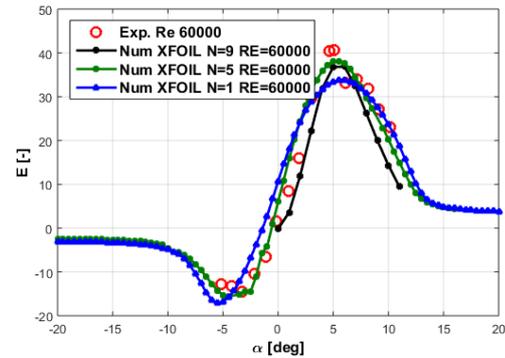
Figure 12 – Experimental and numerical RG14 efficiency wrt. AoA

The polars for blade-element momentum theory (BEM)-calculations on model-scale are available as WT-Perf [7] input file, as well as the CAD models of the blade.

The polars of the model blade airfoil have been first calculated using the program XFoil at Reynolds 60000 and for different value of N_{crit}. The simulated polar for $N_{crit}= 1$ showed a good agreement with wind tunnel measurements [8], as visible in Figure 11 and Figure 12. However, given that it is expected a moderately turbulent flow in the wave tank, the polar data for $N_{crit}= 9$ have been used to build the WT-Perf input file.

In order to match the main properties of the rotor dynamics as already outlined in Chapter 2.2 with the desired ones, the tip-speed ratio TSR and the blade pitch angle can be adjusted, as can be seen in Figure 13 and Figure 14.
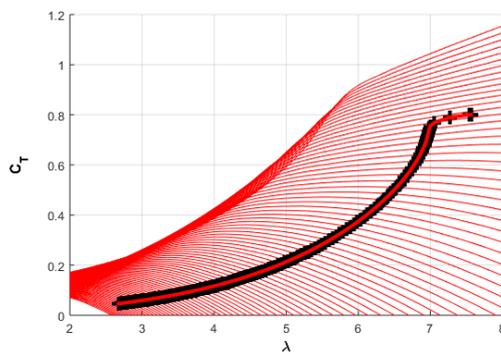
Figure 13 – Model thrust coefficient wrt. TSR and blade pitch.
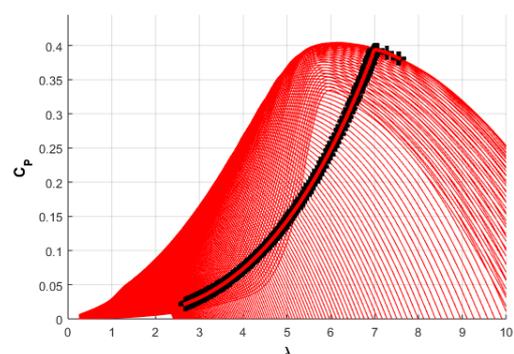
Figure 14 – Model power coefficient wrt. TSR and blade pitch.

Thus at the beginning of every test session (before week 2 and week 3) the pitch angle giving the correct thrust force for a given wind speed has been calibrated as explained in the following paragraph.

At this aim, it was necessary to compute the rotor aerodynamic thrust from the available measurements (see Chapter 2.10.2), i.e. from the tower base fore-aft bending moment M_{fa}.

With M, x_{cog}, y_{cog} respectively three vectors storing the masses, the positions of the centers of gravity along the wind axis and the positions of the centers of gravity along the tower axis of the model sub-components, the overall model mass is 9.179kg, according to Equation (3).

$$M_{model} = \sum_i M_i \tag{3}$$

The position of the overall model center of gravity along the wind and tower axis, computed with respect to the tower base, are $x_{cog,model}$ = 0.0354m (upwind) and $y_{cog,model}$ = 1.532m. These values have been calculated using Equation 4 and Equation 5:

$$x_{cog,model} = \frac{x_{cog}{}^T \cdot \boldsymbol{M}}{M_{model}}$$

(4)

$$y_{cog,model} = \frac{y_{cog}{}^T \cdot \boldsymbol{M}}{M_{model}}$$

(5)

The following relationship has been therefore used to estimate the rotor aerodynamic thrust T using the platform pitch angle θ_P:

$$T = \frac{M_{fa} - gM_{model}(x_{cog,model}\cos\theta_P + y_{cog,model}\sin\theta_P)}{H_{height}}$$

(6)

Equation 6 is only applicable when the rotor operates in steady condition, since it neglects the effect of inertial loads on the tower base measurements.

2.5.1 Pitch angle tuning before week 2 tests

The tests during week 2 have been conducted without using any anemometer for measuring the wind speeds during the test. Before starting week 2 tests, an anemometer located at hub height with the model still not installed within the wave tank, was used to measure the relationship between the power of the fans used to generate the wind and the wind speed measured by the anemometer.
This means that the wind speed during the tests was not known, but was assumed on the basis of the previously computed relationship between wind speed and fans power, which did not account however of any possible effect produced by the model on the upcoming flow.
Several tests have been conducted keeping constant the rotor speed and the fans power while changing the blade pitch. In particular, at the beginning of week 2, the tests listed in [6] were conducted at four different speeds, with the goal of identifying the blade pitch providing the desired thrust coefficients C_T at the target TSR for the 10MW prototype. Values for the 5MW prototype were established as well for reference.

Table 14 Tests conducted for tuning the blade pitch before week 2 tests

	10MW Prototype		5MW Prototype	
	Target TSR	Target C_T	Target TSR	Target C_T
Static_Wind_1d27	7.54	0.94	7.6	0.814
Static_Wind_1d7	7	0.89	-	-
Static_Wind_2d3	4.69	0.16	-	-
Static_Wind_2d68	-	-	4.43	0.148

INNWIND.EU D4.2.4: Floating Wind Model Tests at ECN and DHI
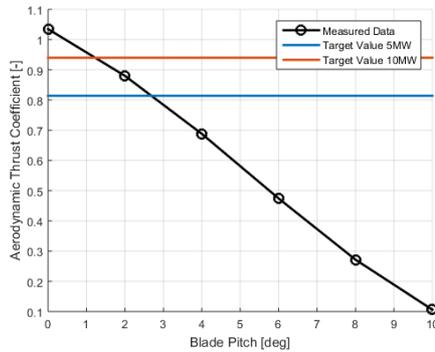
Figure 15 week 2 test "Static_Wind_1d27": thrust
coefficients wrt. blade pitch
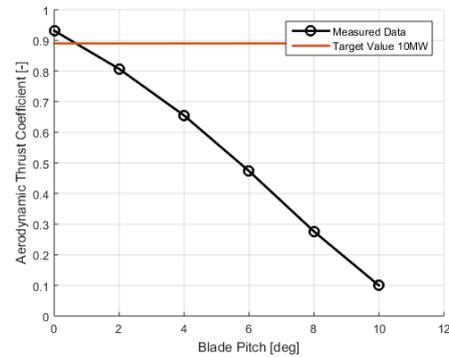
Figure 16 week 2 test "Static_Wind_1d7": thrust
coefficients wrt. blade pitch
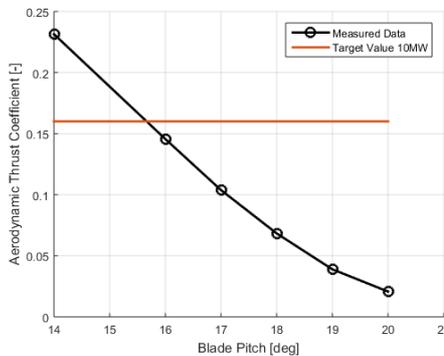
Figure 17 week 2 test "Static_Wind_2d3": thrust
coefficients wrt. blade pitch
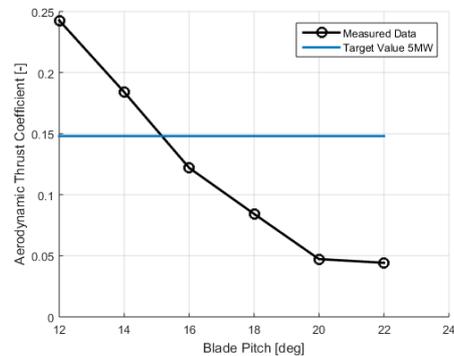
Figure 18 week 2 test "Static_Wind_2d68": thrust
coefficients wrt. blade pitch

For several values of the blade pitch, the thrust coefficients have been computed as

$$C_T = \frac{T}{\frac{1}{2}\rho V^2 A}$$

with $\rho = 1.19\ [kg/m^3]$, the air density.

The tests during week 2 were performed with a fixed rotor speed and blade pitch angle which were set on the basis of the results shown in Figure 15, Figure 16, Figure 17 and Figure 18.

The resulting model operating conditions for tests conducted during week 2 are listed in Table 16. A set of reference tests at 5MW conditions were carried out to allow comparison to earlier studies. The associated operating conditions are shown in Table Table 16.

Table 15 Model Operating condition used during Week 2 tests for the 10MW prototype.

	Blade Pitch [deg]	Rotor Speed [rpm]
Wind_0d9-10MW	1.2	46.7
Wind_1d1-10MW	0.7	53.1
Wind_1d5-10MW	0.7	71.3
Wind_2d3-10MW	15.4	74.7

INNWIND.EU D4.2.4: Floating Wind Model Tests at ECN and DHI

Table 16 Model Operating values for 5MW prototype conditions.

	Blade Pitch [deg]	Rotor Speed [rpm]
Wind_1d04-5MW	3	54
Wind_1d27-5MW	3	65.7
Wind_1d7-5MW	3	81.6
Wind_2d68-5MW	15.5	81.6

2.5.2 Pitch angle tuning before week 3 tests

Week 3 tests have been conducted using anemometers to measure the wind speeds during the test. In particular, the wind speed measured by an anemometer located about 1m from the outlet of the wind generator was used as reference.

It was therefore necessary to calibrate again the pitch angle with the goal of identifying the blade pitch providing the desired thrust coefficients C_T at a target TSR for the 10MW prototype only. The tests listed in Table 17 have been therefore conducted keeping constant the rotor speed and the wind speed and changing the blade pitch.

Table 17 Tests conducted for tuning the blade pitch before week 3 tests

	Target TSR	Target C_T
Static_Wind_v0d90	7.6	0.94
Static_Wind_v1d48	7	0.89
Static_Wind_v2d30	4.8	0.16
Static_Wind_v2d63	4.1	0.11

Similarly to what is described in Chapter 2.5.1, the tests during week 3 were performed with a fixed rotor speed and blade pitch angle (see Table 18) were set on the basis of the obtained results shown in Figure 19, Figure 20, Figure 21 and Figure 22.
When comparing Table 16 and Table 18, it can be noticed that blade pitch angle used during tests performed in week 2 and week 3 are not the same, despite in both case the rotor thrust coefficients were nominally the same. This is mainly due to the fact that during week 2 tests the wind speed was not known, but was simply estimated by using the relationship wind speed-fans power obtained as described in Chapter 2.5.1. This implies that the effective wind speed viewed by the rotor during week 2 tests was probably different from the estimated one, which translates into different values of the blade pitch required to generate the target thrust than the ones used for week 3 tests.
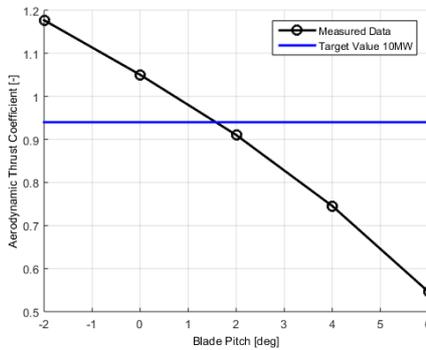
Figure 19 Week 3 test "Static_Wind_v0d90": thrust coefficients wrt. blade pitch
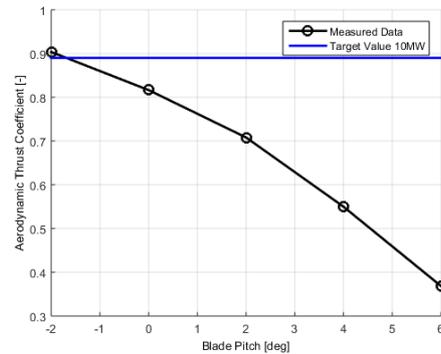
Figure 20 Week 3 test "Static_Wind_v1d48": thrust coefficients wrt. blade pitch
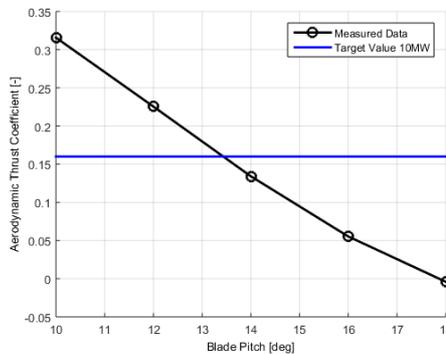
Figure 21 Week 3 test "Static_Wind_v2d30": thrust coefficients wrt. blade pitch
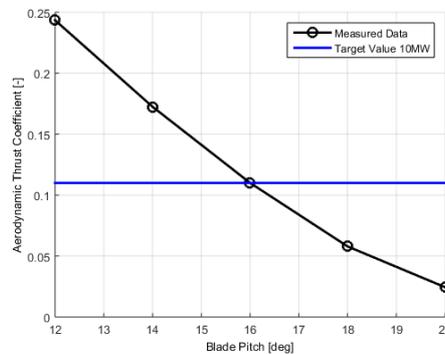
Figure 22 Week 3 test "Static_Wind_v2d63": thrust coefficients wrt. blade pitch

Table 18 Model Operating condition used during week 3 tests for the 10MW Prototype

	Blade Pitch [deg]	Rotor Speed [rpm]
Wind_0d90-10MW	1	46.7
Wind_1d48-10MW	-2.2	71.3
Wind_2d30-10MW	13	75.3
Wind_2d68-10MW	16	75.3

2.6   Wind Turbine: Ducted Fan

An alternative method to the design of a low-Reynolds rotor to achieve representative rotor thrust during the execution of the tests is the use of a ducted fan to introduce a controlled force at the tower top that represents the aerodynamic loading. This method has the advantages of being very economical and avoiding an external wind generation system to introduce the main force impacting the floating system by other means. Several of these options and the correlated experiments from the literature are outlined in [4]. The use of this method in addition to the low-Reynolds rotor will allow an assessment of the advantages and shortcomings related to this simplified testing method.

The basic concept of the method consists of substituting the rotor by a fan driven by an electric motor. The fan thrust is controlled by the fan rotational speed set by the controller, which again

depends on the real time simulation of the full scale rotor in a turbulent wind field, with the platform motions measured in real time in the wave tank test. A picture of the ducted fan at the tower top is shown in Figure 23. Details on the configuration and the control algorithms can be found in [9].

Figure 23 – Ducted fan (week 4)

The fan and its real-time controller are lighter than the scaled mass and thus, ballast has been added to the nacelle to match the full scale configuration. The fan is mounted on the same tower as the Froude-scaled rotor, see Chapter 2.4.

The model of ducted fan selected to generate the force representing the aerodynamic thrust during the tests is the DS-30-AXI HDS, manufactured by the German company Schübeler. As shown in Figure 24, the fan is powered by a brushless motor HET 2W20 that is controlled by an Electronic Speed Controller (ESC) YGE 90 HV, and works with an industrial AC/DC power supply. This system configuration produces an approximate force range of 0-18N. The rpm of the motor (and therefore the force produced by the fan) is controlled by a Pulse Width Modulation (PWM) signal that is generated with the LabVIEW control software, using servo libraries for Arduino. The demanded force for the fan is provided by the full scale simulation of the rotor's aerodynamic thrust.

The software used to compute the aerodynamic loads in real time is the version v6.02c-jmj of the FAST code, with AeroDyn 12.58. These codes have been developed by NREL [10], and modified by CENER to be used in real time and coupled with the test. The software has been compiled in Linux and during the test campaign it was ran in a computer with a 2.54GHz Intel Core Duo CPU and 2GB of RAM.
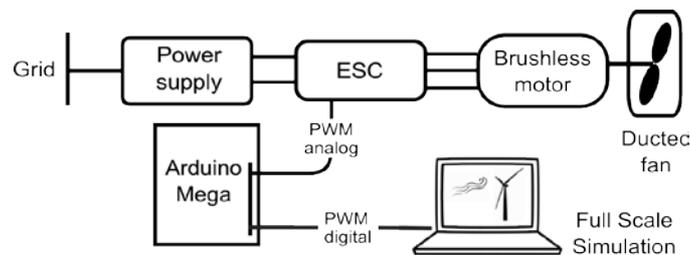
Figure 24 – Fan Control System Lay Out

INNWIND.EU D4.2.4: Floating Wind Model Tests at ECN and DHI

The layout of the system is shown inFigure 25. The left side describes the simulation part of the system, which works in full scale, and the right side represents the wave tank scaled test. The different magnitudes that are interchanged between both blocks are transformed by the appropriated scaling laws based on the factor scale λ.
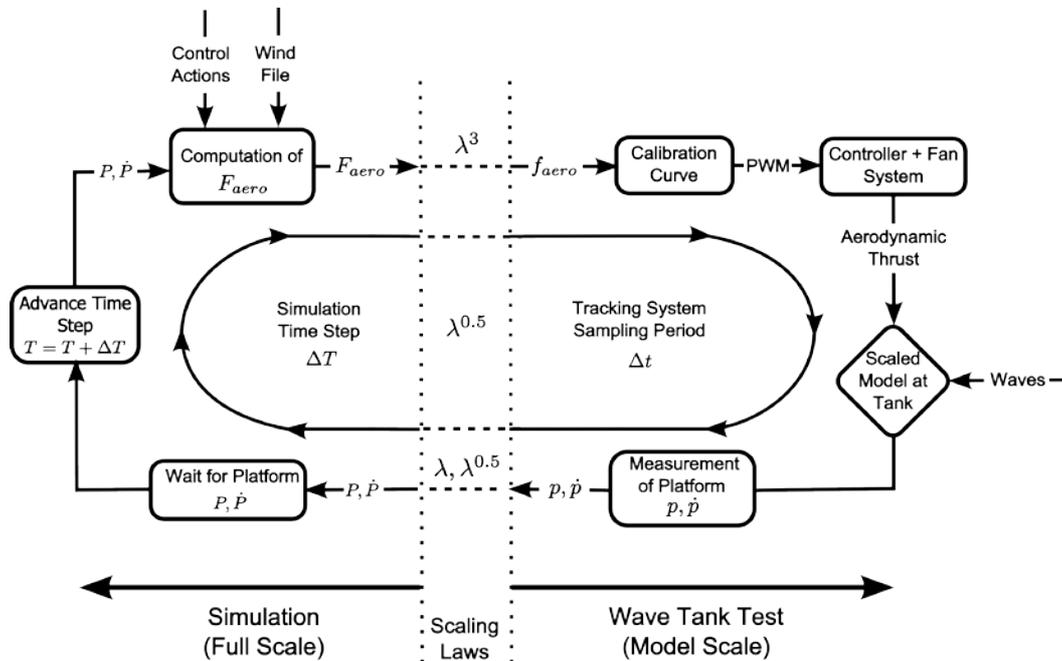
Figure 25 –Software-in-the-Loop Method Diagram

The simulation tool provides the total aerodynamic force on the shaft F_{aero} from integration of all the aerodynamic loading at the blade elements. This force in full scale is transformed to the model scale (f_{aero}) and the pulse width of the PWM signal needed to produce the force in the ducted fan is provided by a calibration curve. The control system regulates the fan speed that introduces the desired force at the model's hub height. The waves produced by the wave maker are also acting over the platform and, together with the aerodynamic thrust, inducing motions. The acquisition system measures the positions and velocities for the 6 degrees of freedom of the platform at a certain sampling period. These measurements are sent to the simulation tool that is waiting for the data to advance one time step and calculate the new value of the aerodynamic thrust. For this reason, the sampling period, Δt, and the simulation time step, ΔT, have to be set accordingly (with a factor of $\lambda^{0.5}$).

2.7   Mooring System

The mooring system is modelled through a norm steel chain of DIN 763 with a wire diameter of 2mm and a length of the links of 22m. The mooring system is composed by 3 lines, one upwind and two downwind, with an angle of 120° between them. Figure 26 shows a top view of the scaled model mooring system.
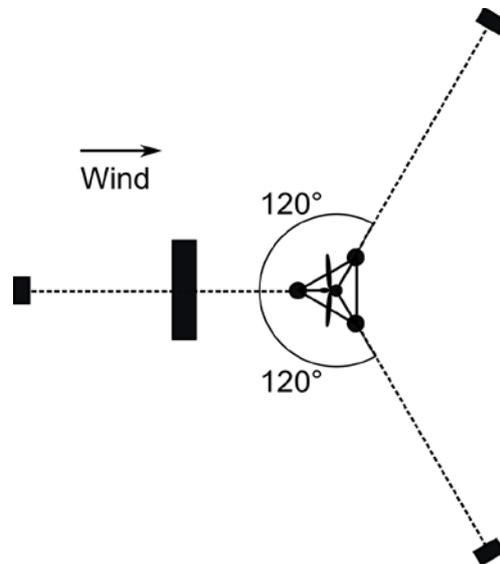
Figure 26 – Sketch of mooring system configuration.

The main dimensions of the lines are summarized in Table 19 – Main dimensions of the mooring system.

Table 19 – Main dimensions of the mooring system

Parameter	Baseline 5MW Prototype	10MW Prototype	Scaled Model (target value)	
Radial distance of the fairleads	40.868	54.49	0.908	m
Draft of the fairleads	14	18.67	0.311	m
Radial distance of the anchors	837.6	1116.8	18.613	m
Depth of the anchors	200	266.67	4.444	m
Angle between lines	120	120	120	deg

Due to the fact that the basin depth (5m) is higher than the target scaled depth of 4.44m corresponding to a prototype sea depth of 266m for $\lambda = 60$ the original baseline mooring system has been re-designed for the increased depth.

This has been done by modifying the length of the unstretched line while keeping the model chain properties, see Table 19. Figure 27 shows the force-displacement relationship of the target mooring system and the system with the increased depth with several line lengths in prototype scale. The x-axis starts at the anchor, the initial fairlead position is at 729m.

INNWIND.EU D4.2.4: Floating Wind Model Tests at ECN and DHI

Table 20 summarizes the properties of the real scaled mooring system implemented during the tests.

Table 20 - Model mooring system properties.

Parameter	Line 1	Line 2	Line 3
Anchors radial position [m]	17.11		
Fairleads radial position [m]	0.908		
Angular position of anchors [deg]	180°	60°	300°
Angular position of fairleads [deg]	180°	60°	300°
Depth of anchors [m]	5m		
Draft of fairleads [m]	0.311		
Unstretched length of the lines (anchor to fairlead, including portion of string, see Figure 54) week1/2 [m]	17.28	17.277	17.275
Unstretched length of the lines (anchor to fairlead, including portion of string, see Figure 52) week3/4 [m]	17.273	17.272	17.27
Chain wire diameter [m]	0.002		
Mass density in air [N/m]	0.062		
Equivalent hydrodynamic diameter [m]	0.0032		
Equivalent mass density in water [N/m]	0.0534		
Axial stiffness (EA) [N/m]	360000		

Some of these parameters are known, as the depth of the water basin, and others have been measured: the mooring line lengths from anchor to fairlead are given based on the measurements

INNWIND.EU D4.2.4: Floating Wind Model Tests at ECN and DHI

of the length of the strings which connect the chain with the fairlead sensors, see Section 2.10.1. The fairlead is considered to be located at an orifice on the level of the base columns (see Figure 54 and Figure 55). The anchor position should be taken as an approximate value with the precision in the range of centimeters due to the fact that the radial distance has to be measured under water by a diver. Experiments with a shortened line (by 5 links) have been conducted in week 3 in order to allow for an error assessment of the mooring system, see Section 2.11.

The values for the chain mass density in air and for the chain equivalent hydrodynamic diameter in Table 20 have been derived from measurements in laboratory of the total length, weight and volume of two of the three chains used as lines. Figure 28 shows the method used to calculate the total chain volume.

Figure 28 – Measurement of the water displaced volume for one chain

The measured parameters are presented in Table 21. The total length of the chain does not correspond to the exact length used to connect the fairlead and the anchor, because the total length of the chain was not used as mooring line during the tests.

Table 21 – Chain measured parameters.

	Total Length (m)	Total Line weight (kg)	Total Line Volume (l)
Line 1	19.285	1.191	0.1535
Line 2	19.171	1.188	0.15366

From these measurements the chain mass density and the equivalent hydrodynamic diameter have been calculated and the results are presented in Table 22. These are the values included in Table 20 for the air mass density and the equivalent hydrodynamic diameter.

INNWIND.EU D4.2.4: Floating Wind Model Tests at ECN and DHI

Table 22 - Derived chain mass density and equivalent diameter.

	Mass Density (kg/m)	Equivalent Hydrodynamic Diameter (m)
Line 1	0.06176	0.00318
Line 2	0.06197	0.00319

The axial stiffness in Table 20 was estimated using the formula:

$$EA = 90000\, D^2 \tag{7}$$

Where the extensional stiffness has the unit [N] and the chain wire diameter is input in mm, see [11], Lecture 14.

2.8 External Conditions

The combined wind-wave facility *LHEEA - Research Laboratory in Hydrodynamics, Energetics and Atmospheric Environment* has an open wind generator above the surface of a wave basin. For the Froude-scaled rotor tests the wind generator was used whereas the ducted fan allowed testing without an external wind generator.

The temperature, pressure and air density during the tests can be found in Table 23. The temperature is a value from the measurements of the microcontroller board in one of the platform columns.

Table 23 – Atmospheric data from wave basin.

Air temperature [deg]	≈ **16** (ECN: 14-15, Arduino in column: 17)
Water temperature [deg]	17
Humidity [%]	70-80

2.8.1 Wave Basin

The dimensions of the wave tank are 50x30x5m with a central pit of 5x5m of 10m depth, which was, however, closed during the tests. Regular and irregular waves as well as waves with different heading directions can be produced. The wave generator can operate in force or motion control mode with 48 controlled flaps. The sea states range from periods of 0.5 – 5s with a maximum wave height of approximately 1m.

INNWIND.EU D4.2.4: Floating Wind Model Tests at ECN and DHI

Figure 29 – Ecole Centrale de Nantes wave basin (LHEEA).

Figure 30 – Wind generator outlet.

2.8.2 Wind Generator

The wind generator outlet has a cross sectional area of 3x3m. The outlet can be moved to a central location of the wave basin in order to provide the wind turbine with the highest achievable wind quality. For this test it was located at a distance of 4m from the center of the wind turbine. The turbulence intensity is below 5% and the longitudinal and radial wind homogeneity is, at least for high wind speeds, very good. The details on the open wind tunnel can be found in [12] and [13].

The longitudinal evolution of the jet has been assessed in [12], seeFigure 31. However, for the small wind speeds between 1 and 2m/s used in these experiments a significant decrease of wind speed in longitudinal direction (x) and also depending on the radial position has been observed. Therefore tests with woollen strings attached to a vertical fishing line have been performed to locate the shear layer without the turbine. Ultrasonic measurements were then performed at locations of the shear layer.
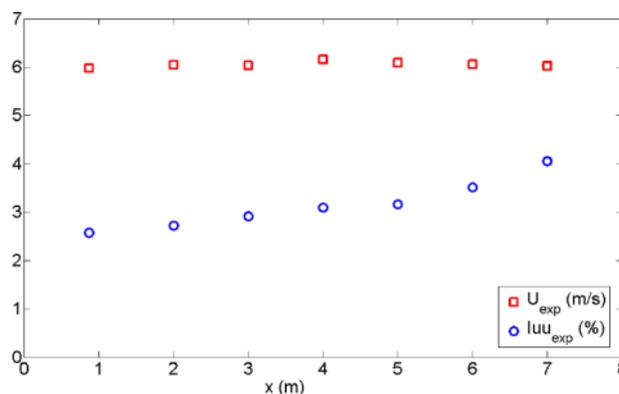
Figure 31 – Longitudinal evolution of the jet [12]. Wind speed (red), turbulent kinetic energy (blue).

More details on the dimensions of the wave tank, mainly for CFD calculations, can be found in the attached file "ECNBasinDimensions.pdf" which was kindly provided by ECN after request.

INNWIND.EU D4.2.4: Floating Wind Model Tests at ECN and DHI

2.9   Verification of the scaled model characteristics

In the present section the verification of the Froude-scaled rotor model characteristics is carried out. Having a Froude scaled model, verification of the design using linear tools in terms of the hydrodynamic characteristics of the model is direct and there is no need for repeating it. Use of non-linear models and/or of models addressing viscous hydrodynamic effects is outside the scope of the present task and will be part of the validation process of tools included in the forthcoming task. Similarly for the mooring lines their separate analysis at this stage is not expected to give further verification outside of the framework of fully coupled simulations which are also foreseen as part of the validation of tools. Therefore the present verification focuses on the scaled rotor which due to its size and the test conditions has two specific issues.

The rotor is not Re scaled. In fact the Re number is ~60000 which is significantly lower than the full scale operational values. Because of that and in view of at least match the thrust characteristics, POLIMI designed a special rotor for the test conditons with specific airfoil shape, chord and twist distribution and control settings. In principle the same rotor but with different control setting can be used to model the thrust characteristics of other prototype rotors. Here, we analyse the rotors performance in representing the INNWIND.EU 10MW rotor and the NREL 5MW rotor.

In addition to the Re issue, there is a second one in connection to the provision of the wind inflow during the tests. The use of a fan system that provides a jet flow can have significant effects on the behavior of the wind turbine. The fact that outside the jet stream there is no air flow renders the inflow conditions different from the full scale "infinite" inflow conditions. The rotor acts as a resistance to the flow and will force the jet to expand and therefore reduce the mass flow through the rotor disk.

With respect to the "Re issue", POLIMI provided airfoil polars using XFOIL with N_{crit}=1. Based on these polars BEM computations were performed and the control setting were defined by matching the NREL CT curve. In the verification presented next the following additional calculations were performed:

a) Using 2D RANS CFD, the polars of the RG14 airfoils were calculated.
b) Using the XFOIL and the CFD polars, the control settings have been re-determined for the INNWIND.EU and NREL 5MW rotors.
c) Using 3D RANS CFD, the performance at rated and above conditions is assessed in full space (infinite) uniform wind conditions.

Remark: Conditions below rated were not considered, assuming that the controller will take care of any differences in the inflow and provide operation at max Cp.

With respect to the "jet inflow" issue, the performance at rated and above conditions is assessed. To this end "infinite" conditions are compared to "jet inflow" conditions using vortex modeling. To this NTUA's vortex model GENUVP is used. In its baseline version, GENUVP combines a 3D panel method for the rotor blades and a vortex particle simulation of the rotor wake. The effect of the jet has been added as a shear layer carrying surface vorticity and allowed to deform under the effect of the presence of the rotor. This model was originally applied to tests carried out in the LLF DNW section for helicopters and wind turbines [14]. Indicative results in connection to the MEXICO experiment [15] are given in Figure 32-Figure 34. The simulation corresponds to a nominal wind inflow of 10m/s and comparisons with and without the tunnel effects are carried out with respect to measurements. The specifc run covers 56 full rotations with 36 time steps per rotation. The results clearly indicate that the presence of the rotor provokes the cross expansion of the jet and so the rotor receives a lower wind inflow compared to that set at the nozzle outlet.

INNWIND.EU D4.2.4: Floating Wind Model Tests at ECN and DHI

MEXICO, U=10m/s: upstream & downstream velocity (x=-0.3, 0.3m), azim.=0de

MEXICO rotor, U=10m/s, Cp distribution at r/R=82
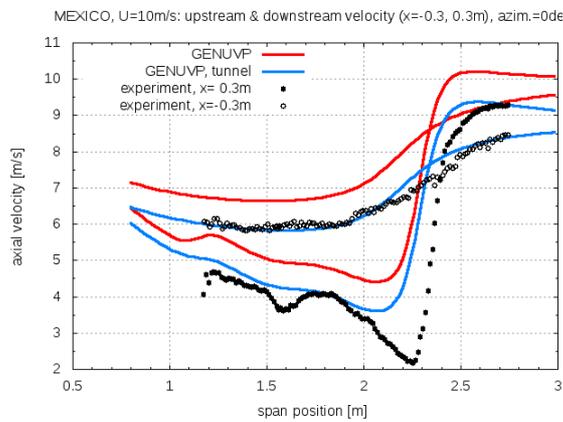
Figure 32. Comparison of the axial velocity distribution upstream and downstream of the MEXICO rotor at nominal 10m/s wind speed. Vortex simulations with (blue) and without (red) the effect of tunnel are compared to measurements. Adding the effect of the shear layer, gives a very good match with the upstream axial flow conditions. In the wake, there is good agreement except over the tip region (2.<r <2.6). In the specific simulation the time step corresponded to 10° azimuth step. Such a wake resolution is expected to filter the intensity of the velocity shear at the tip. Furthermore the velocity gradient is seen further inboard in the vortex predictions as compared to measurements. This is due to the lack of viscous diffusion in the simulation.
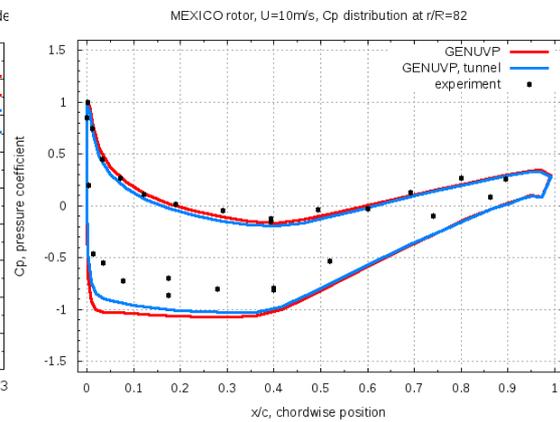
Figure 33: Pressure distribution at r/R=0.82. Vortex simulations with and without the effect of tunnel are compared to measurements. Adding the tunnel effects improves the accuracy leading to lower loading. It is noted that the simulations are inviscid and so the over-prediction of pressure on the suction side is explained.
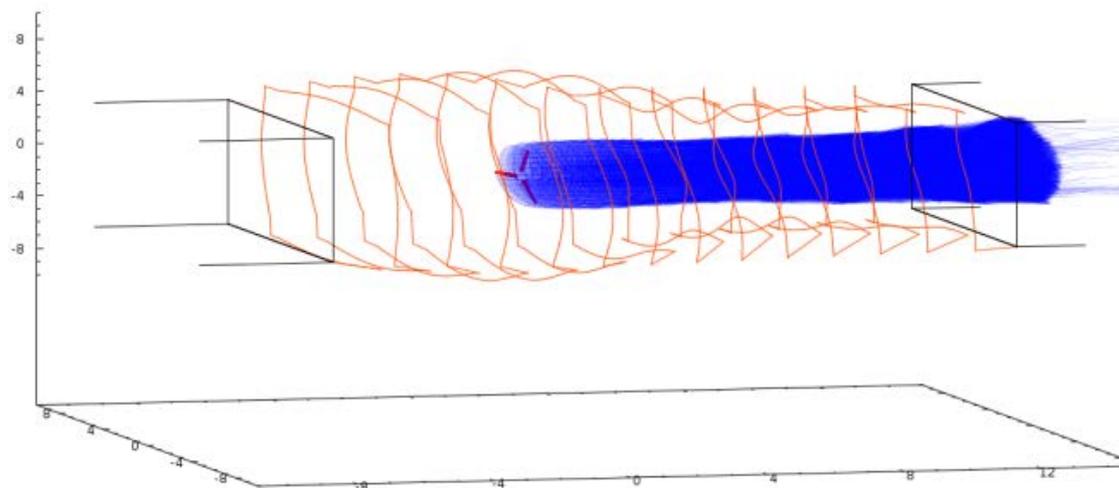
Figure 34: Layout of the wake development after 56 full rotations. The black lines on the left and right part of the figure indicate the inlet nozzle and collector respectively. The red lines indicate the position of the shear layer while the rotor wake is shown in blue. The deformation of the shear layer is clearly seen. Besides the expected expansion and contraction, there is also a swirling rotation noted.

INNWIND.EU D4.2.4: Floating Wind Model Tests at ECN and DHI

2.9.1 Assessment of the Re issue: 2D Polars

In Figure 35 the XFOIL polars calculated by POLIMI are compared to RANS CFD simulations using MaPFlow which is the CFD tool developed at NTUA and already used in WP2 of the present project. The XFOIL results correspond to free transition conditions. Transition in XFOIL is modeled by the e^N model. The specific results were obtained by setting $N_{crit}=1$. On the contrary the CFD results correspond to fully turbulence conditions. This choice for the CFD runs was made in order to have less uncertainty in the predictions since transition modeling at Re numbers in the range of 10^4 – 10^5 is questionable at least with some of the known models such as the Re_θ-γ and Granville models.

The comparison is fair over the linear part of the CL curve and there is good match in terms of drag over the same range. At high angle, CFD predicts stall earlier which also results lower CL values in the post stall region. This is expected since the CFD results correspond to fully turbulent conditions. Assuming that most of the rotor will have attached flow conditions in all of its operation conditions the different post-stall behavior is not regarded critical.

INNWIND.EU D4.2.4: Floating Wind Model Tests at ECN and DHI

RG14 airfoil polars

RG14 airfoil polars
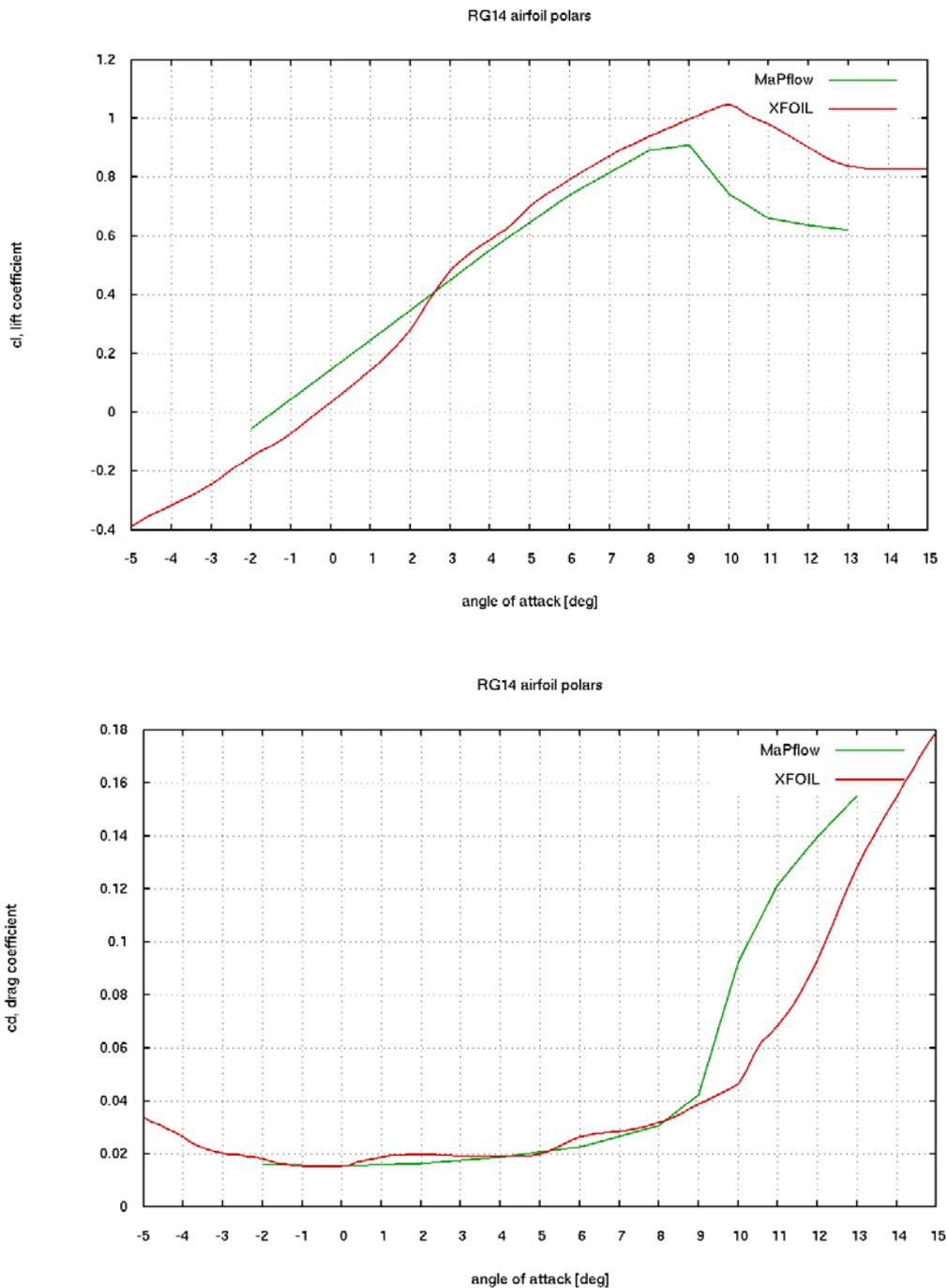
Figure 35: Comparison of the 2D polars. The XFOIL CL, CD polars are compared to 2D CFD simulations at Re=60000. The CFD results correspond to fully turbulent conditions using the k-ω SST model. The CFD simulations above 10deg were unsteady and the values shown in the graph are averaged values.

2.9.2 Assesment of control setting

The control settings include the fixed pitch at rated conditions (TSR=7, 81.2RPM) and the pitch schedule at conditions above rated.

INNWIND.EU D4.2.4: Floating Wind Model Tests at ECN and DHI

The CT (thrust coefficient) performance for the POLIMI scaled rotor is presented in Figure 36 for operation at above rated conditions (TSR<7) and for various pitch setting ranging from -2° to 25° with a 0.5° step. In the graphs the targeted CT curves for the INNWIND.EU 10MW and NREL 5MW are included giving an overview of the framework for determining the pitch schedule. This has been done using the two sets of polars (XFOIL, MaPFlow) presented in the previous paragraph. Similarly in Figure 37 the corresponding results in terms of CP (power coefficient) are shown.

(a)

(b)
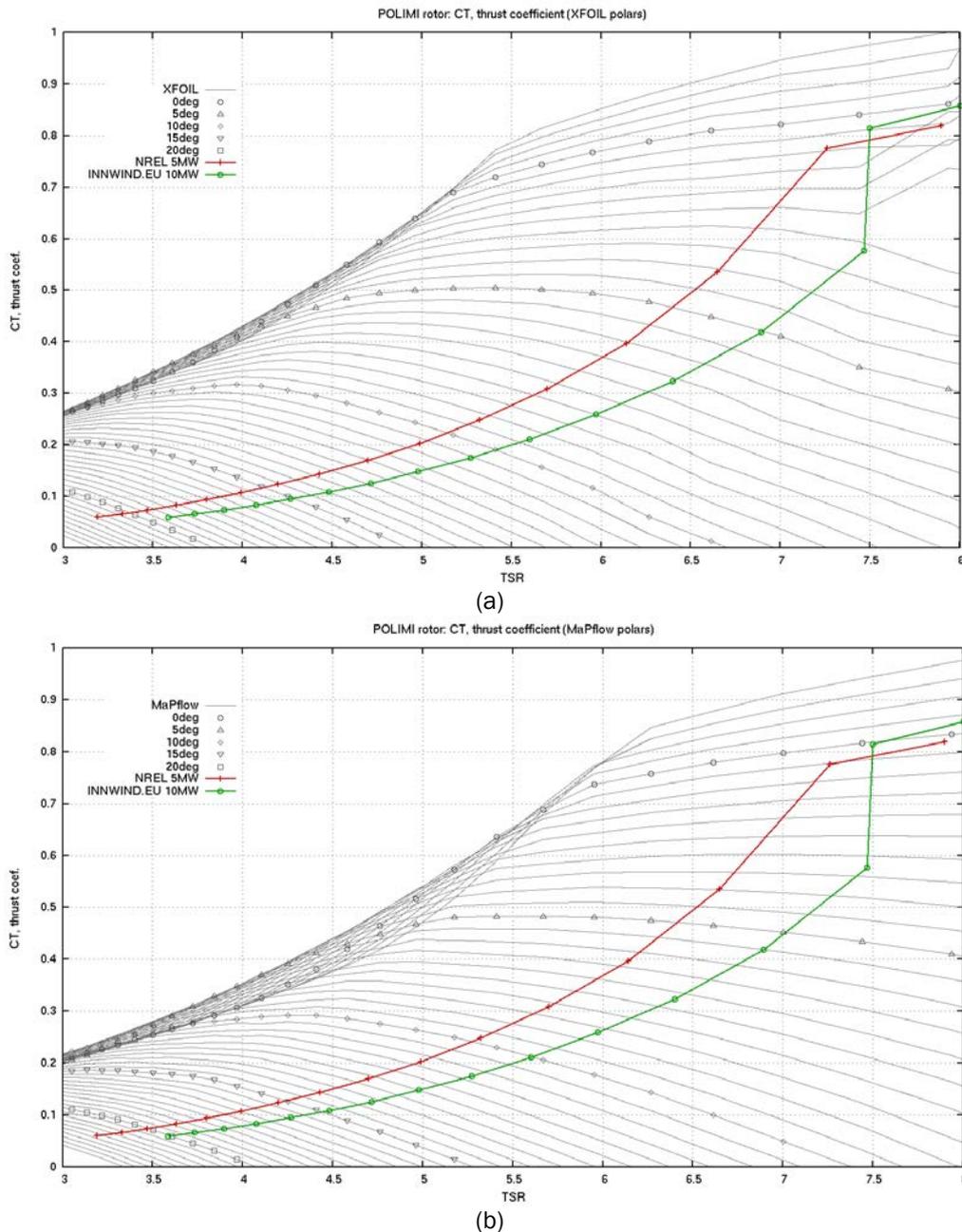
Figure 36: Pitch settings for the POLIMI scaled rotor. The graphs include:
- **the CT performance curves (grey lines) of the scaled rotor using the two sets of polars (XFOIL (a), MaPFlow (b)) at pitch settings ranging from -2° to 25° with a step of 0.5° and**
- **the INNWIND.EU 10MW (green line) and NREL 5MW (red line), targeted CT curves.**

Through matching the pitch schedule at conditions above rated is determined.

INNWIND.EU D4.2.4: Floating Wind Model Tests at ECN and DHI

(a)

(b)
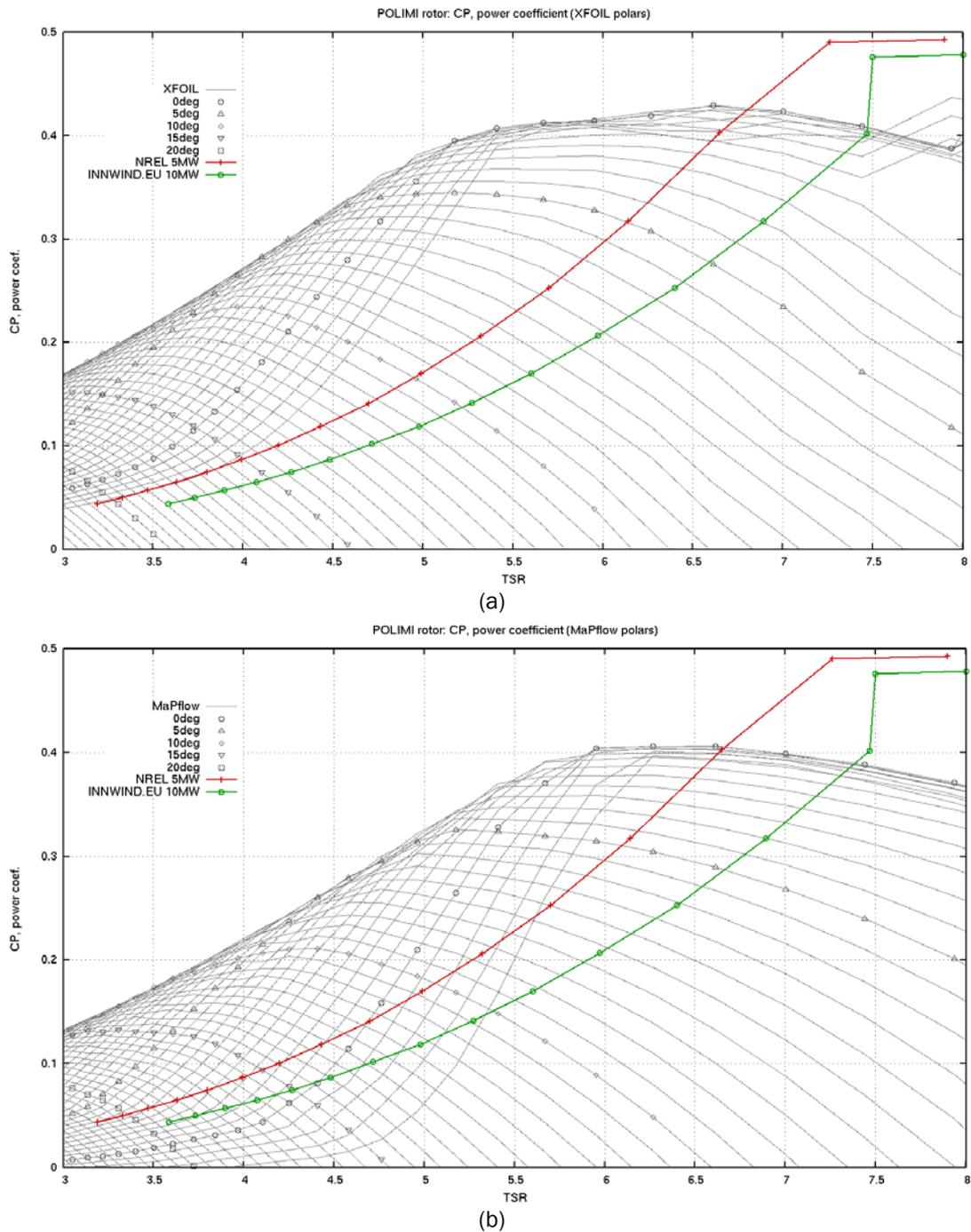
Figure 37: CP performance curves for the POLIMI scaled rotor. The graphs include:

- the CP performance curves (grey lines) of the scaled rotor using the two sets of polars (XFOIL (a), MaPFlow (b)) at pitch settings ranging from -2º to 25º with a step of 0.5º and
- the INNWIND.EU 10MW (green line) and NREL 5MW (red line) CP curves.

The pitch schedules for the INNWIND.EU 10MW and NREL 5MW as obtained through matching are presented in Figure 38 for the two different polars. There is a difference of almost 1deg between the two sets which is due to the differences already noted in Figure 35. Such a difference in the

INNWIND.EU D4.2.4: Floating Wind Model Tests at ECN and DHI

pitch schedule is regarded small and acceptable especially when also considering the deviation in CP shown in Figure 39 and Figure 40.
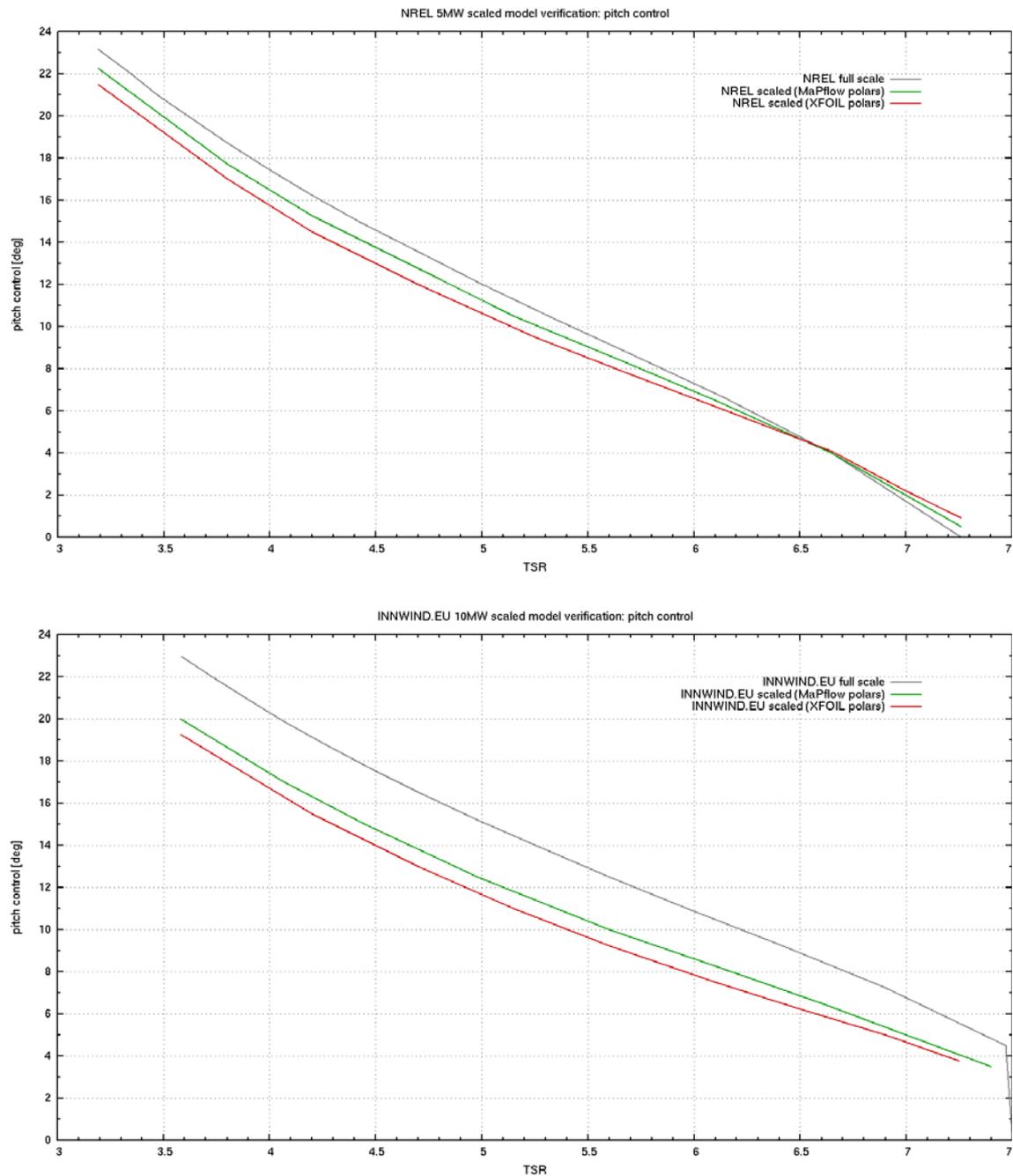
Figure 38: Predicted pitch schedule of the scaled rotor in comparison to the INNWIND.EU 10MW and NREL 5MW settings. The gray line corresponds to the full scale rotors, the green lines correspond to the fitting using the XFOIL polars and the red lines correspond to the fitting using the MaPFlow ones
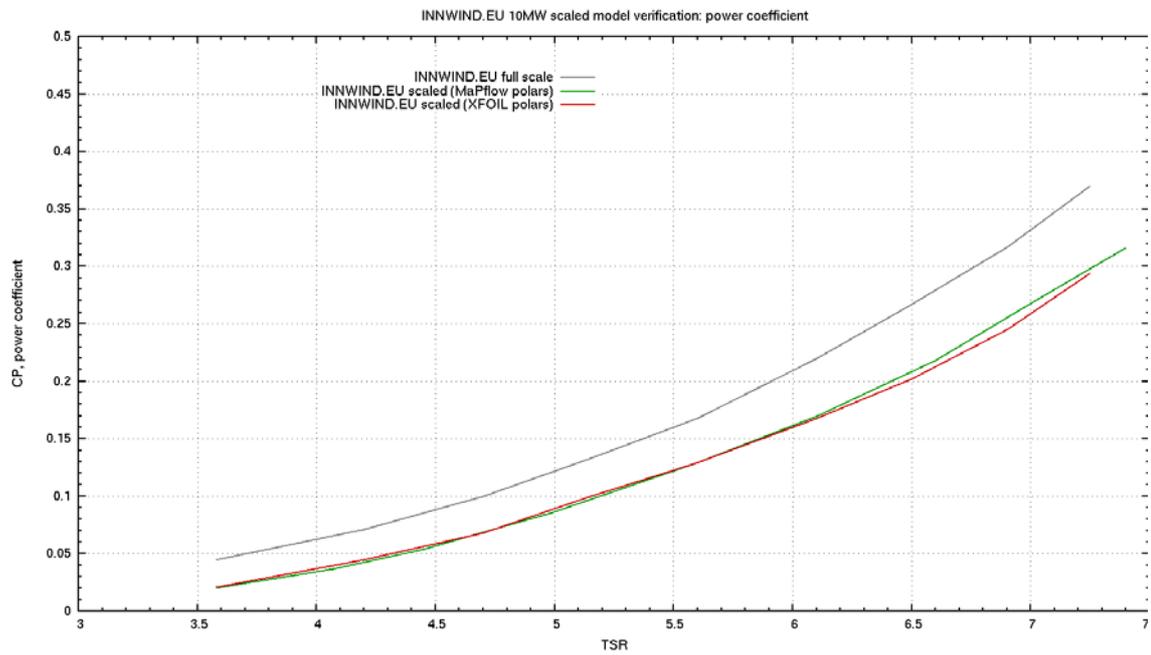
Figure 39: CP variation using the XFOIL and MaPFlow polars for the INNWIND.EU 10MW
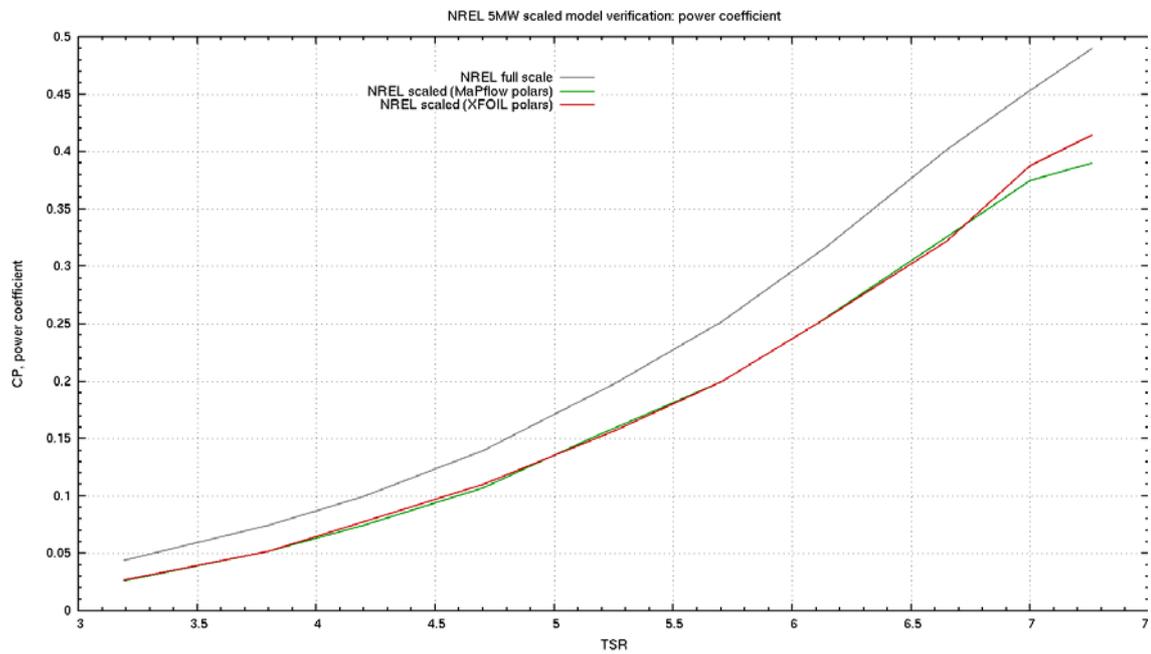
Figure 40: CP variation using the XFOIL and MaPFlow polars for the NREL 5MW WT

INNWIND.EU D4.2.4: Floating Wind Model Tests at ECN and DHI

Table 24: Basic settings

	INNWIND.EU 10MW			NREL 5MW RWT		
	Full Scale	XFOIL	MaPFlow	Full Scale	XFOIL	MaPFlow
Reference TSR (*)	7	7	7	7	7	7
Fixed Pitch setting at rated conditions [º]	6.75	4.64	5.00	1.68	2.20	2.00
Rotational speed at rated conditions [RPM]	9.6	81.2	81.2	12.1	81.2	81.2
(*) This value was kept the same as in the original design						

The above results verify that the scaled rotor is capable of providing CT match to the full scale rotors to which the tests refer to. This conclusion is subjected to the simulation uncertainties related to BEM modeling. This point is relevant not only to the scaled model predictions, but also to the full scaled data used which was also estimated using BEM modeling. Furthermore it has been checked that the different polars used do not affect significantly the matching and the deviations are within the confidence levels BEM modeling offers. Finally, concerning the power performance of the scaled model, the deviation with respect to full scale is significant. This corresponds to an unavoidable compromise which is expected to affect the rolling behavior of the system.

2.9.3 Assessment of the performance using CFD

In this section results from 3D simulations at rated conditions are presented. Two solvers are used: the MaPFlow[1] CFD solver and the GENUVP[2] vortex one, and the results are compared. This comparison aims on one hand at cross checking the BEM results and on the other at determining the deviations between CFD and vortex aerodynamic modeling. This is relevant to the assessment of the effect of the jet inflow which is carried out using the vortex model. Restricting the analysis to rated conditions is justified by the fact that rotor has variable speed and pitch. This means that at conditions below rated the normalized performance characteristics will be identical to those at TSR=7 while at above rated the pitch schedule will lead to lower aerodynamic loading.

For the CFD simulation, a surface grid of 300 cells in the chordwise and 184 in the spanwise directions was used while the 3D grid amounted to a total of 6.5 million cells. The cell size followed a geometrical progress increase from the blade and outwards starting with a cell of Y+<1.

---

[1] MaPFlow is a multi-block MPI enabled compressible solver equipped with preconditioning in regions of low Mach flow. The discretization scheme is cell centered and makes use of the Roe approximate Riemann solver for the convective fluxes. In space the scheme is 2nd order accurate defined for unstructured grids and applies the Venkatakrishnan's limiter. The scheme in time is also 2nd order and implicit introducing dual time stepping for facilitating convergence. The solver is equipped with the Spalart-Allmaras (SA) and k-ω SST eddy viscosity turbulence models.

[2] GENUVP is an unsteady 3D inviscid flow solver that combines the panel method with a vortex particle approximation of the wake. The evolution of the wake follows the Helmoltz vorticity equation. Cost reduction is achieved by adopting the Particle-mesh technique and applying a fast Poisson solver. Time integration is 2nd order. Steady state is obtained through converging a sudden start-up of the flow and following the gradual built-up of the wake.

INNWIND.EU D4.2.4: Floating Wind Model Tests at ECN and DHI

For the vortex simulation, a surface grid of 49 x 47 points was used. The grid covers the spam from r=0.167m to tip over which the airfoil RG14 is extended. The time step of the simulations corresponds to 5º of azimuth angle.

In Figure 41 indicative surface loading distributions are given at three radial stations. In terms of surface pressure loading, there is fair agreement. Taking into account that the vortex model is inviscid, deviations in suction peak at the level shown are expected. The differences seen at the trailing edge are artifacts. In the vortex model the pressure Kutta condition is satisfied at the closest to the TE control point which is at non-zero distance from it. Increasing the number of panels in the chordwise direction will minimize the differences.

In terms of spanwise loading, the comparison is shown in Figure 42 and Figure 43 while in Table 25 the different rotor performance predictions are given. The axial force distributions along the blade span as obtained from CFD and vortex modeling agree fairly well in accordance to the surface pressure results. On the other hand, as expected, the driving force distributions are different due to the lack of viscous effects in the vortex simulations. In particular in the tip region the vortex model predicts higher driving force which explains the difference in the rotor power coefficient given in Table 25 Concerning the thrust force which is the key quantity in the present context, there is good agreement. CFD predicts slightly smaller value compared to that of BEM. In terms of power coefficient, the CFD value agrees with that of BEM using the MapFlow polars while the vortex prediction is significantly higher since the model lacks friction and so it is expected to approach the Betz limit.

Table 25: Comparison of performance at rated operational conditions

	BEM results (hGAST)	Vortex results (GENUVP)	CFD results (MaPFlow)
Rated CT	0.675	0.684	0.665
Rated CP	0.389 (XFOIL polars) 0.376 (MaPFlow polars)	0.523	0.375

Pressure distribution at r/R=0.35 (r=0.5m)   Surface friction distribution at r/R=0.35

Pressure distribution at r/R=0.6 (r=0.84m)   Surface friction distribution at r/R=0.60

Pressure distribution at r/R=0.9 (r=1.26m)   Surface friction distribution at r/R=0.90
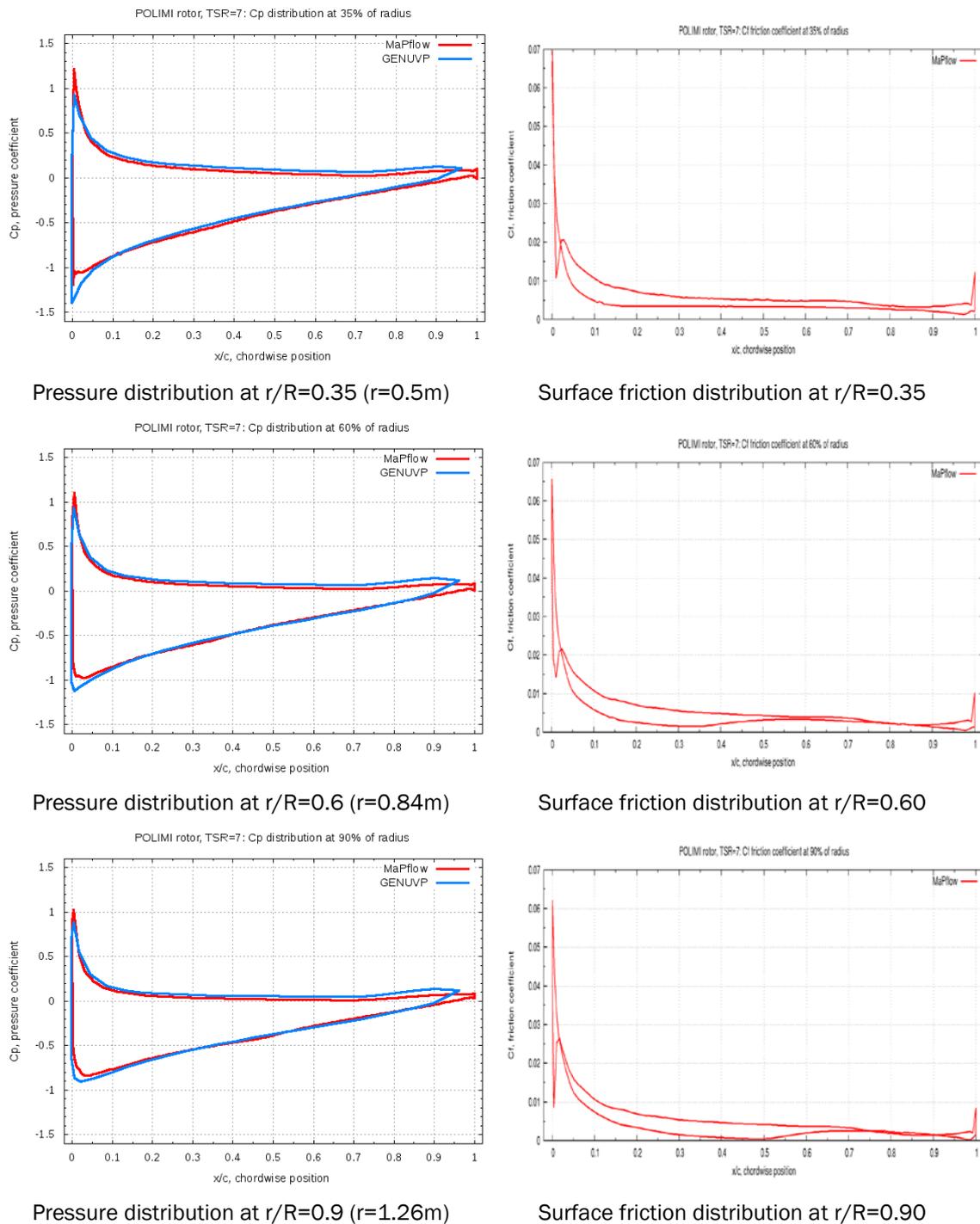
Figure 41: Surface loading results. Pressure and skin friction distributions at three radial stations are given and comparison between CFD (MaPFlow) and vortex (GENUVP) is carried out

Based on the above comparisons it can be concluded that the BEM calculations can be considered reliable and so do the flow characteristics given by the vortex model under attached flow conditions. The latter is confirmed by plotting the surface liming lines over the suction side obtained from the CFD simulation (Figure 44). In the root region flow separation is very limited

while there a small separation bubble is seen close to the tip. Having separation in the tip region is unexpected and further investigation should be made in order to exclude the possibility of seeing an artifact due to numerical reasons. It is noted that there is no experience with rotors at so low Re numbers.
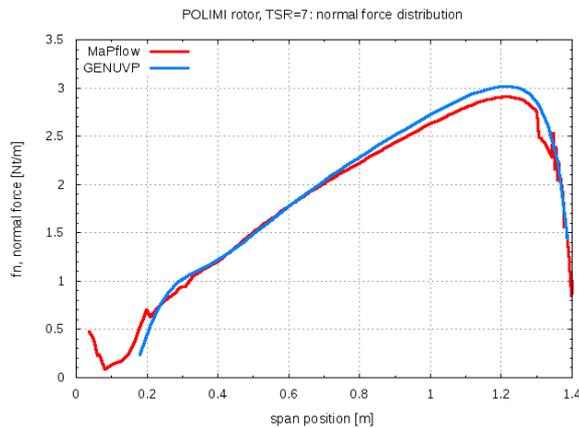
Figure 42: Axial force radial distributions
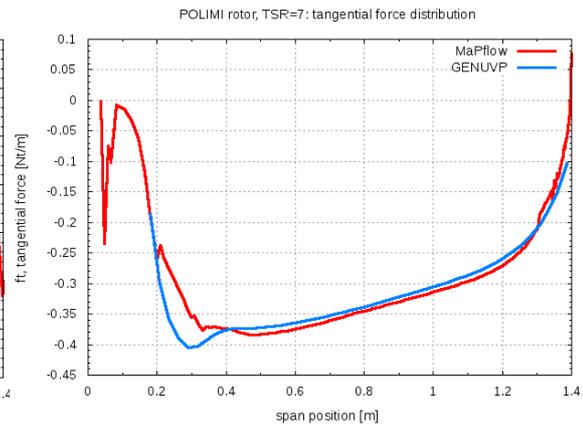
Figure 43: Driving force radial distributions

Root region

Tip region
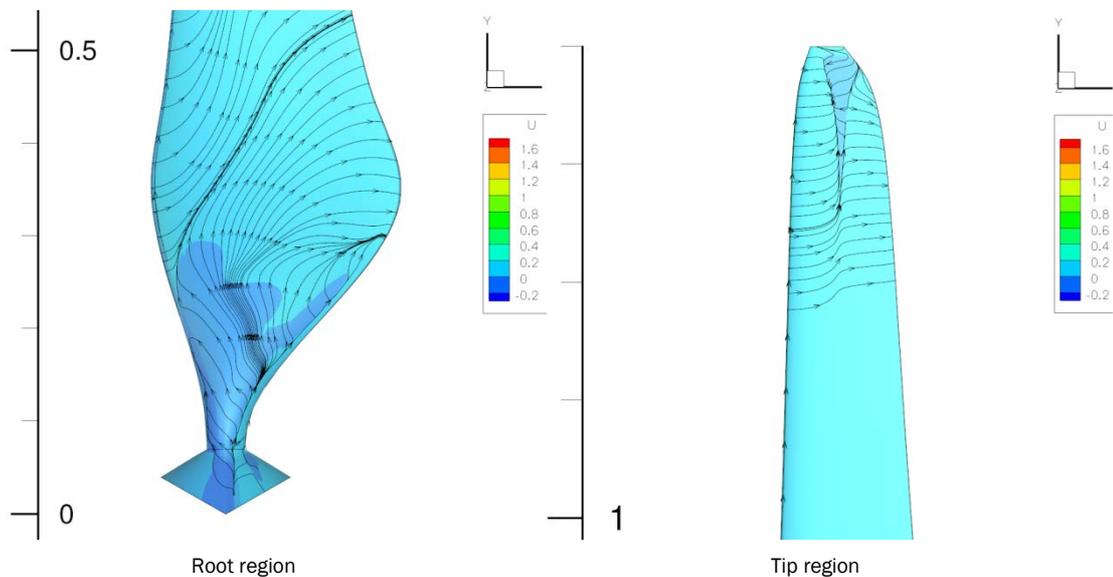
Figure 44: Flow field characteristics of the scaled rotor at rated conditions (TSR=7. Pitch=2.5). Surface stream traces over the suction side of the blade are shown together with the in plane velocity (Ux)

2.9.4 Assessment of the "jet inflow issue"

In this section the effect of the jet inflow on the aerodynamic performance of the rotor is examined using the vortex model GENUVP in which the jet flow is represented by a deformable vortex sheet. The rotor is located 4m downstream from the nozzle exit and the whole system (nozzle, the jet-inflow shear and the wind turbine) is modeled as shown in Figure 46. The time step in this simulation corresponds to an azimuth increase of 10°.

Numerical set up: nozzle, jet-inflow shear and wind turbine	Schematic view of the flow evolution (same notations as in Figure 34).
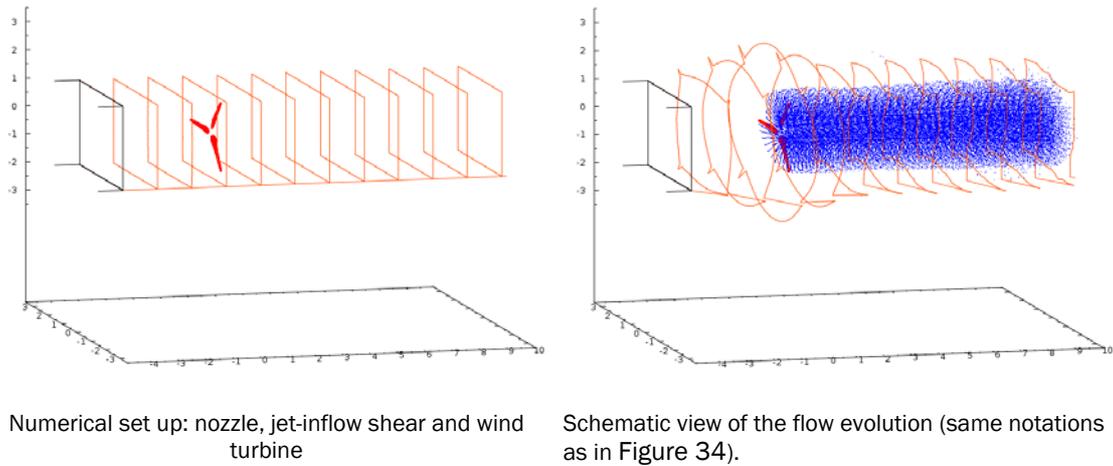
Figure 45: Numerical set up and schematic view of the flow development

As already noted with respect to the MEXICO experiment the presence of the rotor will force the jet flow to expand resulting lower rotor loading. In Figure 46 this expansion is clearly seen. Compared to that obtained for the MEXICO rotor, the expansion in significantly more pronounced due to the small difference between the rotor diameter and the dimensions of the nozzle. Another difference with respect to the MEXICO experiment which is also believed to be related to the small margin between the rotor and the jet shear, is that the shear contracts downstream of the rotor. In the simulation with jet inflow, the incoming flow is given by the velocity induced by the vorticity distributed on the shear sheet. So by recording only this part of the total velocity, it is possible to quantify the modification of the jet flow due to the presence of the rotor. This is done in Figure 46 where the axial flow induced by the jet shear is shown at various downstream stations. The rotor is placed at x=0. On the rotor plane values less than 1.7m/s are noted while in the wake the axial velocity attains higher values. Note also that at x=5m (1.8D) the effect of rotation is seen as a swirling deformation of the jet cross section.
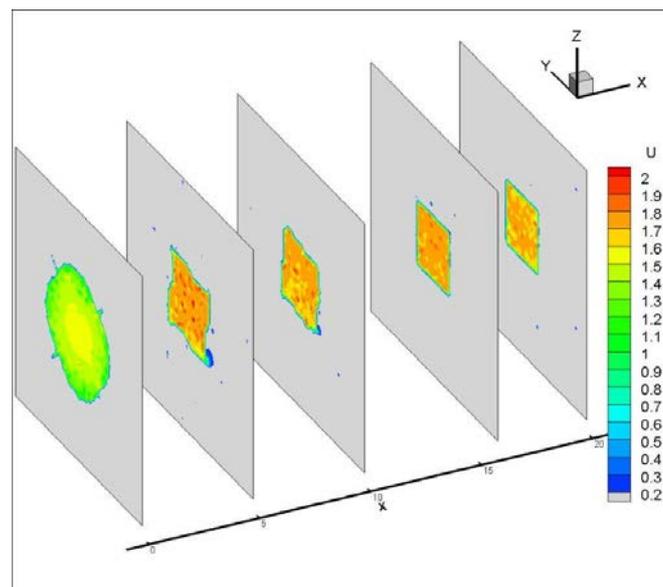
Figure 46: Modification of the axial velocity field induced by the jet shear in the presence of the rotor

The effect on the loading is recorded in Figure 47 - Figure 49. The comparison of the pressure distributions obtained with/without the jet inflow effect is clear and the same is shown in the loading distributions of the axial and driving forces. Another way to quantify this difference is to compare the estimated effective angles of attack. This comparison is important because the effective angle of attack is the key parameter in the BEM aerodynamic modeling. Figure 50 indicates a difference of ~1º over most of the span. During tests such a correction is clearly within the capabilities of a pitch control system and therefore it can be argued that the rotor design is suitable. Of course in order to associate the test results to full scale data requires a correction procedure. It is expected that during the validation process that will be carried next, such a correction methodology could be derived.

Pressure distributions at r/R=0.35

Pressure distributions at r/R=0.60

Pressure distributions at r/R=0.80

Pressure distributions at r/R=0.90
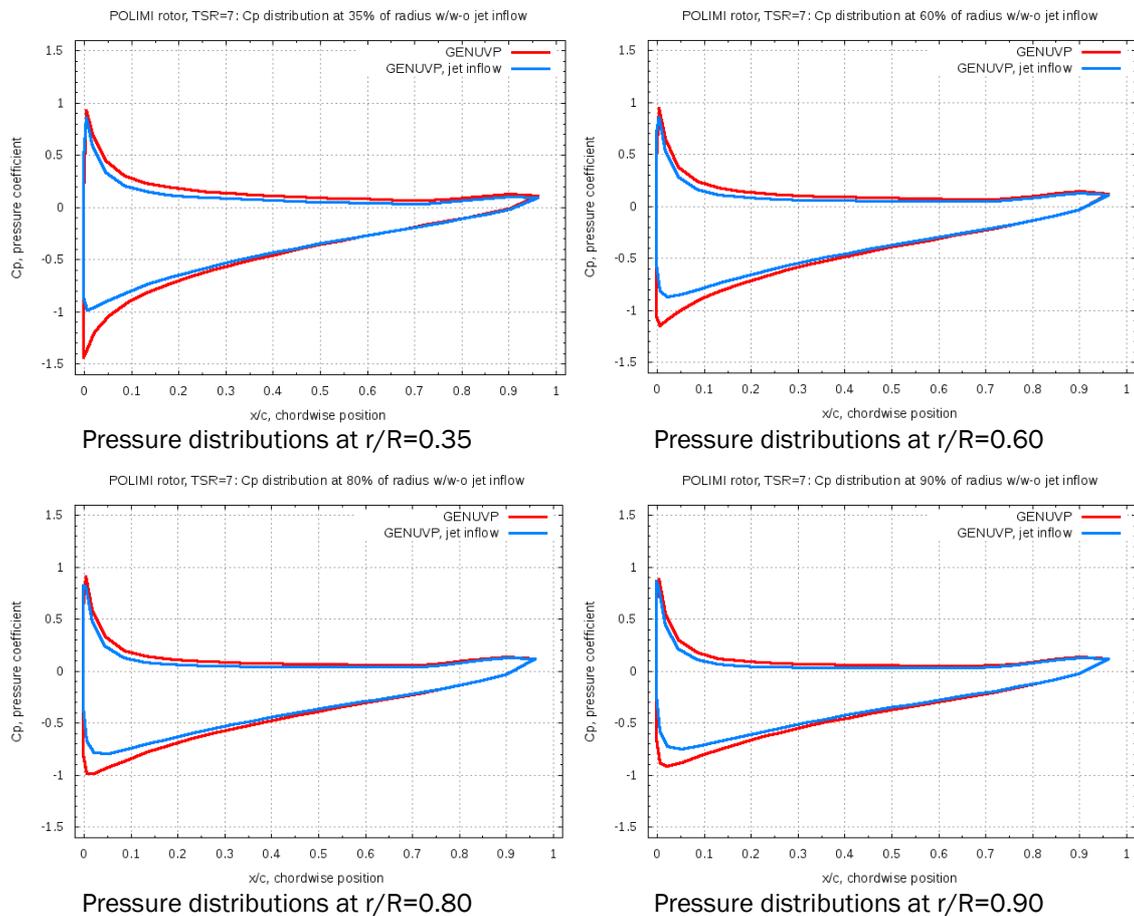
Figure 47: Comparison of pressure distributions with and without the jet inflow effect. Placing the rotor within a jet flow lowers the loading.
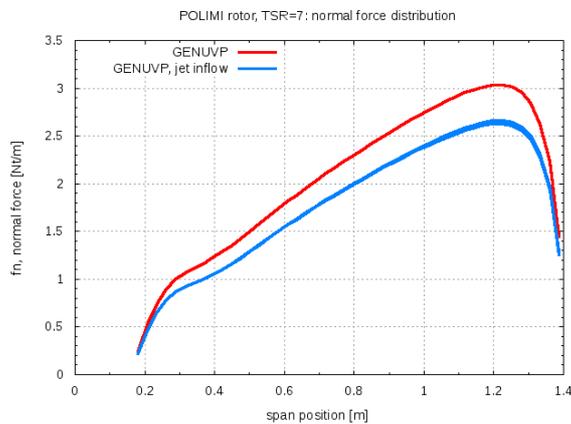
Figure 48: Axial force radial distributions (with/without jet inflow effects)
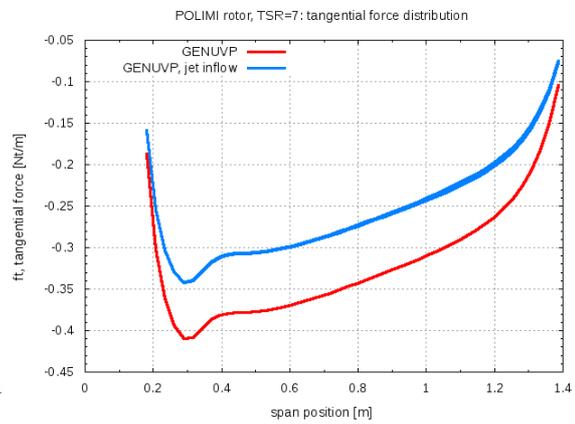
Figure 49: Driving force radial distributions (with/without jet inflow effects)
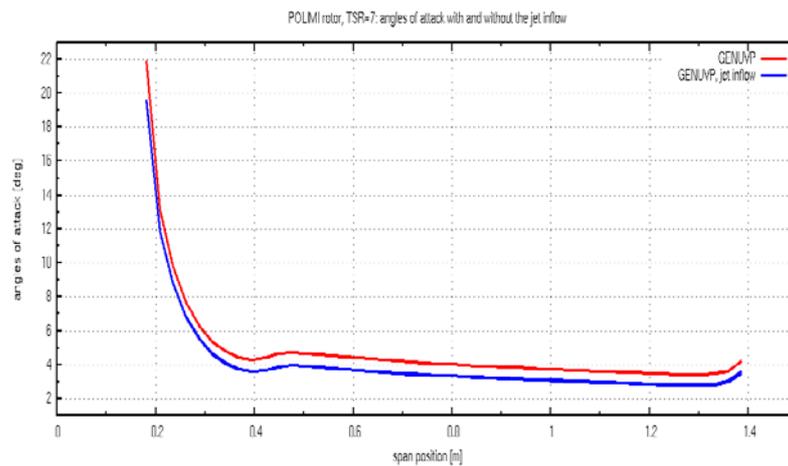
Figure 50: Comparison of the effective angles of attack

2.9.5 Conclusion

With respect to the effect of the jet-inflow on the aerodynamic characteristics of the rotor, the results show that there is a shift of the point of operation towards lower loading. This calls for some attention when associating scaled model results to those at full scale. From a verification point of view, the fact that the effective angle of attack is changing by an almost constant value indicates that the scaled design is correct and that the tests are valid and can be regarded as indicative of the full scale case provided that appropriate corrections are added. Devising a correction formula or strategy was outside the scope of the present deliverable. This will be part of the next deliverable in which the complete configuration will be compared to measurements. Such comparisons will allow assessing the effect of the jet inflow on the floater motions and hydrodynamic loads.

2.10 Sensors

Various sensors and data loggers have been used in the experiments. There are four different data files which collect the signals of each data logger. However, one common trigger signal was used for all sensor systems in order to start the measurements at the same instant of time.

2.10.1 Platform

The platform is equipped with three beam load cells for the measurement of the fairlead tensions (see Figure 51, Figure 52 and Figure 53) and two redundant combined accelerometers and gyroscopes at the overall center of mass, see Figure 56 and in column #2. The data is stored directly on an SD card on the platform and also instantly transmitted through a wireless connection to a stationary PC at a rate of 100Hz. All signals are converted to a digital signal through 15bit ADCs. The microprocessor and the sensors are powered by batteries on the platform, which sustain at least one day of testing. Details can be found in [6].

The beam cells measure the portion of the applied force in perpendicular direction of the beam. Initially it was planned to apply them at a realistic angle of $\theta_{frld} \approx 32\ldots37$ deg following a variety of operational and shut-down full-scale simulations. It was then decided, however, to apply orifices at the location where the fairlead is supposed to be in the full-scale model, which is the edge of the base column. The sensor angle (towards the horizontal) was maintained at $\theta_{frld} = 35$ deg , a wire loop added in week 1 and 2 and an improved set up introduced for week 3 and 4.

The angle of attack of the string towards the load cell can be calculated from the sketches in Figure 54 and Figure 55. The string touches the loop most likely at the outer part of the loop, at least for fairlead 2. The inner diameter of the loop is about 20mm for the improved setting of weeks 3 and 4 and about 10mm for week 1 and 2. The load cells are of the type Bosche B10N. During week 1 and 2 they were of a capacity up to 5kg. It turned out that, at least during installation, higher loads can occur and so the first sensors were replaced by the same model but with strain gages that stand up to 50kg. Therefore, different calibration curves have to be applied. They can be found in the attached Excel file "DataIndex_INNWIND_ECN1409.xlsx" and in Table 26, where x is the measurement raw data.

Table 26 - Fairlead sensor calibration factors.

Sensor	Week 1/2	Week 3	Week 4
1	(x-5195)/4.39573/1000*9.80665	(x+577)/322.277829	(x+1621)/324.64
2	(x+353)/4.278239/1000*9.80665	(x+458)/320.972631	(x-851)/322.27
3	(x+109)/4.37059185/1000*9.80665	(x+1326)/324.673181	(x+2508)/323.87
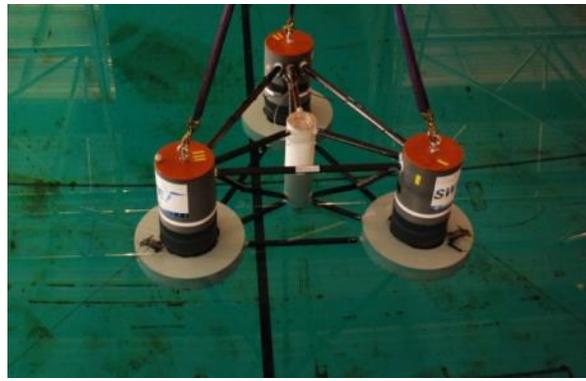
Figure 51 - Fairlead sensors, week1/2.

Figure 52 – Fairlead sensors, week3/4.   Figure 53 - Fairlead sensors, week3/4.

During week 1 and 2 it was found that the applied wires would not sustain the loads in the front line (#2) and therefore they were bent up. Out of this reason the wires were removed on October, 2nd in the morning. Therefore, the strings are free to take their shape without any other constraint from their attachment point at the end of the beam cells for the most part of week 2.
At the end of week 2 it turned out that the beam cell #2 was bent downwards to an angle of about 20deg. The exact time of this will have to be found from the measurements.

INNWIND.EU D4.2.4: Floating Wind Model Tests at ECN and DHI
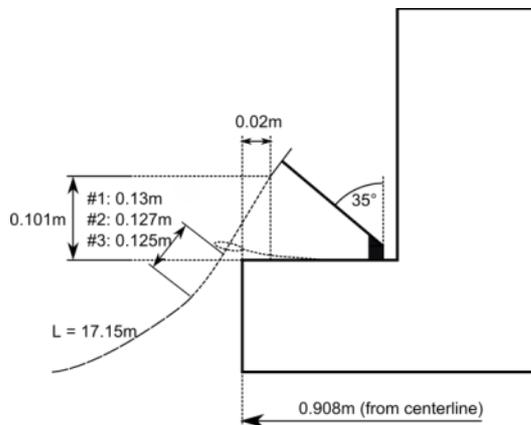
Figure 54 – Fairlead sensor sketch, week1/2.   Figure 55 - Fairlead sensor sketch, week3/4.
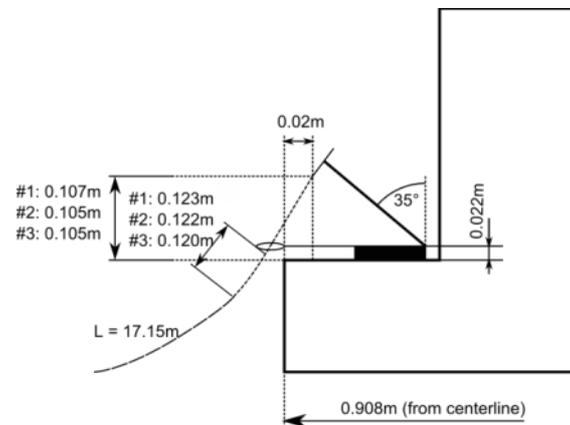
Figure 56 shows the MPU-6050 six-axis accelerometer and gyroscope (IMU). It outputs accelerations and rotation rates in the local coordinate system as 16 bit values. The sensitivity was set to +-250 °/s and +-2g which is the lowest possible. An integrated algorithm to convert the raw data to Quaternions or Euler angles has not been used in this test. The calculation of the rotation angles from the raw data has been made in the postprocessing. Therefore the yaw angle drifts a lot, because it cannot be stabilized by the acceleration data. There is, however, also the position signal from the Qualisys motion tracking system available, see Section 2.10.5.

The sensor offsets were adjusted on the chip by software, therefore the 16 bit values only have to be divided by the gain factor to get the raw data. This factor is 131 for the rotation rate to get the unit [deg/s] and 1670.7 for the accelerometer to get the unit [m/s^2].

Figure 56 – MPU-6050 six-axis gyroscope + accelerometer.

The effect from the buoyancy forces acting in vertical direction on the fairlead sensors has been measured before connecting the mooring lines before each test session (week 1 and week 3).

2.10.2 Low-Reynolds Rotor

The Froude-scaled rotor, the nacelle and the tower, set up by Politecnico di Milano, contain various sensors, namely the blade pitch angle, rotor speed, power, the shaft bending moment about the rotating nodding and yawing axes, the generator torque, the rotor azimuth angle and the tower base fore-aft and side-side bending moment.

The pitch angle of every blade has been measured with the built-in encoder of the pitch actuator (Faulhaber 1724T018SR brushed motor, equipped with a 16/7-134:1 precision gearhead and IE2-512 encoder). The gearhead backlash (approx. 1 [deg]) was removed by using a torsional

spring connecting blade root and rotor hub, thus ensuring good repeatability of the blade pitch measurements with an acceptable accuracy of about ±0.1 [deg].

The rotor azimuthal position is measured by an optical incremental encoder with N_p=1800 counts per revolution; a zero-index track is used for providing the absolute rotor azimuth. The quadrature signal is read in 4X counting mode, and the rotor speed is computed based on the number of observed pulses within a time window T_{sc}=4 [msec].

Shaft load measurements (see Figure 53) are obtained by strain gages mounted on small bridges, machined directly from the hollow shaft just aft of the hub and sized so as to be subjected to sufficiently high strains. These load transducers were calibrated by using dead weights to stress the shaft simultaneously with torque and two bending moment components. A full 3-by-3 sensitivity matrix was obtained by linear regression, leading to the good quality measurements.
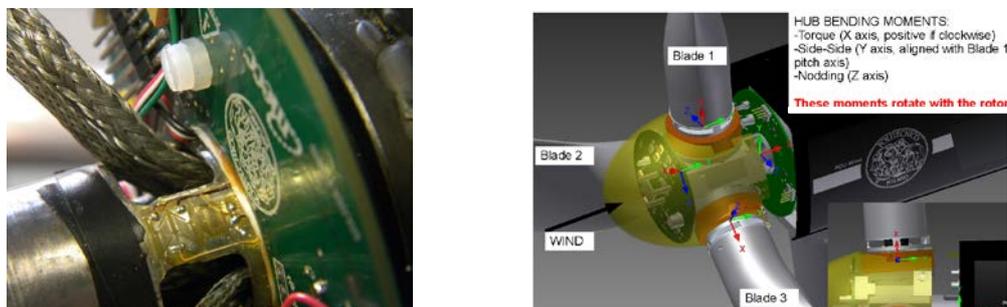
Figure 57 Shaft loads measurements with Low-Reynolds rotor

Tower base bending moments transducers (see Figure 58), again obtained by using strain-gages mounted on the external tower surface and encapsulated within a water-proof shell, were similarly calibrated using known dead loads. After having verified the insensitivity of the transducer measurements to other loading conditions, a full 2-by-2 sensitivity matrix was obtained by linear regression.
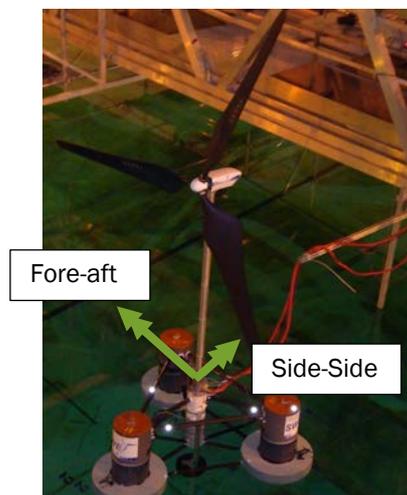
Figure 58 Tower base loads measurements

Onboard sensors are used for collecting data on the behavior and response of the model during experimental observations. The experimental model is controlled by a Bachmann M1 hard-real-time module implementing a supervisor of the machine states, similarly to what is done on a real wind turbine. Three analogue acquisition modules and one counter module acquire all model onboard sensors at a sampling frequency of 250 [Hz]. Shaft loads are sampled at 2.5 [kHz].

All sensor readings are provided as inputs to the supervision and control algorithms, which is executed in real-time on the M1 CPU unit every 8 [msec]. The controller outputs are represented

by pitch and torque demands, which are sent to the actuator control boards via the M1 CAN module.

2.10.3 Ducted fan

The ducted fan was installed on top of the tower built by POLIMI, therefore the same sensors were used to measure tower base moments. Though no more real sensors were installed, several signals from the acquisition system and simulation software were stored:

- The positions of the 6 degrees of freedom of the platform acquired by the Qualisys system and used as an input for FAST
- The velocities of the 6 degrees of freedom of the platform, obtained by derivation of the positions
- The demanded aerodynamic force computed by the software
- The FAST software simulation outputs

2.10.4 Wind/Waves

Three wave probes (WP) are installed in the wave basin around the initial platform position. Their location with respect to the wind outlet and the initial platform position can be found in Figure 59. In week 3 two anemometers (A) have been installed in front of the outlet close to the upper end (A#1 and A#2) mainly as a reference for CFD calculations, see Figure 59. The anemometer used in week 1 and 2 was downwind of the rotor and therefore the measured wind speed may not be representative. Unfortunately, the exact locations of the anemometers were not provided by the *LHEEA*. Table 27 shows the approximate positions.
During week 3 detailed measurements of the jet and its boundary layers have been done with an ultrasonic device. For calibration of the wind generator, both anemometers were placed in front of the outlet at the top end, as it is sketched in Figure 59. Later they were placed at the lower left corner and the upper left corner of the outlet during the tests. For the identification of the jet ultrasonic measurements without rotor have been performed. Its location is also given in Table 27.
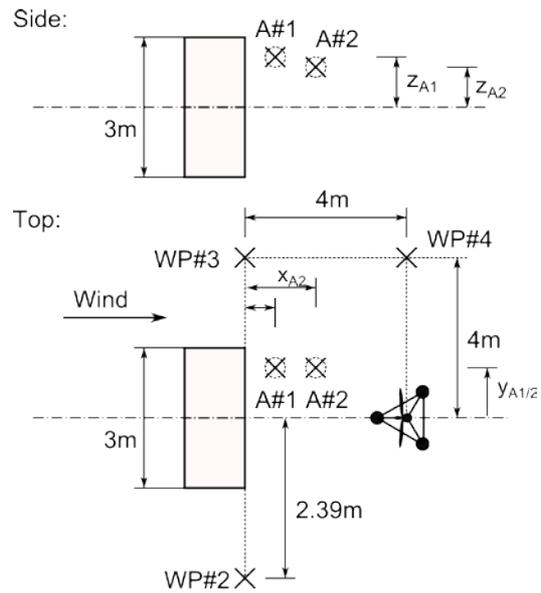
Figure 59 – Sketch of wave probes and anemometers.

Table 27 – Anemometer and wave probe positions.

Sensor	Week 1/2	Week 3/4
A1	$x_{A1} \approx 5m$ $y_{A1} = 0m$ $z_{A1} \approx 1m$	$x_{A1} \approx 0.2m$ $y_{A1} = -1m$ $z_{A1} \approx 2.9m$
A2	-	$x_{A2} \approx 0.2m$ $y_{A2} = -1m$ $z_{A2} \approx 2.9m$
Ultrasonic		$x_U \approx 5.0m$ $y_U = 0m$ $z_U \approx 2,6m$

INNWIND.EU D4.2.4: Floating Wind Model Tests at ECN and DHI

Figure 60 – General view of the scaled model

INNWIND.EU D4.2.4: Floating Wind Model Tests at ECN and DHI

2.10.5 Motion Tracking System

A camera motion tracking system is available at LHEEA, which has been used for all testsAnd consists of 18 ProReflex cameras with a sampling frequency up to 120Hz and a precision of 1.2mm at a distance of 35m. The cameras track three reflective spheres on the platform (rigid body motion). 3-D motion can be tracked with an accuracy that depends on the placement of the spheres on the body relative to the cameras and also the visibility depending on the current position. The reliability of the measurements is indicated by the "Data_Available" channel in the text files produced by the system.

The location of the platform reference point (overall center of mass) with respect to the spheres has been erroneous during week 1 and 2. The radius of the sphere of 15mm has to be added in the positive local z-direction to the platform reference point.

2.11 Test Runs

In total four weeks of model testing were spent at the LHEEA of Ecole Centrale de Nantes during 2014. The first slot was from September 22 to October 3 and the second slot from October 29 to November 6. An overview of the tests performed is provided in Table 28.

<div align="center">Table 28 - Overview on INNWIND.EU test slots.</div>

Period	Model configuration	Performed tests
22.9 – 26.9 (week 1)	Platform without wind turbine, ballast adjusted to match overall center of mass.	Static displacement (mooring forces), free decay, regular waves, irregular waves, white noise
29.9 – 3.10 (week 2)	Froude-scaled rotor mounted on platform. Ballast shifted underneath the platform, see Section 2.3.	Free decay (w/ and w/o wind, w/ and w/o data & power cables), regular waves (w/ and w/o wind), wind (no waves), irregular waves (w/ and w/o wind), 45 deg wave heading
29.10 – 3.11 (week 3)	Froude-scaled rotor mounted on platform. Ballast shifted underneath the platform, see Section 2.3.	Yawed inflow, static displacement (mooring forces), 45deg waves, wind (no waves/ regular waves) for CFD, shortened lines, irregular waves and wind, white noise, survival conditions, deterministic wave
4.11 – 6.11 (week4)	Ducted fan on tower mounted on platform. No shifted ballast.	Regular waves (w/ and w/o thrust), irregular waves (w/ and w/o thrust), free decay w/ thrust …

Tests for identification of the system as well as tests under realistic conditions have been performed.

For the identification of the mooring characteristics the platform has been brought to various displacements in x- and y-direction using a string, attached to the overall center of mass of the

platform at 0.2198m below SWL in order to obtain the static forces on the mooring sensors. Free decay tests with the mooring lines attached have been performed. Also with and without wind in order to see the effect of the aerodynamic damping. For identification of the influence of the data and power cables of the Froude-scaled rotor a pitch-free decay has been performed with disconnected cable.

Before the Froude-scaled rotor was mounted platform-only tests have been performed in week1, see Table 29. In order to maintain the center of mass additional ballast representing the wind turbine was introduced and all dumbbell disks have been shifted upwards.

Table 29 - External conditions week1

	Regular/Irregular waves		Steady Wind Speed (m/s)
	Hs (m)	Tp (s)	
Sea State #1	0,061	0,820	1,04
Sea State #2	0,070	0,969	1,27
Sea State #3	0,092	1,088	1,70
Sea State #4	0,108	1,327	2,68
Sea State #5	0,133	1,491	3,73

With the Froude-scaled rotor numerous tests have been performed with wind and waves only and combined situations with irregular, regular and white noise waves, see Table 30. The wave height was adjusted with respect to the wave period in order to achieve a constant wave steepness of 5% of the breaking limit. The wave height is approximated as

$$H = 0.05 \frac{gT^2}{2\pi}.$$
(8)

Also a wave heading direction of +45deg was tested and yawed inflow, where the turbine was mounted on the platform with an angle of +13.5deg. In order to better identify possible errors in the model mooring system, the lines have been cut by 5 links and static displacement as well as regular wave tests were performed. A deterministic wave as well as survival conditions with high wind speeds and harsh sea states were tested. For the calculation of RAOs white noise waves with and without wind were tested.

Table 30 - External conditions week2

	$\lambda = 45$			$\lambda = 60$		
	Hs (m)	Tp (s)	Wind (m/s)	Hs (m)	Tp (s)	Wind (m/s)
Sea State #1	0,052	0,820	1,043	0,039	0,710	0,9
Sea State #2	0,073	0,969	1,267	0,055	0,839	1,1
Sea State #3	0,092	1,088	1,699	0,069	0,942	1,5
Sea State #4	0,137	1,327	2,683	0,103	1,149	2,3

In week 3 the remaining tests with the Froude-scaled rotor were performed. In order to avoid many different sea state with very close wave periods for the two different scaling ratios only one set of sea states and wind speeds was tested, see Table 31.

INNWIND.EU D4.2.4: Floating Wind Model Tests at ECN and DHI

Table 31 - External conditions week3

	Regular/Irregular waves		Steady Wind Speed (m/s)
	Hs (m)	Tp (s)	
Sea State #1	0,04	0,70	0,90
Sea State #2	0,06	0,90	1,48
Sea State #3	0,09	1,10	2,30
Sea State #4	0,13	1,29	2,63
Sea State #5	0,17	1,49	3,20

Table 32 - Survival conditions (week3)

	Survival conditions		Wind speed (m/s)
	H (m)	T (s)	
Sea State #1	0,18	2,30	7,00
Sea State #2	0,23	2,00	7,00

All test runs start at an equilibrium position. Only after the measurements have been started the wind and wave generators were turned on.
In week 4, similar conditions as in week 1 were tested:

Table 33 - External conditions week 4

	Regular/Irregular waves		Steady Wind Speed (m/s)
	Hs (m)	Tp (s)	
Sea State #1	0,070	0,969	1,27
Sea State #2	0,092	1,088	1,70
Sea State #3	0,108	1,327	2,68
Sea State #4	0,13	1,29	2,68

In addition, an extreme wave condition (regular and irregular) with no wind was tested. The objective of this condition was to evaluate the effect of mooring dynamics on the platform motions:

Table 34 - Survival conditions (week 4)

	Survival conditions	
	H (m)	T (s)
Sea State #1	0,2	3,13

2.12 Selected Results

Figure 61 and Figure 62 - Pitch free decay with cables (Froude-scaled rotor) show selected results for a pitch free-decay test of the platform with the Froude-scaled rotor mounted on top from week

2. The effect of the cables is assessed through this comparison, where Figure 61 shows the results for disconnected cables.
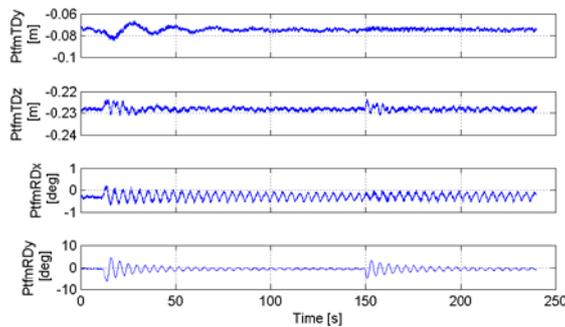
Figure 61 – Pitch free decay without cables (Froude-scaled rotor).
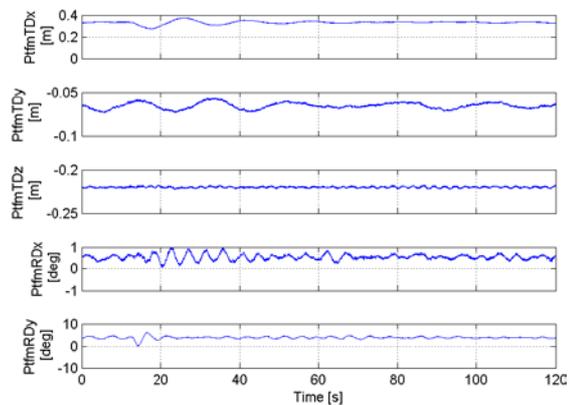
Figure 62 - Pitch free decay with cables (Froude-scaled rotor).

Figure 63 compares 4 different free decay tests in pitch performed with 4 different wind conditions and using the coupled fan system to model the wind thrust. In the case with "no wind" the fan is not connected and, therefore, the wind loading is zero. The other cases correspond to wind constant velocities of 8.5m/s, 11.4m/s and 18m/s in full scale (scale factor 1/45). The plot shows that the minimum damping appears in the "No Wind" case, and the maximum damping corresponds to the case with 11.4m/s of wind that is the rated wind speed, and also the condition where the aerodynamic thrust is the maximum.

2.13 Acknowledgements

INNWIND.EU D4.2.4: Floating Wind Model Tests at ECN and DHI
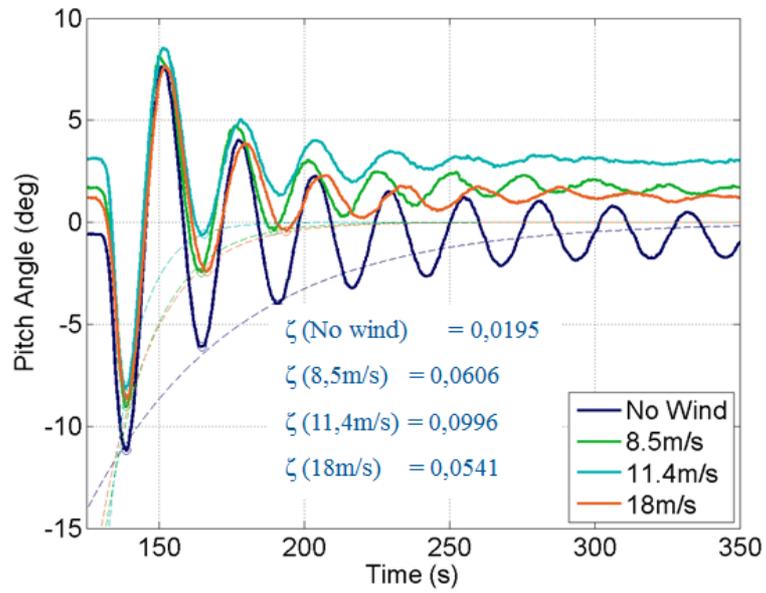
Figure 63 – Comparison of pitch free decay tests with different constant wind speeds modelled by the coupled fan system.

INNWIND.EU D4.2.4: Floating Wind Model Tests at ECN and DHI

3. TLP TEST CAMPAIGN

The second test campaign was carried out at DHI Denmark in December 2014 (1 week) and January 2015 (4 weeks). The tests extend the results of the first campaign by

- Application and design of another floater type (TLP) with different dynamic properties than the semi-submersible concept
- A re-designed 1:60 Low-Reynolds number rotor that is based on the DTU/INNWIND.EU 10MW rotor
- Tests with 3 different mooring configurations
- Tests with directionally spread waves
- Tests in mis-aligned wind-wave conditions
- Tests with focused waves, as a model for extreme waves

The test campaign and its results have been reported in detail in [16] and presented orally at the EWEA Offshore 2015 conference [17]. The report [16] is provided as a separate attachment for full documentation. The present chapter is an extracted summary from this report.

3.1 Floater concept and coordinate system

The TLP floater concept is radically different from the semi-submsersible floater by its compact volume and the attainance of stability by the mooring system. The mooring configuration is based on a strong excess buoyancy which makes the floater response much stiffer (higher natural frequencies) than the semi-submersible. The associated change in dynamic behaviour makes the TLP concept interesting to study as an alternative to the semi-submersible floater.
Further, it is noted in [18] that the anchoring system of TLPs may be better suited for shallow waters than the catenary mooring system of a semi-sub, and that the limited platform motions of the TLP may reduce turbine and power cable fatigue loads.
In the study of [19] it was estimated that TLP type foundations are among the most competitive floating foundation designs of today, mainly driven by low production costs which make it up for slightly higher installation costs due to expensive anchoring.
The TLP floater for the present experiments was designed specifically for the DTU 10MW turbine. A simple geometry was chosen, as a detailed and optimized design of this structure is not the aim of the present work. This further eases construction of the model scale foundation and simplifies the numerical modelling of the floating wind turbine.The foundation consists of a cylindrical transition piece, a cylindrical floater and slender spokes, as sketched in Figure 64. The TLP is sketched with four tendons, but tests with also three spokes (n_s =3) were carried out. The floater was designed for a water depth of $h = 180$ m, to match the basin water depth of 3.0 m for the 1:60 scale model tests.
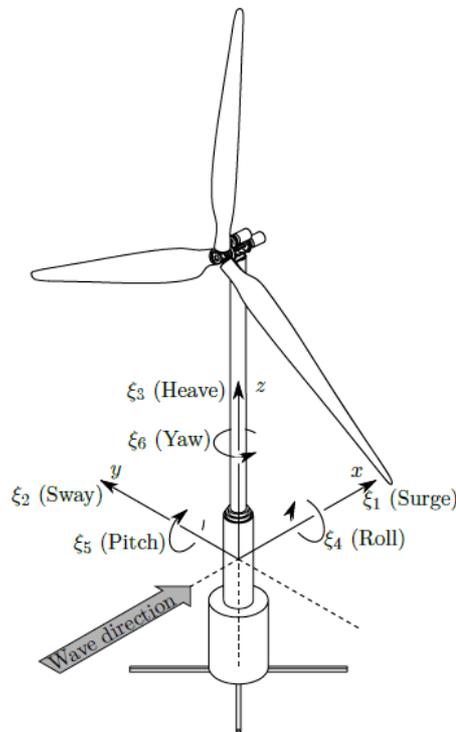
Figure 64 - TLP floater, coordinate system and the six motion components.

The global (x, y, z)-coordinate system is located at the position of the unloaded structure, with $z = 0$ in the mean water level (MWL) and the z-axis pointing upwards. The x-axis is coincident with the primary wave direction. Rigid body displacement in the positive directions of the x, y and z-axes, are denoted surge, sway and heave, while rotations about the same axes are denoted roll, pitch and yaw in accordance with general maritime terminology. These motions are denoted $\xi_1, \xi_2, \xi_3, \xi_4, \xi_5$ and ξ_6. Further, a body fixed coordinate system, (x_b, y_b, z_b), is defined such that it coincides with the global coordinate system, when there are no external loads on the structure.

3.2   Dynamic-elastic scaling

The experiments where carried out in scale 1:60. The scaling of mass, length and time follows the Froude-scaling law as desribed in INNWIND.EU Deliverable D4.22 [2], see also [20]. The scaling principles are described in Annex 7.1 and are summarized in Table 35.

The scaling allows for conservation of the Froude number and thus the right balance between gravitational and inertia forces. This way, dynamic similarity can be achieved at the expense of a smaller Reynolds number (balance between viscous and inertia forces). This leads to the need for a re-design of the rotor as will be described in section 3.4.

Table 35 - Scaling factors for relevant parameters.

INNWIND.EU D4.2.4: Floating Wind Model Tests at ECN and DHI

Description	Prototype dimension	Model dimension
Length	l_p	$\lambda^{-1} l_p$
Mass	m_p	$\lambda^{-3} m_p \dfrac{\rho_m}{\rho_p}$
Time	t_p	$\lambda^{-1/2} t_p$
Frequency	f_p	$\lambda^{1/2} f_p$
Velocity	u_p	$\lambda^{-1/2} u_p$
Acceleration	a_p	a_p
Angle	ϕ_p	ϕ_p
Angular velocity	ω_p	$\lambda^{1/2} \omega_p$
Angular acceleration	α_p	$\lambda \alpha_p$
Forces	f_p	$\lambda^{-3} f_p \dfrac{\rho_m}{\rho_p}$
Moments	M_p	$\lambda^{-4} M_p \dfrac{\rho_m}{\rho_p}$
Bending stiffness	EI_p	$\lambda^{-5} EI_p \dfrac{\rho_m}{\rho_p}$

3.3   Scaled model description

3.3.1   Floater construction

The floater consists of the main floater tube, the transition piece and the spokes. Discs at the top and bottom of the floater tube and transition piece serve as mounting surfaces for the spokes, the tower and for linkage between the floater tube and the transition piece. In Figure 65 the assembled floater is shown with 3 and 4 spokes, respectively.

INNWIND.EU D4.2.4: Floating Wind Model Tests at ECN and DHI
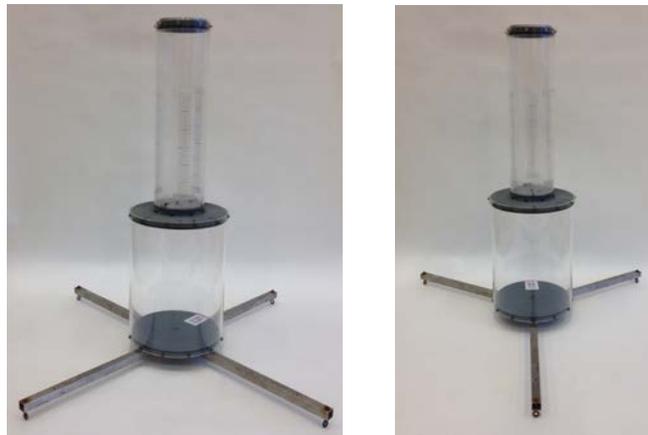
Figure 65 - Assembled floater with 3 and 4 spokes.

A tube of acrylic glass with a diameter of 300 mm and a thickness of 6 mm was used for the floater, while a tube of acrylic glass with a diameter of 150mm and a thickness of 3 mm was used for the transition piece. Discs at the bottom and top of the floater tube and transition piece tube were made from a 20 mm PVC plate. PVC is a rather low weight solid material and by using M8 bolt and drilling the holes 15 mm in depth the assembled floater was considered sufficiently robust. A disc of acrylic glass was mounted at the intersection between the floater tube and the transition piece, constituting a platform for later installation of accelerometers.

By having a transparent floater it is easy to check for leakages and to check that the instrumentation is oriented correctly. Stickers are added to the transition piece in order to identify the point of flotation. Screws of brass were used for assembly to minimize corrosion.

3.3.2   Mooring configurations

In a previous study at DTU [21], [22], a great effect on the response of a 1/200 scale model of a 5MW wind turbine was observed, when introducing an inclination of the tendons. Further, TLP foundations with both three and four spokes are reported in the literature, see e.g. the numerical study [18] and the experimental work [23] and [24]. Hence, it was chosen to define three different structures with different mooring configurations, sketched in Figure 66, based on the chosen floater and transition piece design. The three mooring configurations are denoted structure 1, structure 2 and structure 3.

INNWIND.EU D4.2.4: Floating Wind Model Tests at ECN and DHI
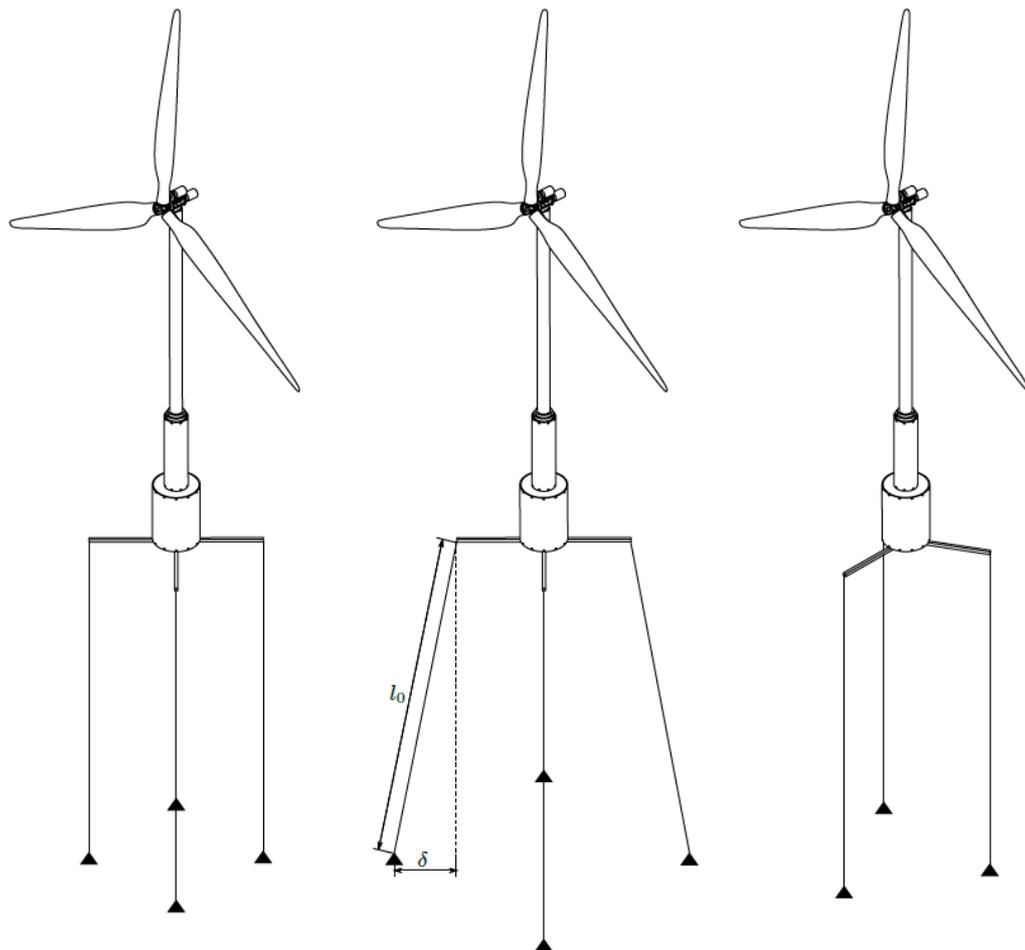
Figure 66 - Sketch of the three applied structures. Left: structure 1, center: structure 2, right: structure 3.

Structure 1 has four spokes, and four vertical tendons, and thus the mooring configuration resembles that of the experimental studies [22] (configurations A and B) and [24] and that of the numerical studies of [25] and [18] (baseline designs 1, 4 and 5). The spokes are oriented such that the wind direction is right between the two upwind tendons. Since this mooring configuration is simple and often observed in the literature, this structure was considered the base case of the present experimental study.

Structure 2 has four spokes and four tendons that are inclined towards the tower with an angle of 9 deg, which means that their intersection is located 43 m above the hub level. This inclination was chosen based on some practical limitations in model scale, and no further analysis of an optimum angle has been considered. The tendon inclination entails a rotation of the WT tower against the floater displacement, which for the defined DOF means that negative pitch is accompanied by positive surge and vice versa, while positive sway is accompanied by positive roll. This will be observed as a 180deg phase shift between the surge and pitch motion, while sway and roll will be in phase. Having inclined tendons, this structure resembles tendon configuration C in [22], which was observed to have a strong coupling of pitch and surge and to have a beneficial dynamic behaviour in harsh sea states. Based on these findings, it was chosen to test the inclination of tendons in this more sophisticated experimental setup. The spokes of this structure are oriented as for structure 1, such that the wind direction is right between the two upwind tendons.

INNWIND.EU D4.2.4: Floating Wind Model Tests at ECN and DHI

Structure 3 has three spokes, where one is parallel to the wind direction, and this structure is moored by three vertical tendons. Hence, this mooring configuration resembles that of baseline designs 2 and 3 in [18]. This structure was chosen, since it is recommended in [26] to have three spokes for easier installation.

To determine the primary hydrodynamic properties of the three chosen structures, they were analysed using software WAMIT. Since the spokes are not modelled in WAMIT, the foundation geometry in these simulations of the three structures are equal, and thus the simulations of the three structures only differ in the external mass and external stiffness.

Based on this analysis, the undamped natural frequencies of the rigid body modes can be determined by solving the well-known eigenvalue problem:

$$(\mathbf{M} + \mathbf{A})\omega^2 = \mathbf{C}$$

(9)

where $\mathbf{M}$ and $\mathbf{A}$ are the mass and added mass matrices, and $\mathbf{C}$ is the stiffness matrix, holding both the hydrostatic and external stiffness contributions. The resulting natural frequencies are given in Table 36 for the three prototype structures.

Table 36 - Prototype natural frequencies from WAMIT simulations for the three structures.

Prototype natural frequencies [Hz]			
Structure	Surge	Heave	Pitch
1	0.027	1.32	0.57
2	0.030	1.30	0.50
3	0.027	1.32	0.58

It was decided to use kevlar rope as tendons for the model, due to its high tensile stiffness. The kevlar rope is 2.5 mm in diameter, made of Dyneema fibers and has a breaking load of 569 kg. The stiffness of the tendons were determined from a simple setup in which the tendon was elongated by adding known masses in the range from 5 - 35 kg. The EA-value of the model tendons is computed to $8.11 \cdot 10^4$ N.

3.3.3 Wind turbine tower

Given the simple geometry of the tower it should be a straight forward task to construct a tower in model scale. However, apart from the dimensions and weight, a key parameter to match is the bending stiffness, since the bending stiffness is governing for the natural frequency of the tower. Matching the natural frequency for the tower is essential, since the structural frequencies of the tower can be excited by the 1P or 3P frequencies. Moreover extreme waves can excite a response of the tower, a phenomena known as ringing.

Due to the floating support of the tower which is relatively soft, it is expected that the tower will only be excited at its first natural frequency in its most fundamental mode shape. For the original full scale tower the first natural frequency is 0.25 Hz which corresponds to 1.94 Hz in model scale. In october 2012 an experimental study of a 5 MW TLP model was conducted at DHI, . The properties of the wind turbine tower used in [24] is quite similar to the target values in this project, with respect to mass and height. This tower is not conical as the full scale tower, and it is also undersized in diameter, but this is considered of secondary importance, since the cross sectional geometry of the tower primarily has an impact on the aerodynamic drag on the tower. The height

INNWIND.EU D4.2.4: Floating Wind Model Tests at ECN and DHI

of the model tower is 1.61 m, which is only a deviation of 1 % from the target value of the present design, but as it will be outlined later the distance to the nacelle will be increased by an additional 72 mm, due to the installation of a strain gauge for monitoring of thrust.

Pure tower decay tests were carried out leading and from these tests the first natural frequencies in the x- and y-direction were extracted: $f_{tower,x} = 2.0$Hz and $f_{tower,y} = 2.4$Hz.

Given that the natural frequency in the x-direction is only differentiating by 3 % from the target natural frequency of 1.94 Hz, it was decided to move forward with the tower from DHI. An advantage of this tower is that the tower frequency will certainly not be excited by the 3P frequency. In Figure 67 the 1P and 3P spans are plotted along with the wave energy spectrum for all the environmental conditions introduced in section 3.9.
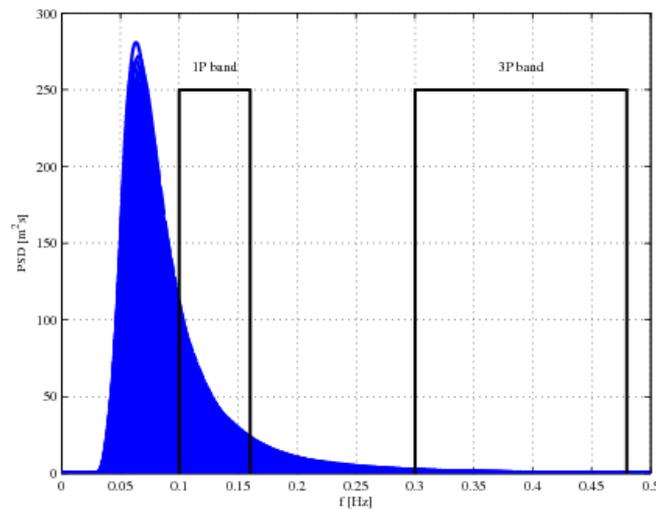
Figure 67 - Wave energy spectra and the 1P and 3P frequency spans

Figure 67 demonstrates that the model tower with a frequency of 2.0 Hz in the x-direction (0.268Hz in full scale) does not coincide with any critical excitation frequencies. Moreover a rough estimate of the coupled natural frequency of the tower bending mode and the pitch motion as being roughly 10-20 % below the tower natural frequency, based on the results from a FEM model, shows that the coupled natural frequency of the tower and the pitch motion should not conflict with the peak frequency of the sea states or the 1P frequency.

3.4 Design of a low-Reynolds number rotor

Froude number similitude entails a reduction in velocity in model scale as the model dimensions are smaller than the dimensions of the prototype. Hence the lab Reynolds number will be significantly lower than the full scale Reynolds number. Consequently the flow regime around the turbine blade will be poorly replicated in model scale if the blades are geometrically scaled. Since the lift and drag coefficient (C_L, C_D) for an airfoil are highly dependent on the flow conditions around the airfoil, [27], the wind turbine performance of the model is expected to deviate from the full scale rotor. The lift and drag coefficients are essential components of the lift and drag force as stated below:

$$F_L = \frac{1}{2}cC_L\rho_a V^2 \qquad F_D = \frac{1}{2}cC_D\rho_a V^2$$

(10)

INNWIND.EU D4.2.4: Floating Wind Model Tests at ECN and DHI

where c is the blade chord length, ρ is the density of the air and V is the relative velocity seen by the airfoil section.

The thrust force F_T and the force component contributing to the rotor torque F_Q are dependent on the lift and drag force in the following way:

$$F_T = F_L \cos\phi + F_D \sin\phi \qquad F_Q = F_L \sin\phi - F_D \cos\phi$$

(11)

where ϕ is the angle between the rotor plane and the incoming wind passing the blade, as sketched in Figure 68. Since ϕ usually is relatively small in magnitude for a high TSR-rotor (TSR: Tip Speed Ratio) as the one considered here, the lift force is the main contributor to the thrust force.
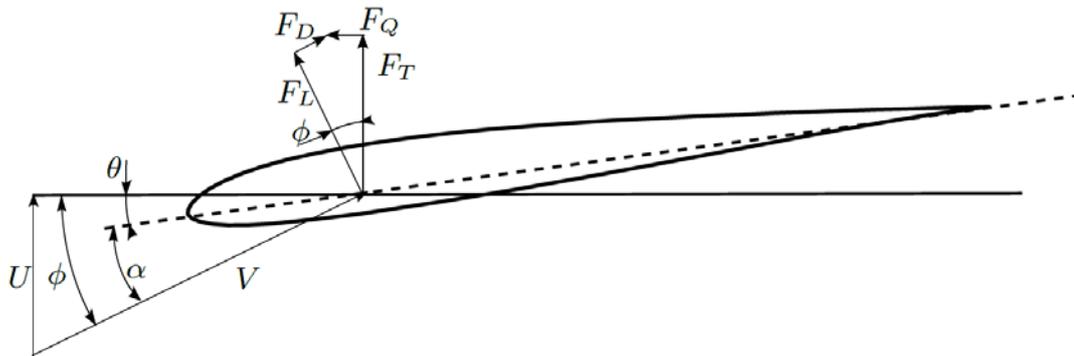
Figure 68 - Sketch of a 2D airfoil

One way to come around the changed drag and lift coefficients is is to implement an alternative airfoil profile which is more suitable for low Reynolds number flows, combined with an increase of the chord, such that the dominating scaling parameter for the blade is $C_L c$ instead of c. The drawback of shifting to a low Reynolds number airfoil is an increase in drag which preclude the ability to scale the torque and hence the power. According to [28] the thrust force is typically an order of magnitude greater than the overturning moment due to the rotor torque, and hence the thrust force will have a much greater impact on the global dynamics of the model. Therefore it was decided to aim for a thrust-matched rotor design. Moreover, effort was put into matching the tip speed ratio correctly and scaling the mass of the blades.

In [29] the overall design criteria for the thrust matched blades are listed, which are

• Match axial blade loading F_z and thrust coefficient C_T

• Single point design, $V = 10$ m/s for full scale

• Preserve design TSR
• Power as good as possible
• Preserve chord distribution scaled with the same factor for all radii

Maintaining the TSR in the Froude scaled wind field ensures that any excitation frequencies arising from rotor imbalances (1P) or aerodynamic interaction with the tower (3P) are scaled correctly.

Usually 1P is not present in numeric codes but will be present in experiments due to uneven mass distribution, discrepancies in pitch angle etc.

Furthermore a retained TSR and a scaled distribution of mass in the blades is a necessity for modeling the gyroscopic effects correctly.

INNWIND.EU D4.2.4: Floating Wind Model Tests at ECN and DHI

As stated in [29], the need for an alternative low Reynolds number airfoil to form the basis for the thrust matched turbine lead to a manual search for profiles with the aerodynamic properties:

- Linear behavior in attached flow across the Reynolds number range
- Continuous trends for drag
- High lift-drag ratio
- "soft"☐ stall behavior
- Limited or no hysteresis

The SD70xx series, [30], [31] [32] was chosen for further analysis due to its favorable properties at low Reynolds numbers. The airfoils in this series are much slimmer compared to the high Reynolds number airfoils of the 10 MW DTU reference wind turbine.

Airfoil data down to $Re = 60000$ was available, but since initial computation suggested that the Reynolds number would be as low as $Re = 25000$ in model scale, it was decided to conduct measurements of a SD7003 airfoil at DTU. A 2D blade was tested in the "red open loop low speed wind tunnel" at DTU for Reynolds numbers of $15000, 20000, 30000, .., 70000$. Measurements were carried out at the minimum turbulence intensity of around 0.1 % and with added turbulence generated from three thin wires mounted upstream of the testsection. With the wires the level of turbulence intensity can be increased up to 1 %. It should be noted that this increased turbulence intensity is still much smaller than the turbulence intensity experienced by the blades in the wave tank tests which was typically 5%.

In Figure 69 the lift and drag coefficients are plotted as a function of the AOA. The results are discussed in detail in [16]. The coefficients for $Re = 15000$ and $Re = 20000$ are omitted since these results turned out to be of insignificant relevance.

INNWIND.EU D4.2.4: Floating Wind Model Tests at ECN and DHI

C_L and C_D depency on AOA number(——) C_L, (- - -): C_D

Correlation between C_L and C_D

Correlation between C_L/C_D and C_D
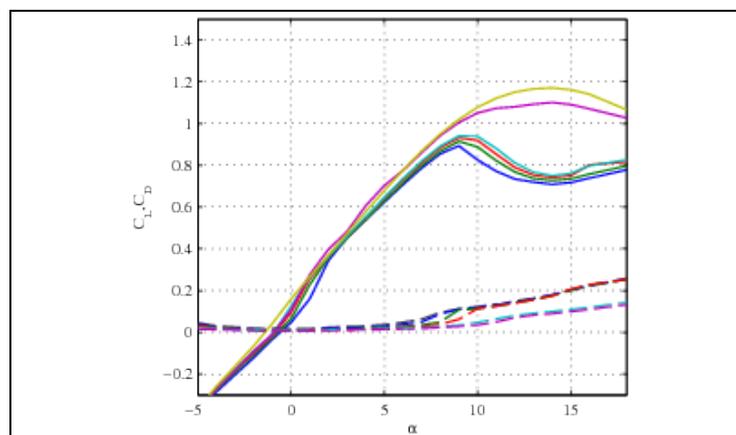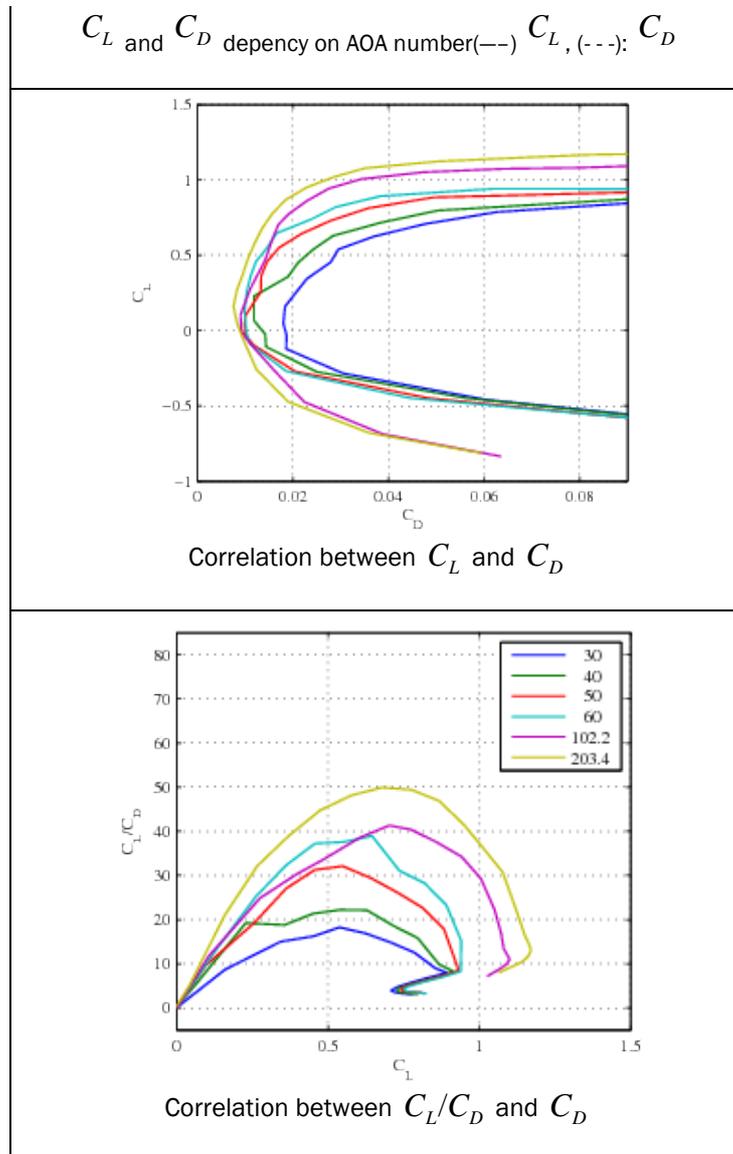
Figure 69 - Measured airfoil characteristics of the SD7003 airfoil for Reynolds numbers of 30k, 40k, 50k and 60k. Selig data applied for 100k and 200k.

The measured airfoil properties is the main input for the final rotor design. A central task here was to decide upon the length of the chord which must match with the design C_L in order to scale $c \cdot C_L$ correctly. Additionally the chord is a decisive parameter with respect to the Reynolds number and in order to ascertain a sufficiently high margin to stall, the chord must be increased around 60-80% to match the design lift.

However, increasing the chord implies the need for more material and hence an increased weight of the blade. Furthermore, an increase in chord would make the blade more sensitive to changes in the pitch of the blade, impacting the global dynamic response of the model.

INNWIND.EU D4.2.4: Floating Wind Model Tests at ECN and DHI

Even though the slope $\dfrac{\delta C_L}{\delta \alpha}$ is alike for the full scale blade and model blade the relative larger chord of the model blade will result in greater changes in the load and increase in aerodynamic damping for the model blade for an equivalent change in the AOA. This sensitivity towards pitch is naturally an issue impacting the control characteristics of the model, but since the main target is to match the static thrust force, this effect was condoned.

As stated earlier, the new blade design does not allow a match of the torque, due to the larger drag of the SD7003 airfoil compared to the prototype blade, and hence the maximum C_L/C_D ratio of the model blade will consistently be lower. According to [27], typical values of the C_L/C_D ratio is in the order 100-150 for full-scale wind turbine blades, while figure 6 shows that only a maximum C_L/C_D ratio of 20-40 is obtainable.

A series of trial computations was conducted to investigate the impact on the Reynolds number and the lift coefficient for different chord elongations. This lead to the choice of a chord increase of 75 % relative to direct geometric scaling. The final blade design is shown in Figure 70.

Scaled chord distributions. The inboard adjustment serves to have a cylindrical section of 80mm

INNWIND.EU D4.2.4: Floating Wind Model Tests at ECN and DHI

Distribution of Reynolds number across the blade span

Distribution of lift and drag coefficients
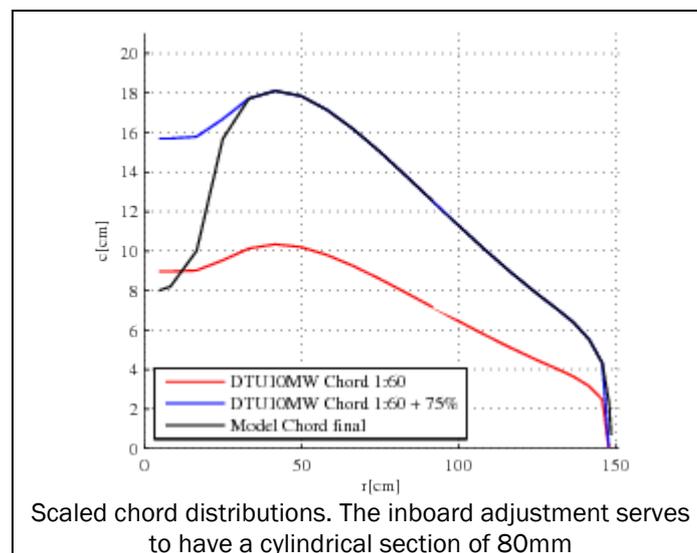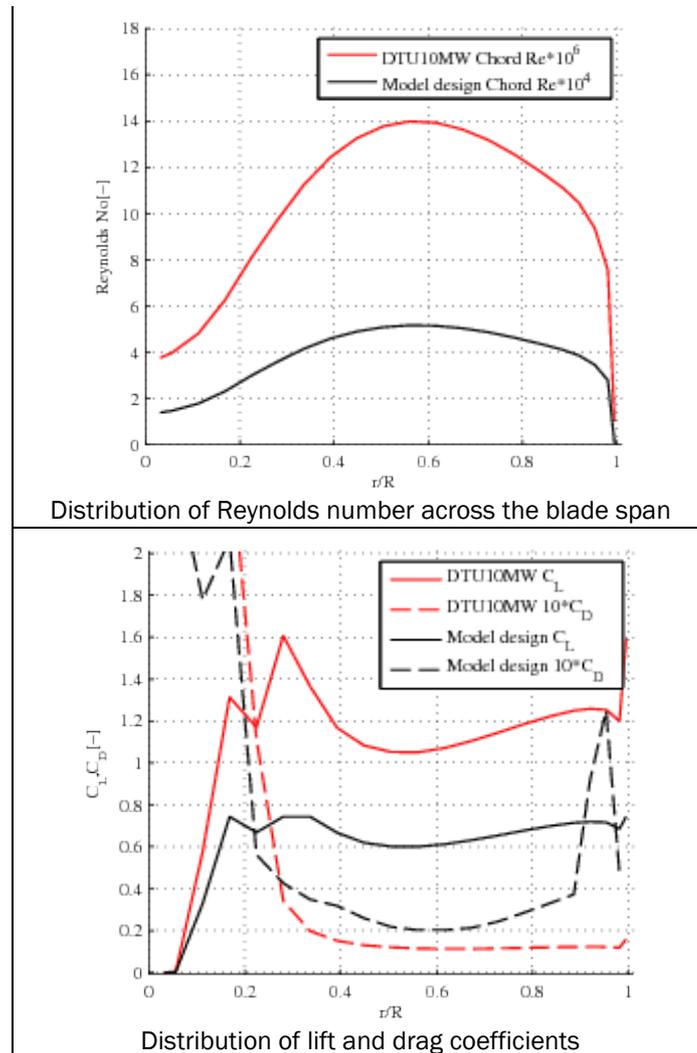
Figure 70 – Properties of the performance scaled blade.

Two additional airfoils from the SD70xx series, more specifically SD7032 and SD7062, were applied to assist in the transition from the SD7003 profile to a cylindrical profile at the blade root. Additional information can be found in [29]. All three airfoils are sketched in Figure 71. Determination of the twist angle of the model blade is thoroughly outlined in [29], but a main point is that knowing the chord, thickness and lift distribution, the twist may be derived using the airfoil data and linear interpolation.

INNWIND.EU D4.2.4: Floating Wind Model Tests at ECN and DHI
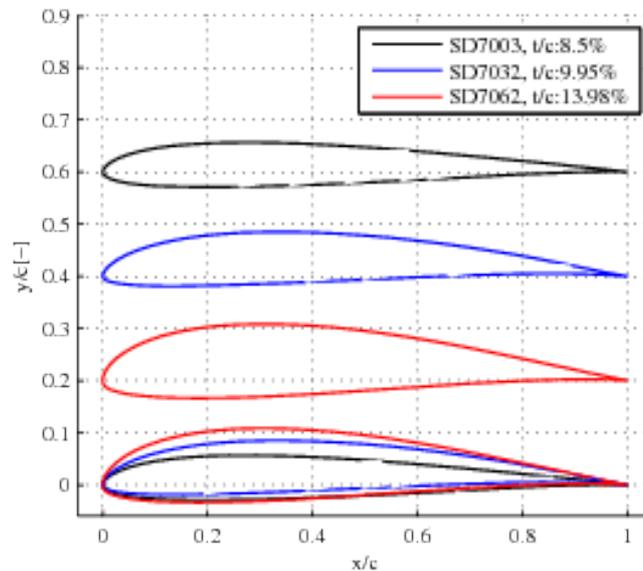
Figure 71 - 2D SD70xx airfoils making up the performance scaled blade

3.4.1 Casting and assembly of blades

It was decided to aim for a lightweight design with one layer of weaved carbon fiber ($\rho = 80\text{g/m}^2$) aligned with the span of the blade, followed by a unidirectional carbon fiber band ($w = 25$ mm, $\rho = 295\text{g/m}^2$) also aligned with the span of the blade to increase the spanwise stiffness.The next layer of carbon fiber with a finer weaving is oriented at an $45°$ angle with respect to the span. The weaved carbon fibers have a density of approximately 93 g/m^2 .

Slow curing epoxy resin was used as adhesive and hardener. The amount of epoxy resin should match the mass of the carbon fiber.

A vacuum was created in the mold and after 24 hours of hardening the two sections of the blade were taken out of the mold. Any excess material was cut away and the suction and pressure sides were then ready for assembly. A blade partition was cut from a plate of foam which in advance had been reinforced with a layer of carbon fiber on each side. The blade partition was inserted at 30 % of the chord from the leading edge.

A difference in the range of 10 g between the blades was detected once the blades were assembled. In order to balance the mass and the center of mass for the individual blades, a piece of brass band aligned with the airflow was attached to the pressure side of two of the blades in order to minimize the disturbance of the flow, such that they would match the heavier blade in mass and center of mass.

As stated earlier, the airfoil profile is thicker at the inboard part, and combined with a lower Reynolds number the risk of flow separation is higher in this region of the blade. Therefore it was decided to attach vortex generators to the inboard part of the blade to delay flow separation and thus aerodynamic stall.

One of the finished blades is shown in Figure 72.

(a) Top view

(b) Leading edge view

(c) Bottom view

(d) Close up view of vortex generators
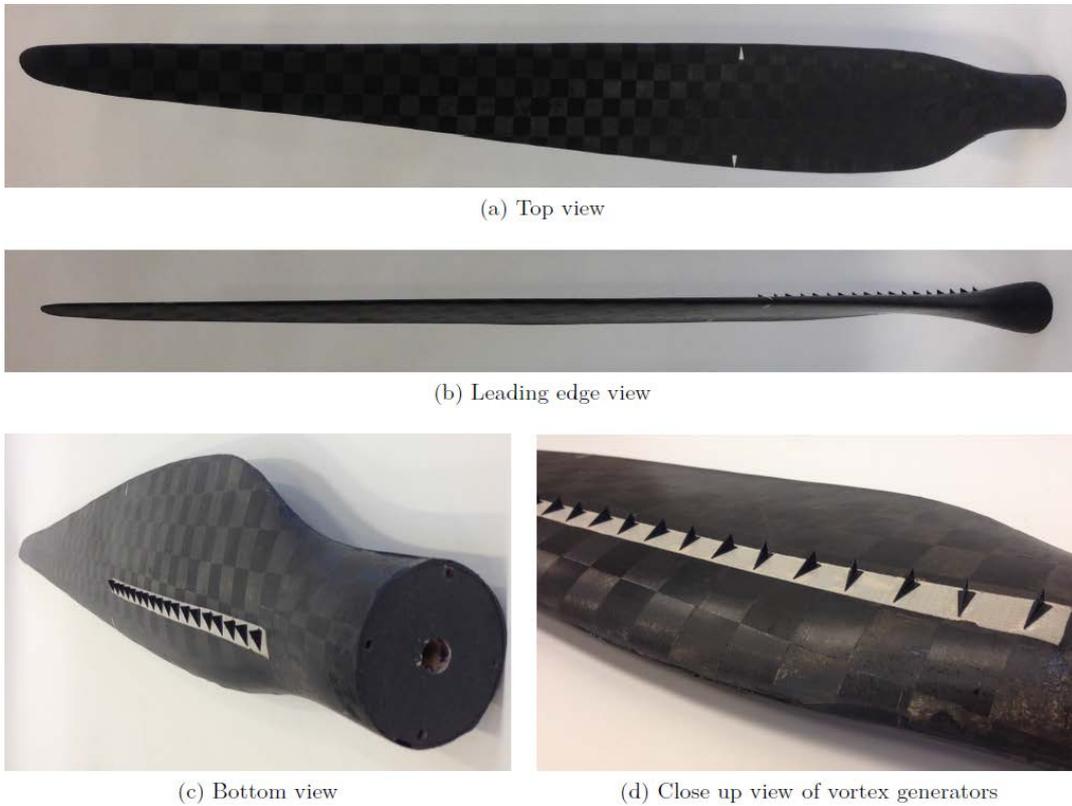
Figure 72 - Assembled blade

3.5   Model specifications

The assembled TLP wind turbine is shown in Figure 73.

Figure 73 – Assembled TLP wind turbine.

In Table 37Table 37 - Key specifications of the prototype scale wind turbine, the ideally Froude scaled 1/60 model, and the actual scaled 1:60 model the corresponding key specifications for the prototype wind turbine, the ideally Froude scaled model and the actual model TLP wind turbine are collected.

INNWIND.EU D4.2.4: Floating Wind Model Tests at ECN and DHI

Table 37 - Key specifications of the prototype scale wind turbine, the ideally Froude scaled 1/60 model, and the actual scaled 1:60 model

Dimension	Proto-type scale	Froude Model Scale	Actual Model Scale (including instrumentation)
Foundation			
Floater diameter D_f	18.0m	300mm	300mm
TP diameter D_{TP}	9.0m	150mm	150mm
Floater height h_f	25.0m	417mm	417mm
TP height h_{TP}	32.0m	533mm	533mm
Spoke length L_s	32.1m	535mm	535mm
Submergence h_s	12.0m	200mm	200mm
Freeboard $h_{freeboard}$	20.0m	333mm	333mm
Mass (3 spokes) M_f	2390ton	10.80kg	11.50kg
Mass (4 spokes) M_f	2403ton	10.85kg	12.49kg
Tendons			
Length l_t	142m	2.36m	2.25m
Stiffness EA_t			8 10⁴N
Tower			
Diameter, D_t	7.82m-5.50m	130mm-92mm	80mm
Tower height, h_t	95.6m	1594mm	1682mm
Hub height o. MWL, h_{hub}	119m	1983mm	2070mm
Mass, M_t	469 ton	2.12kg	1.98kg
Nacelle			
Rotor diameter, D_R	178.3m	2972mm	2972mm
Blade Length L_b	86.5m	1440mm	1440mm
Blade mass M_b	41.7 ton	0.188 kg	0.198 kg
Nacelle+hub mass M_n	552 ton	2.49 kg	3.48 kg
Full model			
Mass (3 spokes), M_{total}	3533 ton	15.96 kg	17.55kg
Mass (4 spokes), M_{total}	3546ton	16.02kg	18.54 kg
Vertical COG (3 spokes), z_{COG}	18.2m	310mm	378mm
Vertical COG (4 spokes), z_{COG}	18.4m	306mm	321mm
Mass moment of inertia (3 spokes) I_{yy}	1.30 10¹⁰ kgm^2	16.3kgm^2	22.30kgm^2
Mass moment of inertia (4 spokes) I_{yy}	1.30 10¹⁰ kgm^2	16.3kgm^2	22.70kgm^2

INNWIND.EU D4.2.4: Floating Wind Model Tests at ECN and DHI

By inspection of Table 37 the difference in mass of the nacelle and hub for the Froude model scale and the actual model scale really stands out, with an exceedance in the actual mass of 40%. Moreover the mass of the floater is too large for the actual model scale, especially for the configuration with 4 spokes. However as outlined in section 86 the z-gauges for monitoring of the tendon tension each weigh 250 g, and consequently are decisive for the excess mass.

This increase in the mass of the entire model, naturally leads to a decrease in the natural frequencies in all modes of motion. Especially the drastic increase in mass of the nacelle, results in an increase in the mass moment of inertia which most likely will lead to a considerable decrease in the pitch and roll natural frequencies. Moreover the increased mass of the nacelle and hub is expected to induce a destabilizing effect in the response as the model rolls and pitches. Yet, the fine compliance for the manufactured model blades must be highlighted. Given the complex shape, large dimension and low target mass, it is quite satisfactory to be within 5% of the target mass and obtain the degree of stiffness present in the blades.

Despite the differences in Froude model scale and the actual model scale, the model is still expected to represent the dynamics of the full scale FWT qualitatively. Even if this is not the case, the results are still valuable for validation of the numerical models by the model scale data. The validated model can next be applied for the design and analaysis of the full-scale structure.

3.6   Wave basin and wave generation

The experiments were conducted in the deep water wave basin at DHI Water & Environment in Hørsholm, Denmark. The length of the basin is 20m, the width is 30m and the depth is 3m throughout the entire basin, with the possibility of increasing the depth at the center of the basin to 6 or even 12m.

The wave maker is of the hinged type and consists of 60 individually controlled flaps, all operated by hydraulic pistons. The wave maker is capable of generating unidirectional regular and irregular waves with a heading of up to $\Theta = 30°$. Furthermore the wave maker is able to generate multidirectional waves. Opposite of the wave maker a passive wave absorber is located, with the aim of dissipating wave energy and reduce wave reflection. At the sides of the wave basin small stripes of permeable mat functions as wave absorbers to reduce the reflection from oblique waves.

A bridge, with the ability to move in the transverse direction of the basin, serves as the work station from where the wave makers are controlled. Additionally all the equipment for data acquisition is located on the bridge. In Figure 74 a top view of the wave basin is sketched.

INNWIND.EU D4.2.4: Floating Wind Model Tests at ECN and DHI
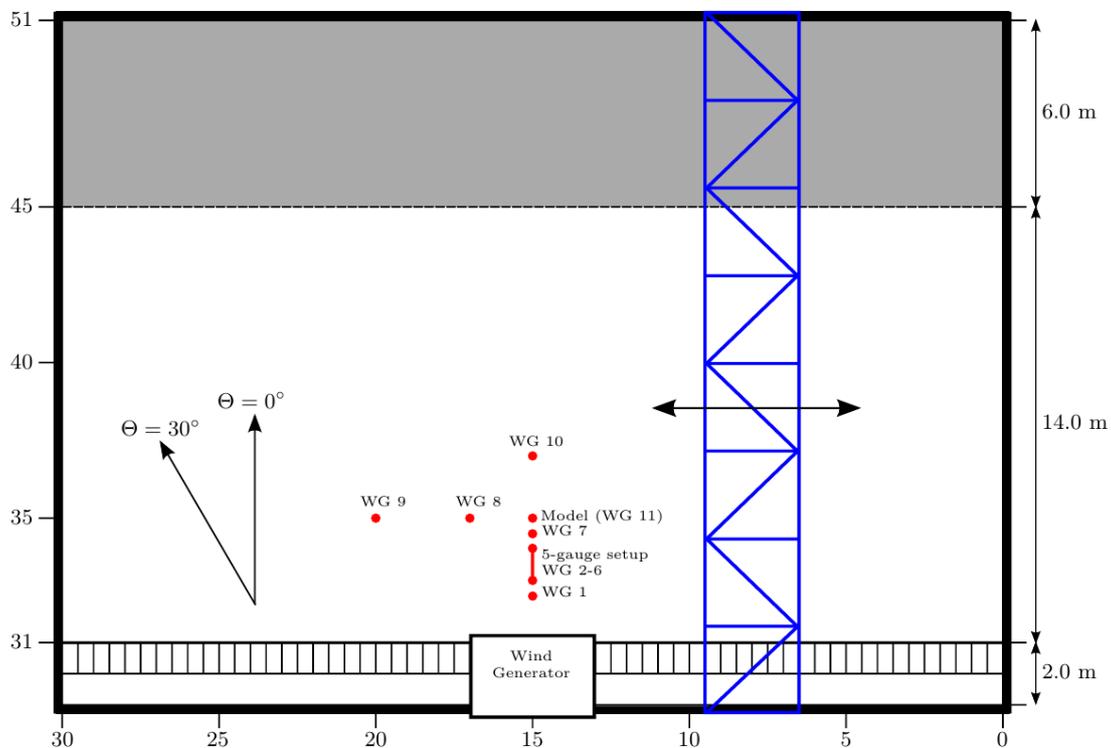
Figure 74 - Experimental setup in wave basin at DHI

Four meters from the wave maker the mooring platform is immersed. The platform is build of wooden beams and weighed down with bricks of lead. Numerous eyebolts are pinned to the platform constituting the anchoring points for the three different mooring configurations. The tendons are lead through the anchor points, then trough eyebolts located at one common edge of the platform and then gathered on the bridge where the tendons are fastened. The individual tendons are coiled around their respective anchor point in an attempt to constrain the tendons to be elastic only from the model to the platform, while still being adjustable from the bridge.

The wind generator is located on top of the wave maker. It was necessary to construct a supporting structure of wooden beams in between the wave maker pistons, such that the wind generator can have a stable platform. In Figure 75 the experimental setup is sketched in side view.

INNWIND.EU D4.2.4: Floating Wind Model Tests at ECN and DHI
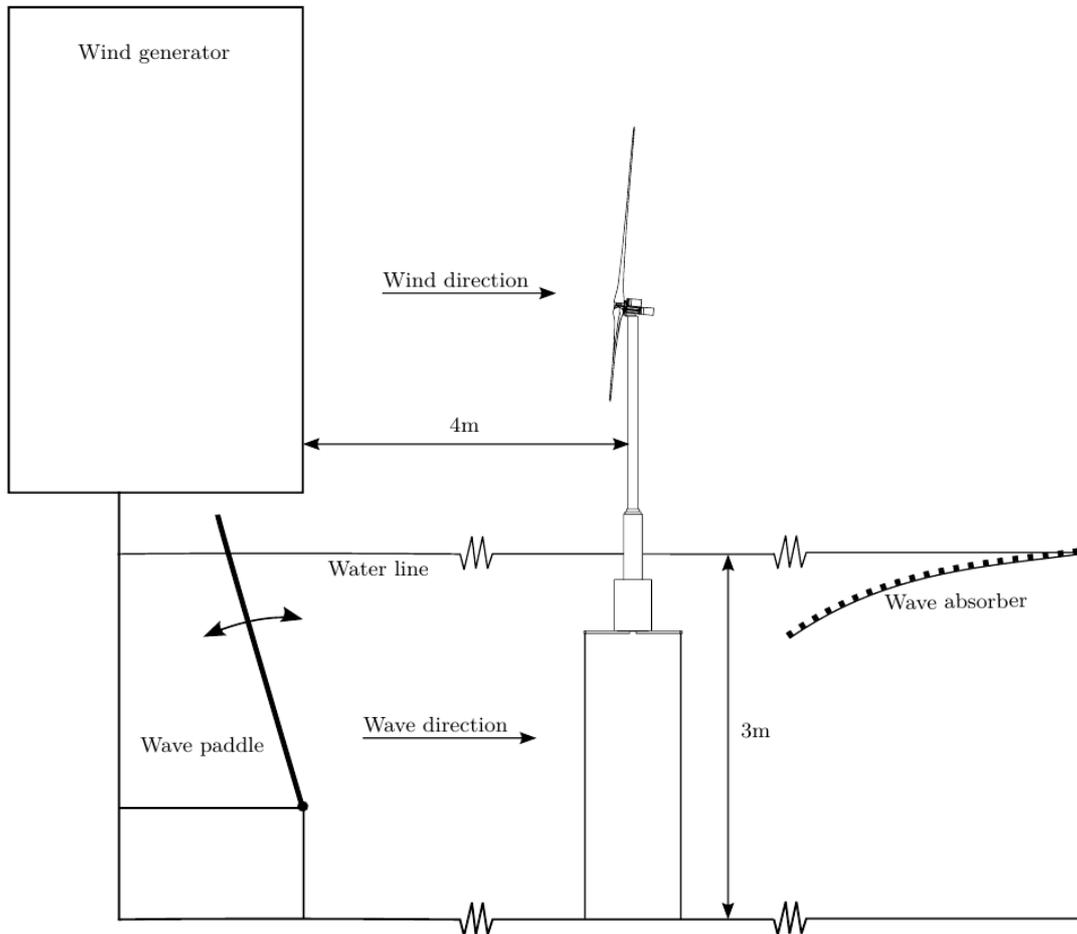
Figure 75 - Side view of the experimental setup

Due to the concrete borders of the wave basin and the wave paddles it was not possible to lower the wind generator sufficiently in order to cover the entire rotor area. One solution would be to tilt the wind generator forward, but due to the size of the wind generator this was not an option. Consequently this misaligned is tolerated in the experiments. A photo of the complete setup is shown in Figure 76.

INNWIND.EU D4.2.4: Floating Wind Model Tests at ECN and DHI
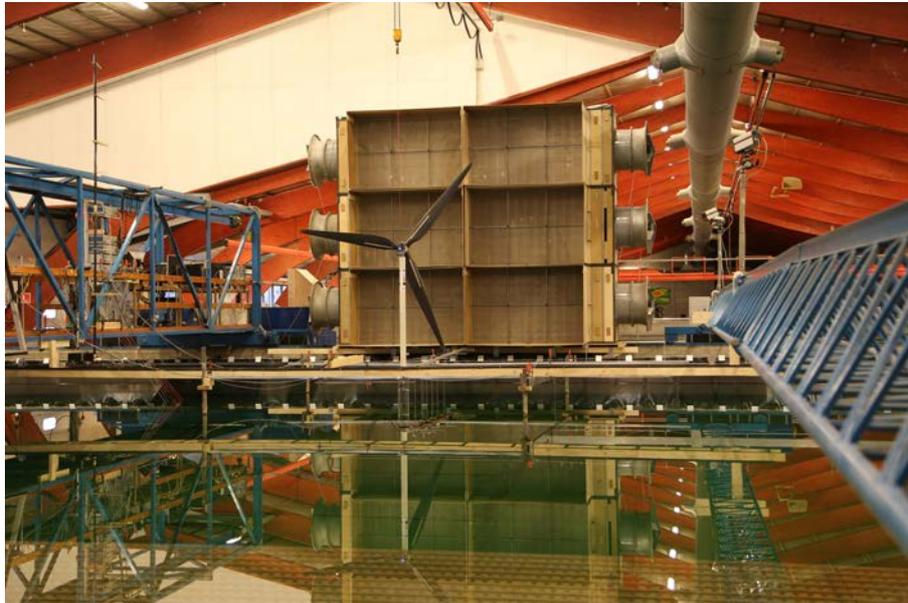
Figure 76 - Experimental setup

3.7   Wind generator design

The wave basin at DHI is not equipped with a wind generation system capable of covering the rotor area of the floating turbine. Hence it was necessary to design and build a wind generator from scratch. Given that the wind turbine is tested in a wave basin it is necessary to construct an open wind generator, yet an open jet allows the outer streamlines to bend more freely around the rotor plane, which actually simulates a real wind field better.

DHI were in possession of six AVL-710 fans, which formed the basis for the design of the wind generation system. It was decided to have an outlet of 4m x 4m, to cover the rotor area since the wind turbine is located some distance from the wind generator, and the area of the uniform wind profile decreases as the wind turbine gets further away from the outlet, causing a higher degree of turbulence at the boundaries, potentially impacting the wind turbine rotor.

Instead of designing one large wind generator, the generator system was designed as six identical units with outlets of 2.00 m x 1.33 m. Several benefits arose from this strategy. First of all it gave the opportunity of testing a single wind generator once it was built, making it possible to measure and decide upon whether the sought wind field was obtainable before the construction of the remaining units. Moreover the crane at DHI could not lift more than 1000 kg, and with a weight of 100 kg per fan this would put an impracticable limit on the weight of the remaining construction. A sketch of the single wind generator and the final wind generation system where six units are combined to form a uniform wind profile of 4 x 4 meter is provided in Figure 77.

INNWIND.EU D4.2.4: Floating Wind Model Tests at ECN and DHI
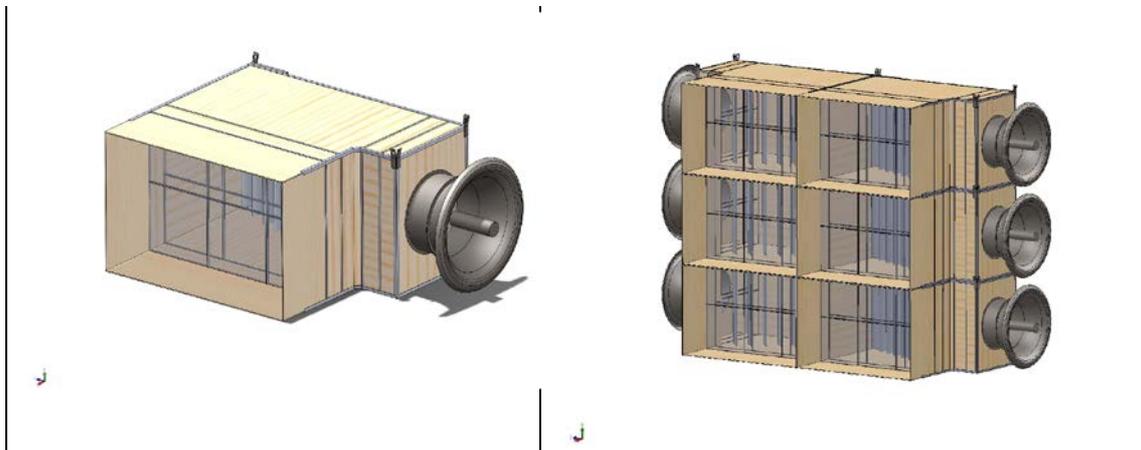
Figure 77 - Sketch of wind generator. Left: Single unit. Right: Full generator.

The limited space available for the wind generator at the wave basin set out the need for a compact solution which was achieved by introducing a corner section where the flow is turned $90°$. Additionally the corner section was utilized for expanding the flow, which otherwise would require a diffuser section. A compact diffuser given the space available would most likely lead to flow separation and backflow due to the relatively sudden expansion. Such phenomena causes energy loses and induces turbulence to the flow. Guide vanes were mounted diagonally in the corner section to turn the flow $90°$ without significant energy loses, and an additional benefit of the guide vanes is a reduction in large scale turbulence.

In order to homogenize the flow prior to the corner section a settling chamber with dimensions of 1.33 m x 1.00 m was installed. The settling chamber was fitted with two screens and downstream of the corner section two additional screens were installed. The axial fan induces a strong rotational velocity component to the flow, and the purpose of the screens is to filter out this turbulence and to smear out the flow. The flow must have a certain length to develop across once it has passed the screens. This is due to the small scaled turbulence introduced by the wires in the screen. Therefore the outlet is situated some distance away from the last screen. It was decided not to mount a contraction at the outlet of the wind generator, since this would require an outlet of the corner section of at least 5 x 5 meter, which would make the construction too large for the basin building. However the lack of a contraction section which in particular reduces turbulence at the boundaries will imply the need for careful considerations regarding the remaining sections of the wind generator.

An exploded view of the wind generator is presented in Figure 78. In-depth descriptions of the screens, guide vanes, fans and wind generator construction is provided in the report of Laugesen & Hansen [22].
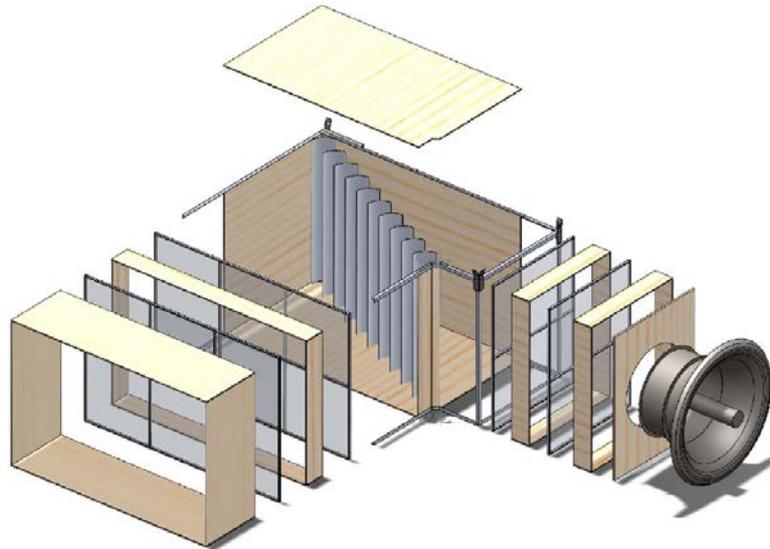
Figure 78 - Exploded view of a single wind generator

Before commencing the model tests, the wind field was measured in a few discrete points, as only a single air velocity probe was available. The wind speed was measured by means of TSI 8455 air velocity transducers borrowed from DHI and described in section 3.8.

Based on these measurements, the wind generator settings that were applied throughout the entire range of experiments, were defined. The measurements were conducted in a plane approximately 0.5 m downwind from the un-forced rotor position. It is assumed that the wind field does not develop significantly over this distance as it is small compared to the distance of 4.0 m from the rotor to the wind generator.

The 16 measurement points were evenly distributed across the wind generator, as sketched in Figure 79. A sampling time of 30s was chosen to be able to determine the turbulence intensity from the largest scales which are assumed to be the same order of magnitude as the wind generator. Given a minimum wind speed in the order of 1m/s, this sampling time corresponds to

the passing of $\dfrac{1\text{m/s} \cdot 30\text{s}}{4\text{m}} = 7.5$ of the largest eddy structures.
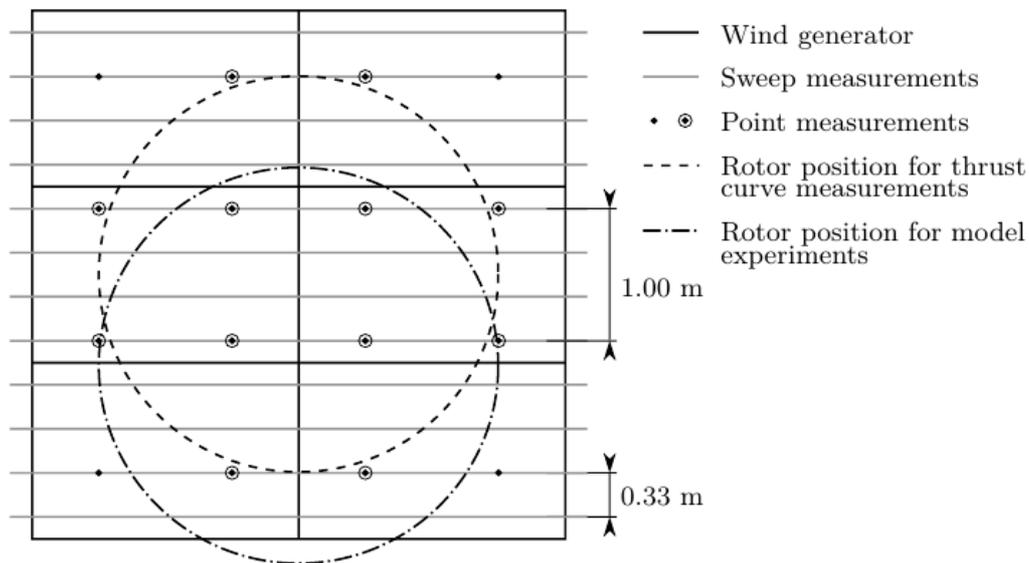
INNWIND.EU D4.2.4: Floating Wind Model Tests at ECN and DHI

Figure 79 - Location of wind point and sweep measurements and the wind turbine rotor relative to the wind generator

It was decided to base the overall mean wind speed and the overall turbulence intensity estimate on the mean of the measurements in the circled points in Figure 79, even though the rotor in the model experiments was not centred in jet. For the model experiments the rotor was centred approximately 2.0 m above the MWL, which corresponds to 1.35 m above the bottom of the wind generator. These are shown in Figure 80, in the legend denoted "point", for a range of fan frequencies from 24 Hz to 47 Hz, which turned out to be the maximum frequency that did not lead to overload on the fans. As it appears from this figure, the maximum obtainable mean wind speed was 1.7 m/s, meaning that environmental states 6-10 could not be established with the correctly scaled wind speeds. It was decided to apply the maximum wind speed at these environmental states as it is shown in Table 38.
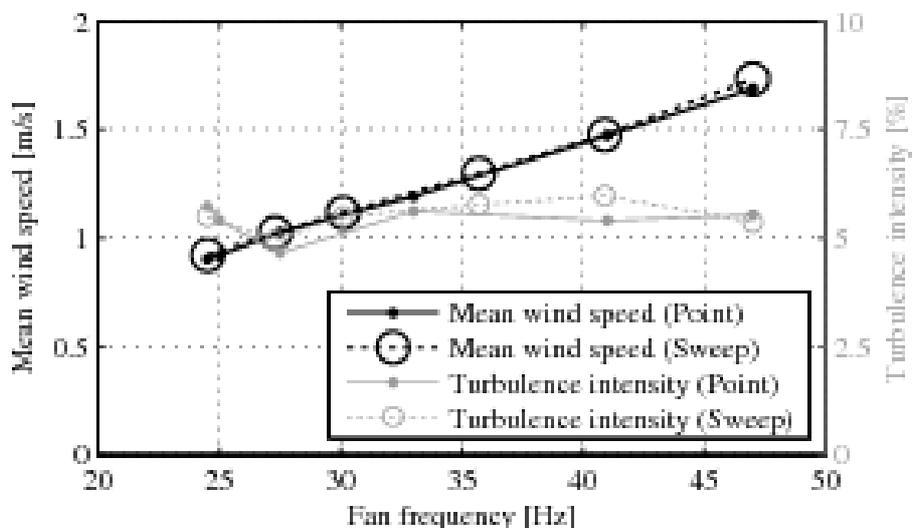
Figure 80 - Mean wind speed and turbulence intensity for a range of fan frequencies

INNWIND.EU D4.2.4: Floating Wind Model Tests at ECN and DHI

In Figure 80 it is further observed that the mean turbulence intensity is around 5%, for all wind speeds, and that the mean wind speed seems to depend linearly on the fan frequency. A linear correlation between fan frequency and mean wind speed was estimated:

$$\overline{U} \cong 0.035 f_{fan} + 0.058 \qquad (12)$$

where $\overline{U}$ [m/s] is the mean wind speed, and f_{fan} [Hz] is the fan frequency.This correlation was used to define the frequency converter settings that were applied for the ten environmental states for all the model experiments, and are given in Table 38.

Table 38 - Fan frequencies and mean wind speeds for the 10 environmental conditions

Environmental state	1	2	3	4	5	6 - 10
f_{fan} [Hz]	24	27	30	36	41	47
$\overline{U}$ [m/s] (Point)	0.90	1.0	1.1	1.3	1.5	1.7
$\overline{U}$ [m/s] (Sweep)	0.92	1.0	1.1	1.3	1.5	1.7

Later, three additional probes were bought, giving the possibility to conduct sweep-measurements across the wind field in 12 levels, as sketched by the grey horizontal lines in Figure 79 - Location of wind point and sweep measurements and the wind turbine rotor relative to the wind generator. In the first sweep, the probes were mounted in levels 1,4,7 and 10, in the second sweep in levels 2,5,8 and 11 and in the third sweep in the remaining levels.The results for a mean wind speed of 1.7 m/s are presented as contour plots in Figure 81.

In these plots the six units of the wind generator are indicated by gray lines, and position of the rotor is sketched by a dot-dashed circle. The mean wind speed and mean turbulence intensity over the rotor, $\overline{U}$ and $\overline{TU}$, can be determined as

$$\overline{U} = \frac{1}{A}\int_A U dS, \qquad \overline{TU} = \frac{1}{A}\int_A TU dS \qquad (13)$$

where A is the rotor area. As shown in Figure 79, the measurements do not cover the entire rotor area. It is is likely that the wind speed drops significantly and the turbulence intensity increases at the bottom of the rotor where measurements are missing. However, as the area outside the measurement area is only $\approx 6\%$ of the total rotor area, it was chosen to neglect this variation, and in stead it was assumed that $\overline{U}$ and $\overline{TU}$ based on the area of the rotor that is covered by measurements, are representative of the same quantities for the entire rotor. To evaluate $\overline{U}$ and $\overline{TU}$ numerically, $\overline{U}$ and $\overline{TU}$ were first interpolated to a finely meshed circular grid, covering the rotor area. Next, the surface integrals (6) were approximated using the trapezoidal rule. The values of $\overline{U}$ and $\overline{TU}$ are plotted in Figure 80 together with the corresponding quantities from the point measurements. It is evident that the two series of measurements show very equal results both for the mean wind speed and the turbulence intensity. Hence, the sweep measurements confirm that the applied settings of the fan frequency give mean wind speeds over the rotor, as specified in the environmental states, however, with the aforementioned upper limit of 1.7 m/s.

The contour plots in Figure 81 show that for the a large part of the rotor area, the wind field is relatively uniform and low turbulent. The mean turbulence intensity is in the order of 5-6%. The performance of the wind generator is generally very satisfactory, given the compact design. It is observed that the uniformity of the flow over the rotor would be enhanced if the center of the jet

was lowered to the rotor center. However, this was not possible due to the presence of the wave maker. Further, it is observed that the wind generator unit in the lower left corner, under-performs in the range $-2 < y < -1$. Here the wind speed is remarkably low and the turbulence intensity is high for all mean wind speeds.

There are likely two explanations to this behaviour: One, is presence of the measuring bridge as sketched in Figure 74, which could have affected and limited the inflow to the fan. The other is that the guide vanes of this unit could have been installed at a larger angle, directing the flow to the center of the jet in stead of making it uniform. In addition an area of remarkably higher wind speeds for all mean wind speeds is observed in the center left unit. These deviations from uniformity in the wind field are likely to cause 3p frequencies in the response of the WT model response, because for each of the blades passing the an area with deviation from the more uniform part of the flow, the rotor will be loaded differently. This is worth to keep in mind for later analysis of the results.

INNWIND.EU D4.2.4: Floating Wind Model Tests at ECN and DHI
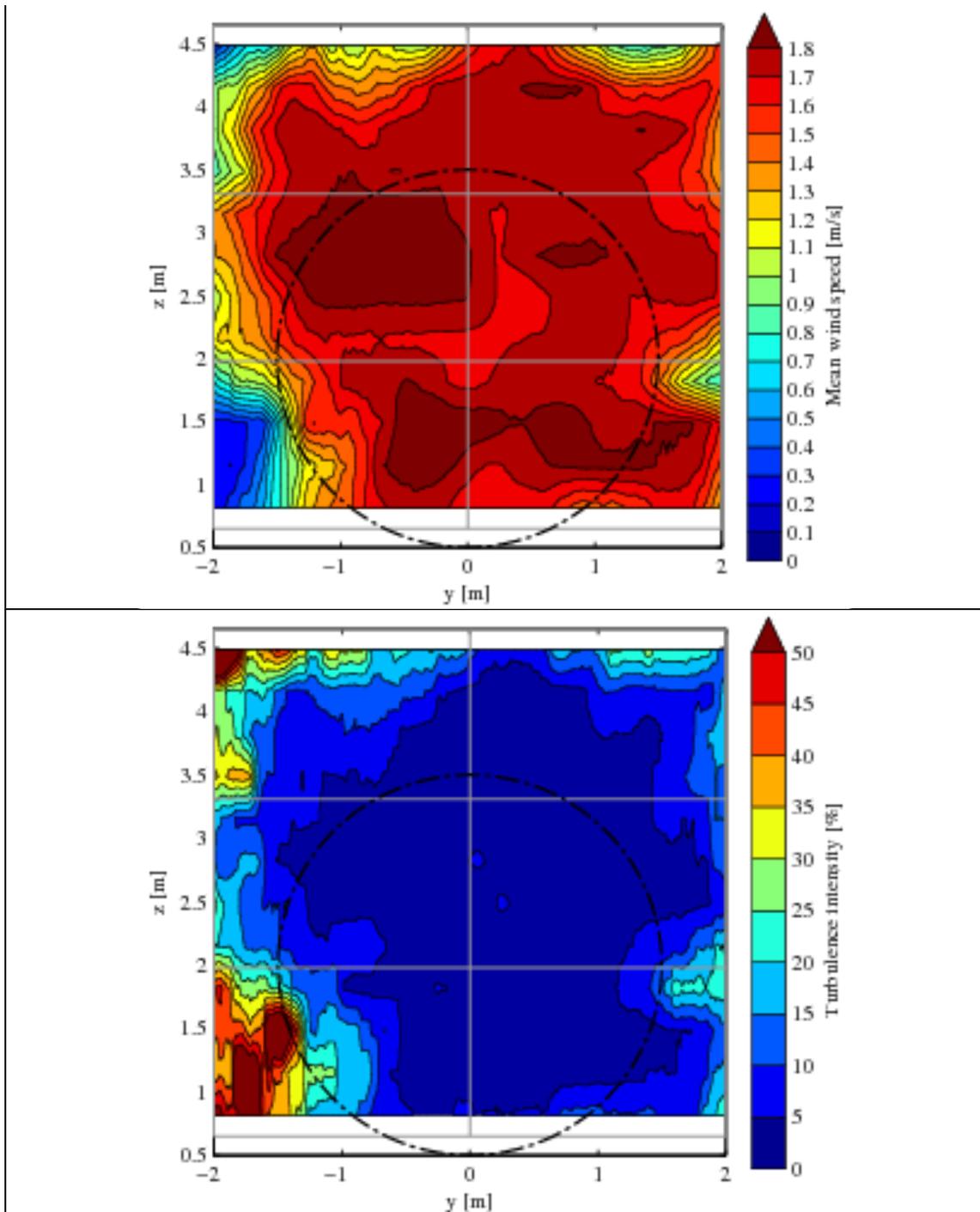
Figure 81 - Wind field measurements for a mean wind speed over the rotor area of 1.7 m/s. The wind generator units are sketched in grey, and the position in the model experiments is indicated by the dot-dashed circle. Upper: Mean wind speed. Lower: Turbulence intensity.

INNWIND.EU D4.2.4: Floating Wind Model Tests at ECN and DHI

3.8 Instrumentation and sensors

Apart from monitoring the surface elevation in 11 locations, it was decided to measure the six modes of motion, the accelerations in the floater and the nacelle, the tendon tension and the thrust force of the model.

3.8.1 Wave gauges

The eleven wave gauges used in the experimental setup (WG 1 - 11) are sketched in Figure 74.
A wave gauge is a simple monitoring device which consists of two thin rods of stainless steel in parallel. When submerged in water an electric circuit is established, and the voltage drop in the circuit is proportional to the level of submergence. The wave gauge is calibrated by submerging it to two known depths and a linear relationship between voltage and submergence/surface elevation can be extracted. The 5-gauge setup in front of the model facilitates an analysis of the wave reflection in the basin. However such an analysis is not conducted in this report.
Wave gauge number 11 (WG 11) is located at the exact position where the model is intended to be installed. Hence the surface elevation measurements from WG 11 will serve as reference for all subsequent experiments with the model. Five tripods were placed in the water and from aluminum beams connecting the tripods the wave gauges were hung. In this way the diffracted waves from the tripods did not impact the surface elevation measurements.

3.8.2 Z gauges

The tendon tension is captured by Z-gauges. This type of gauge is Z-shaped, made of stainless steel and when the Z-gauge is elongated a strain gauge monitors the deformation which through Hooks law is converted to tension force. Eyebolts at either ends of the Z-gauge renders the possibility of inserting the Z-gauge as a link in the mooring line. A disadvantage of the Z-gauges is the mass of 250g each, which indisputable will have an effect on the dynamics of the model.
According to [33] the accuracy of the Z-gauges is 1 % of the measured value and the resolution is 0.1 % of the force range.
The calibration of the Z-gauges was conducted by suspending the Z-gauges one at a time and gradually suspend a given number of weights with known masses. An upper limit of around 200N was chosen, which guaranteed a sufficient safety margin. In this way a linear relationship between loading and output voltage was obtained. It was tested that leaving the Z-gauges in the wave basin overnight did not change the readings.

3.8.3 Strain gauge

A two component strain gauge links the tower and the nacelle. The top and bottom of the strain gauge is connected by four pillars, and each pillar is fitted with two uniaxial film strain gauges. This setup enables measurements of the shear force between the nacelle and the tower, which can be interpreted as the thrust force on the rotor and transverse forces arising from unsteadiness in the rotor rotation.
In order to properly calibrate the nacelle strain gauge, the tower was aligned horizontally and calibrated by suspending known weights in the lateral and transverse direction, respectively, resulting in a linear description of the loading and output voltage.
During the experiments the thrust measurements had a tendency of being contaminated by an offset of around 0.2 N even though the strain gauge was reset before the tests. One very reasonable explanation for this is a heterogeneous cooling of the pillars and strain gauge due to the wind field. To reduce the possibility of this uneven cooling the strain gauge was encircled by a piece of paper.

3.8.4 Accelerometers

Five single axis accelerometers were used for monitoring accelerations sensed by the model. Three accelerometers are mounted perpendicular to each other in the floater at the top of the floater comprising a 3 axis system. Two accelerometers were attached underneath the nacelle measuring the acceleration in the x and y direction.

Measurements of the acceleration in the nacelle and floater in the x and y direction enables an estimation of the tower frequency. Moreover the accelerations of the floater is comparable to the Qualisys displacement output, since the transition piece is very stiff compared to the tower. The accelerometers weighs 29.1g each, and hence the mass of the nacelle is increased by around 2 %.

A static gravitational calibration was carried out in order to obtain a three point reading at 0 and $\pm 1g$. The relationship between acceleration and voltage is linear and the range was set to cover $\pm 2g$.

3.8.5 Qualisys motion tracking system

The Qualisys system extracts the surge, sway, heave, roll, pitch and yaw motion of the TLPWT. It consists of two infrared cameras that track the motion of the TLPWT and a piece of software that processes the camera readings. At the top of the transition piece an aluminum frame parallel to the water surface makes up a platform on which three white spheres were mounted at different heights. An additional sphere was fitted to the lower part of the tower, and these four spheres constitutes a frame of reference. The spheres cannot move independently and hence the motion of the spheres is directly linked to the motion of the model. A certain spacing between the spheres is necessary in order to separate the surge, sway, heave, roll, pitch and yaw motion of the model in the Qualisys system, and likewise the spheres must at all time be visible to both cameras. At the same time the spheres must be within sight of the camera and neither the spheres or the supporting structure must be in the way of the rotor. Moreover the size of the supporting structure should be minimized in size and weight in order to corrupt the motion of the model as little as possible. The chosen sphere-setup is a compromise of these conditions. The Qualisys software outputs the motion which is then sampled.

The calibration is carried out by fixing a right-angled frame to the top of the transition piece with the tower unmounted. The frame is aligned with the x and y direction and spheres are located along the edges, such that the origin, the x, y and z axis of the frame of reference can be established. Subsequently the four spheres and wind turbine are installed.

According to [33], the accuracy of the positioning system is generally within 1mm, which with the applied spacing of the tracking objects corresponds to an accuracy in the order of 0.1 deg for rotary motion.

Analysis of the results for platform pitch, however, have shown that the measured platform pitch is strongly exaggerated. Subject to ongoing investigations, it is expected that this exaggeration can be corrected by a change of the calibration. For this reason, however, the majority of the analysis in the present report is based on measurements of nacelle accelerations rather than platform pitch measurements.

3.8.6 Data Acquisition and sampling frequency

The output signals from the measuring instruments are collected through the analog gates of a DHI Standard Cabinet 101E. The input voltage must be in the range from $\pm$ 10 V. In order to maximize the resolution of the signal the gain of the incoming analog signal can be adjusted, such that expected minimum/maximum readings correspond to -10/10 V. Moreover the zero is manually set on the cabinet.

The cabinet outputs digital signals which are transferred to a nearby computer. A piece of DHI in-house software "Wave Synthesizer(c)" (WS) reads these digital signals and stores them in a mat.-file which is compatible with the data handling tool Matlab. The calibration of all instruments is

conducted in Wave Synthesizer. All instruments are consistently reset every time a series of tests is initiated.

A sampling frequency of 160 Hz was chosen in order to ensure a proper resolution of the input data. This is a relative high sampling frequency, since no important or physical frequencies are expected to occur above 31.0Hz which is the rotational speed of the servomotor at the maximum rotational speed of the rotor. However the frequency of the alternating current is 50 Hz, and it is recommendable to have this frequency resolved. The Nyquist criterion must be obeyed, which states the the sampling frequency must be twice the magnitude of the frequency present in the signal, in order to avoid aliasing. Furthermore the sampling frequency should not be divisible with the frequency of the alternating current. Hence a sampling frequency of 120 Hz is decent, but Wave Synthesizer did not allow this sampling rate, neither 130 Hz, and therefore the selected sampling frequency ended at 160 Hz.

3.8.7   Air Velocity Transducers

At DHI the hot spheres which were used during the construction phase of the wind generator were not available. Instead four TSI 8455 air velocity transducers (AVT), which are suitable for low speed measurements, were employed. An AVT consists of a rugged ceramic pin protected by a casing which only allows a 2D flow to pass the probe. The rest of the sensor is basically a thin metal cylinder intended to disturb the incoming flow as little as possible. A maximum velocity of not more than 2 m/s was expected, and consequently the lowest range of 0 m/s - 5 m/s were chosen. The accuracy of the AVT is $\pm$ 2% of the reading or $\pm$ 0.5% of full scale of selected range. In other words the accuracy is $\pm$ 0.025 m/s below 1.25 m/s and increases linearly from $\pm$ 0.025 m/s to $\pm$ 0.04 m/s in the interval from 1.25 m/s to 2 m/s. The AVT samples at a frequency of 5 Hz and the repeatability is within $\pm$ 1%. The AVT's did not need any calibration.

3.9   Test cases

For the experiments with the TLP floater, ten environmental conditions (EC) were chosen as a combination of H_s, T_p and wind speed at hub height $\overline{U}_{hub}$. These are given in Table 39 in full scale and model scale respectively.. For convenience, the environmental conditions are referred to as EC1, EC2,...,EC10. The peak wave periods for EC1, EC3, EC5, EC6 and EC7 were chosen equal to the peak periods of sea states 1,2,3,4 and 5 in the week 2 tests conducted at Ecole Centrale de Nantes. To increase the resolution under operational conditions, EC2 and EC4 were added with peak periods in-between those of neighbouring ECs. The associated wave heights for EC1-EC7 were determined by requiring a 5% wave steepness based on H_s and the deep water wave length, L_0, determined from the peak period. This yields to:

$$H_s = 0.05 L_0 = \frac{0.05g}{2\pi} T_p^2 \tag{14}$$

Equivalently, the wind speeds for EC1, EC3, EC5, EC6 and EC7 were chosen equal to the wind speeds for sea states 1,2,3,4 and 5 of the Nantes-tests and the wind speeds for EC2 and EC4 were chosen in-between. The EC10 was chosen as the 50-year sea state with the maximum significant wave height, based on the parameterised wind-wave climate of Johannesen [34], see also [18] and [16].The parameters defining EC8 and EC9 were chosen in-between the corresponding values for EC7 and EC10. The implementation of these environmental conditions is detailed in [16].

Table 39 - Environmental conditions described by significant wave height, peak period and hub height wind speed.

Environmental condition		EC1	EC2	EC3	EC4	EC5	EC6	EC7	EC8	EC9	EC10
H_s [m]	full scale	2.36	2.81	3.30	3.72	4.16	6.18	7.80	10.0	12.0	14.3
	model scale	0.039	0.047	0.055	0.062	0.069	0.103	0.130	0.167	0.200	0.239
T_p [s]	full scale	5.50	6.00	6.50	6.90	7.30	8.90	10.0	12.2	13.6	15.4
	model scale	0.71	0.78	0.84	0.89	0.94	1.15	1.29	1.58	1.76	1.99
$\overline{U}_{hub}$ [m/s]	full scale	7.0	7.8	8.5	10.0	11.4	18.0	25	33	40	48
	model scale	0.90	1.0	1.1	1.3	1.5	2.3	3.2	4.3	5.2	6.2

The test programme included the generation of regular waves, irregular sea states, focused waves and white noise sea states, as detailed in the following. These were all based on the environmental conditions (EC) defined in Table 39.

Regular waves are not representative of real sea states, but they are easy to analyse and valuable for system identification. For this reason, regular waves with wave heights and periods corresponding to the significant wave heights and peak periods of the ECs, respectively, were included in the test programme with a heading of both 0 degrees and 30 degrees to the global x-axis. The waves with a heading angle of 0 degrees were denoted R01, R02,..., R10, with wave heights and periods corresponding to EC1,EC2,...,EC10, while the waves with a heading angle of 30 degrees were denoted R11, R12,...,R20. All tests with regular waves were given a full scale duration of 30 min, corresponding to 4 min in model scale.

Irregular waves are the most representative of real sea conditions, but their analysis is also more involved. It was decided to include both long-crested irregular waves with heading angles of 0 and 30 degrees to the global x-axis as well as spread waves. The long-crested waves are simpler to analyse, and further this facilitates the comparison of two dimensional and three dimensional forcing. Irregular sea states were defined from Piearson-Moskowitz spectra with the significant wave heights and peak periods defined in the environmental conditions, Table 39. For the spread waves the spreading was described by the cosine-2s-power distribution with $s = 10$. It was found that the largest irregular sea states exceeded the limits on stroke and velocity of the wave paddle and could therefore not be generated. This was the case for the long-crested waves based on EC9 and EC10, and the spread waves based on EC10. It was decided to run 1 h realizations of all irregular sea states, and in addition to run 3 h realizations based on EC8 parameters, which represent harsh sea states that could be generated both with long-crested and spread waves, to get larger extreme waves. The 1 h realizations of the long-crested waves were denoted I01, I02,...,I08 and I11,I12,...,I18 for headings of 0 and 30 degrees to the x-axis respectively, with parameters corresponding to EC1,EC2,...,EC8. The 1 h realizations of the spread waves were denoted I21,I22,...,I29 corresponding to EC1,EC2,...,EC9. The 3 h realizations of EC8, were denoted I38, I48 and I58, for the long-crested 0 degree, 30-degree and spread waves respectively.

Focused waves were in the present work used to study the effect of a single large wave. It was attempted to produce focused waves of the New Year Wave type, at the position of the WT. Due to nonlinearity and perhaps also limitations in the wave generation system, the resulting time series at the location of the structure were not symmetric in time. Nevertheless, the achieved waves are still extreme waves and we note that asymmetry can well be expected for such large waves due to

INNWIND.EU D4.2.4: Floating Wind Model Tests at ECN and DHI

nonlinearity. The New Year Wave is created by waves with many frequency components which are generated by the wave paddle, such that they all meet at the WT, with a resulting excitation of the structure over a broad range of frequencies. The focused waves were created with wave heights corresponding to the expected maximum wave height a 3-hour realization. As for the long-crested irregular waves, it was not possible to generate focused waves based on EC9 and EC10 due to limitations on the wave paddles. The focused waves were generated in a long-crested form with both 0 degree heading and 30 degree heading, denoted F01,F02,…,F08, and F11,F12,…,F18, and with directional spread, denoted F21,F22,…,F28, with the expected maximum wave heights of sea states described by EC1,EC2,…,EC8, respectively.

White noise wave series were used to determine Response Amplitude Operators (RAO) for the structures. These waves were generated as a 1 h realization of an irregular long-crested sea state with a heading of 0 degrees, based on a rectangular spectrum. The low- and high cut frequencies were chosen as 0.5 Hz and 2.0 Hz respectively, and the spectrum area determined as to give H_s of EC2. Hence, the white noise wave was denoted W02.

3.9.1 Test sequence

First, the undisturbed wave field for all waves was measured without the structure in the water, and these tests were given as description the abbreviation for the tested wave, e.g. R01, I23, F14, W02, etc.
Next, the structures were mounted in the basin an subjected to the waves without wind, and these tests were identified by S1, S2 or S3 in addition to the wave abbreviation, e.g. S1R02, S2I13, S3F07 etc.
Finally, the three structures were tested in simultaneous wind and waves, which in the test identification was marked by adding a W after the letter in the wave abbreviation, e.g. S1IW04, S2FW02, S3RW18, S2WW02 etc. The wind speed was chosen in accordance with the wind speed of the EC from which the wave is derived. As documented in section 16, the maximum mean wind speed that could be generated in the experimental setup was 1.7m/s, meaning that the wind speeds of EC6-EC10 could not be modelled. It was decided to run these experiments at the maximum obtainable wind speed, and for EC6 and EC7 to operate the model WT as for this wind speed, while for EC8-EC10 to pitch out the blades since the desired wind speeds for these ECs exceed the cut-out wind speed.
It was managed to cover almost all tests for the three structures. A complete overview of the conducted tests is found in appendix D of the report [16]. Completed tests are assigned with a check mark in the first column of the test matrix, whereas unfinished tests are indicated by a red cell in the first column.

3.10 Selected results

In the following, selected results from the test campaign are presented. A more detailed and complete analysis of the results are provided in the report of Laugesen & Hansen [-1]. The present selection of the results give examples of the following phenomena:

- The effect of wave height on the response for irregular waves
- The effect of wind forcing and damping on the platform response and nacelle acceleration
- The difference in platform response and nacelle acceleration for 'structure 1' (vertical tendons) and 'structure 2' (inclined tendons)
- The effect of 3D wave spreading on nacelle accelerations
- The effect of wind-wave misaligment on the nacelle accelerations
- Platform response and nacelle accelerations for an extreme wave event

Most of the results are presented in terms of emprical exceedance probability plots. This type of plotting enables the presentation of a large amount of data in a concise and very applicable manner. The exceedance probability P is defined as

$$P = p(X \geq x_i) = 1 - \frac{i-1}{N} \qquad (15)$$

where x_i is the i'th peak response sorted in increasing order and N is the number of peaks in the time series. The exceedance probability is presented on a logarithmic scale, such that the extreme events in the response are magnified. To ensure that the peaks are not correlated, a downcrossing analysis on the free surface elevation signal was conducted to identify the time limits of each individual wave, see [16]. Next, for each independent wave the maximum displacement, acceleration and maximum and minimum tendon tension was determined and the exceedance probability for the entire time series was computed.

3.10.1 The effect of wave height on the response for irregular waves

First the wave height of every independent wave is presented in Figure 82 (left). Here it is seen that the smaller sea states (I01 - I05) are not that different when it comes to the distribution in wave heights, which agrees with the aim of having a better resolution of sea states near the rated wind speed. For sea states (I06 - I08), the wave heights increase significantly, reaching as high as 0.25m in seastate I08. This corresponds to 80 % of the maximum wave height in a three hour realisation and 56 % of the maximum wave in the 50 years design sea state. The legend in Figure 82 is valid for the plots throughout this section.

The right panel in Figure 82 shows the nacelle x-acceleration for the eight sea states. This direction is the inline wave-direction and the acceleration behaviour is seen to resemble the wave-crest behaviour (left) quite consistently. We note that the results here are for no wind forcing and thus associated with pure wave motion.
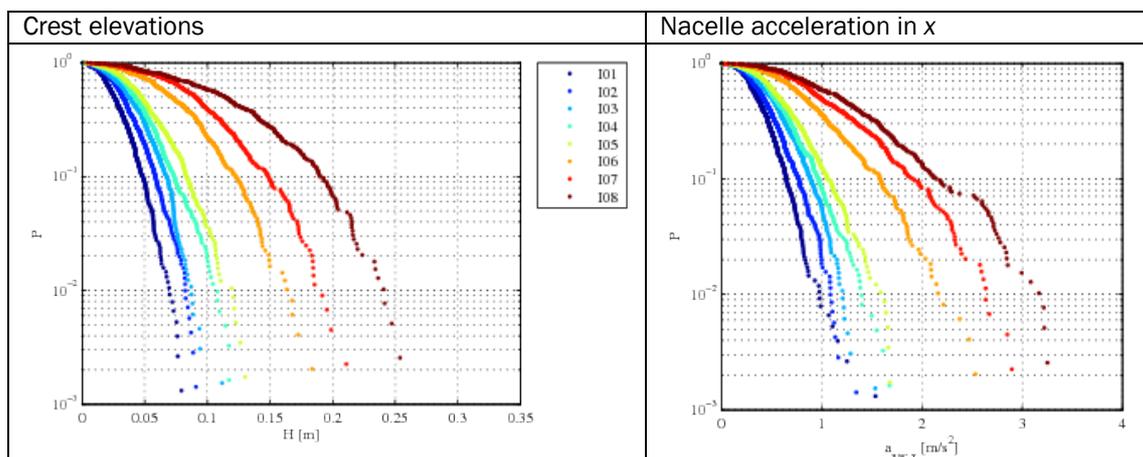
Figure 82 - : Left: Distribution of waves heights in the irregular sea states 1 - 8 for $\overline{\Theta} = 0°$. Right: Nacelle acceleration of structure 1 in irregular sea states 1 - 8 for $\overline{\Theta} = 0°$ without wind.

The nacelle x-acceleration gives a compact measure of the floaters influence on the turbine as it combines the platform surge and pitch induced motion of the nacelle and by the nature of acceleration provides an estimate of the motion-induced forces the nacelle and rotor are exposed to. A more complete picture of the motion response, though, is provided in Figure 83, that depicts all six components of the platform motion for structure 1 for the eight sea states.
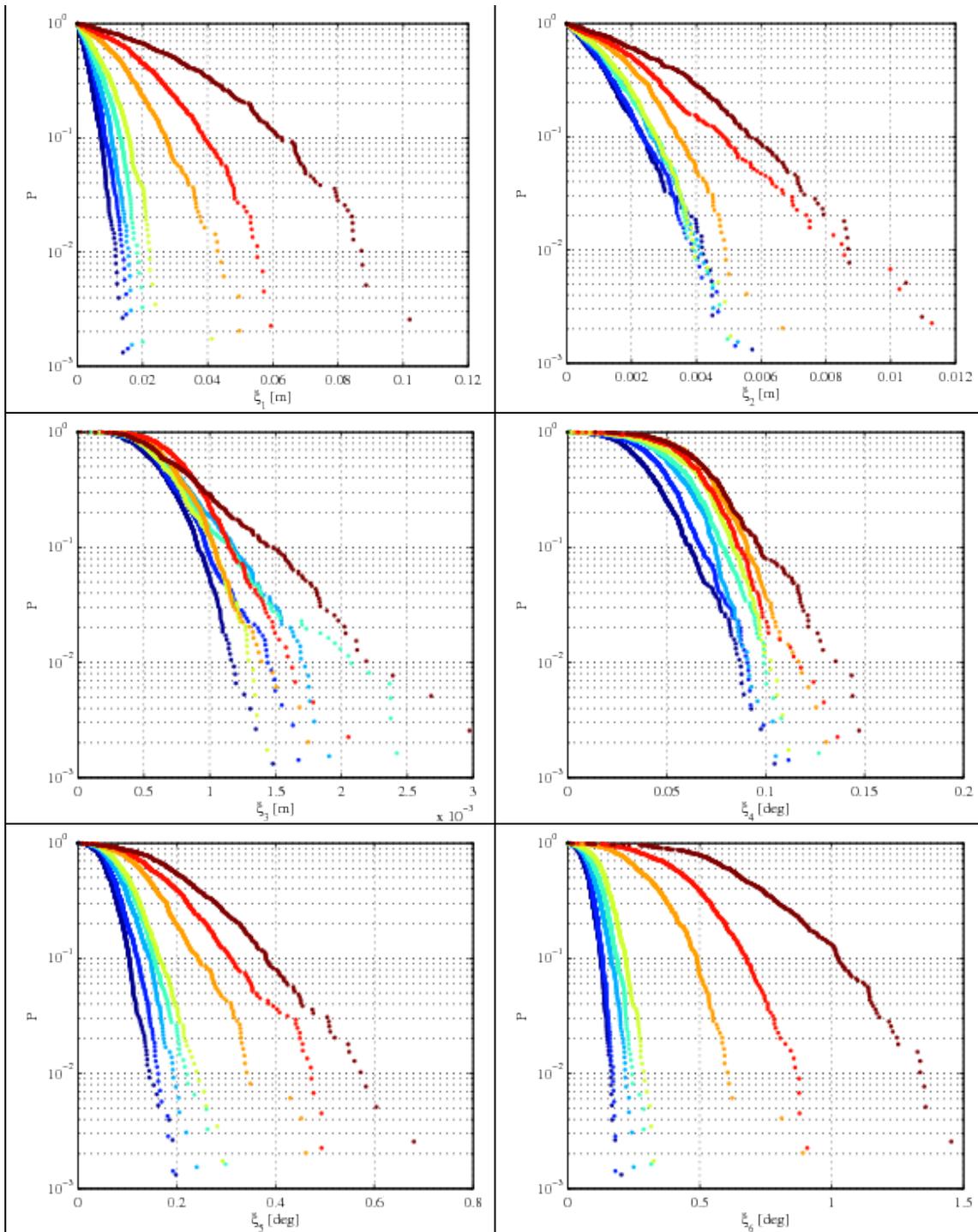
Figure 83 - Motion of structure 1 in the irregular sea states 1 - 8 for $\overline{\Theta} = 0°$ without wind

It can be seen that the magnitude of the surge motion is closely linked to the sea state, and it appears that the individual surge curves are roughly amplifications of sea state 1. The sway motion is an order below the surge motion and there is clear tendency towards larger sway motion as the sea state grows. The probability curves for sway, however, are not as organized as for the surge motion, especially for the smaller sea states. This behavior is expected since the sway

INNWIND.EU D4.2.4: Floating Wind Model Tests at ECN and DHI

motion for the long-crested waves with 0 heading angle is due to residual asymmetry in model, the mooring setup and/or the incoming waves.

For the heave motion, some increase in response is seen for increasing sea state number. For heave, however, it should be kept in mind that the response magnitude is of similar order than the measurement uncertainty of the Qualisys system. Hence the heave results can only be considered indicative. We notice, though, that the difference in heave for the smallest and largest sea state actually is quite limited, which is an essential feature of the TLP concept.

The rolling of the model is closely related to the sway motion, and generally it increases with growing sea state, but also in this case the rolling motion is caused by un-intended asymmetry.

The pitch motion has the same pattern as for surge and shows a clear correlation to the sea state strength. As explained in section 3.8.5, recent analysis have shown that the pitch values obtained from the Qualisys system are too large. Despite this finding which is subject to present further investigation, analysis of the relative change in pitch between different test conditions is still meaningful. In the remainder of the present report, though, emphasis is put on nacelle-acceleration, which provide a compact measure of the induced motion of the nacelle from the platform.

The yaw motion in Figure 83 is particularly distinct for the larger seastate, which is most likely attributed to the fact that the yaw natural frequency of 0.63 Hz is relatively close to the peak frequencies of sea state 6, 7 and 8. The remaining curves are quite steep indicating that the yaw motion is less sensitive to the wave height of the incoming wave.

3.10.2 The effect of wind forcing and wind damping

The wind forcing obviously provides an additional forcing of the turbine and platform motion. The rotor motion, however, is also know to provide aero-dynamic damping of wave-induced motion. For this reason, the effect of added wind forcing is interesting to study and is one of the main arguments for carrying out the tests in combined wind and waves.

The present analysis is based on sea state 5, since the thrust force is at a maximum here. The impact from the wind damping is therefore expected to be more pronounced at this sea state.

In the results for the irregular waves the mean value of the response has been subtracted from the results to ease the identification of discrepancies in the results due to the presence of wind and not due to differences in the equilibrium positions. Throughout this section black curves represent the response with no wind present and the blue curve represents the response at rated wind speed.

(a) Surge   (b) Pitch
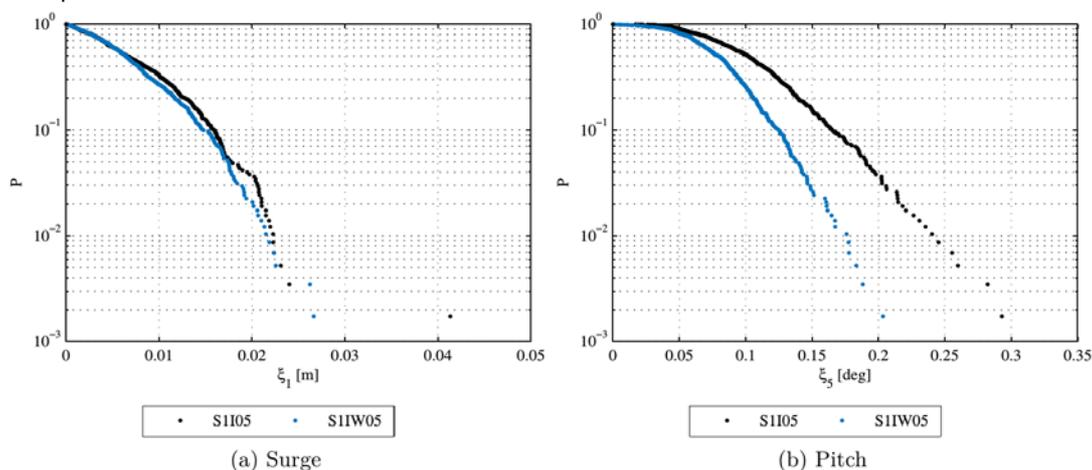
Figure 84- Motion of structure 1 in the irregular sea states 5 for $\overline{\Theta} = 0°$ with and without wind

In Figure 84, the platform surge and pitch motion are presented. It is evident that the surge motion is only slightly reduced when wind is applied. A much larger impact of wind damping is evident in

INNWIND.EU D4.2.4: Floating Wind Model Tests at ECN and DHI

the pitch response, where the pitch motion is consistently lower for the test with wind. The results of Figure 84 indicate that the damping has a greater effect on the large motions motions, leading to a pitch curve which drops more quickly compared to the no wind pitch curve. The most extreme pitch angles are decreased by around 40 %.

The effect of wind forcing on the sway, heave, roll and yaw motion is analysed in [16]. Here, also for structure 1, it is found that

- The sway motion is increased about 50 % when wind is applied. This is increase is very likely due to rotor imbalances or a skewness in the wind field.
- The heave motion increases. This can be linked to the change of equilibrium position away from completely vertical tendons, leading to stronger surge-induced heave motion. Rotor imbalances may also play a role here.
- The roll motion is generally reduced when wind forcing is added. This is surprising, since the sway motion was found to increase. The reduced roll motion might thus indicate sideways aerodynamic damping.
- The yaw motion is significantly increased with wind applied. This is linked to rotor imbalances, deviation from uniformity in the flow and yaw-forcing through combined roll-thrust action.

The acceleration in the nacelle is presented in Figure 85.

(a) Nacelle acceleration in x (b) Nacelle acceleration in y
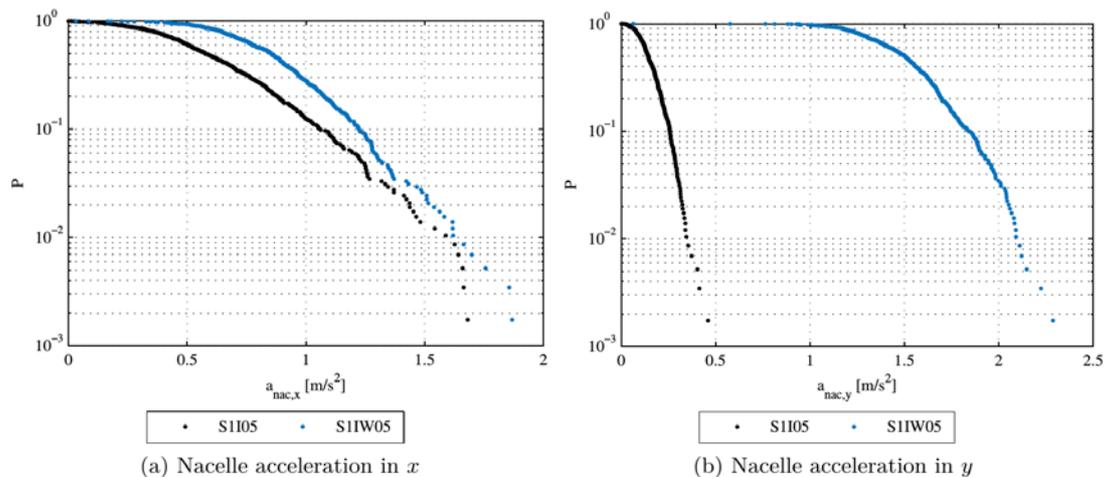
Figure 85 - Nacelle acceleration of structure 1 in the irregular sea states 5 for $\overline{\Theta} = 0°$ with and without wind

The acceleration in the nacelle increases in the x-direction as wind is applied. Previously it was established that the surge and the pitch motion decreases as wind is applied. This indicates that the increase in accelerations is caused by the motion of the rotor. The strong increase in the acceleration of the nacelle in the y-direction with wind indicates that the rotor is not fully balanced in the rotating parts. The offset of the probability curve for the wind case starting at around 0.5 m/s^2 in x and 1 m/s^2 in y provides further evidence for the existence of a baseline nacelle acceleration solely due to the rotation of the rotor. Variations in the wind flow could also be contributory to the excitation of in particular the acceleration in x. Comparison with numerical model simulations are currently planned to investigate these effects further.

3.10.3 The difference in motion response for structure 1 and 2

The motion of structure 1 (vertical tendons) and structure 2 (inclined tendons) is quite different. While vertical tendons leads to very limited platform pitch, inclined tendons enforce a negative pitch for positive surge and vice-versa, as shown in Figure 86.

Structure 1   Structure 2
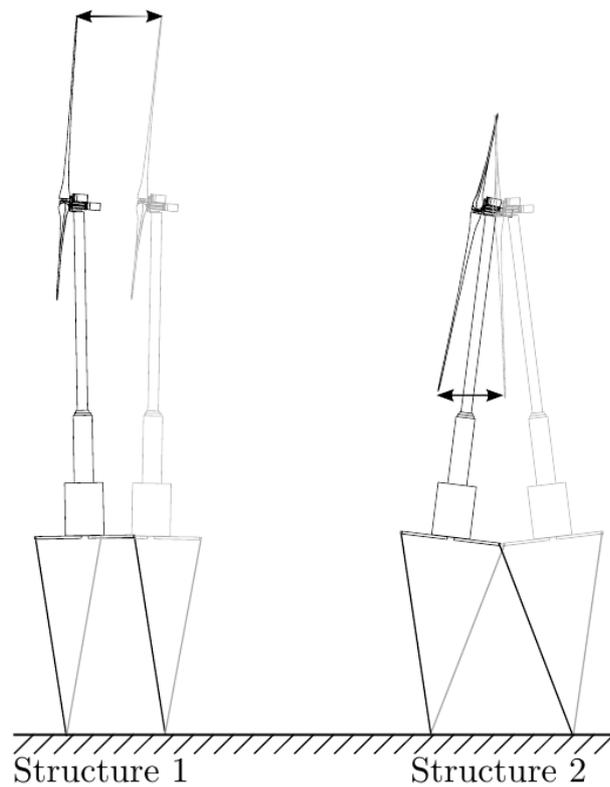
Figure 86 – Motion pattern of structure 1 and 2

In Figure 87 the surge and pitch motion is presented as exceedance probability plots for sea state 5 with and without wind.

(a) Surge   (b) Pitch
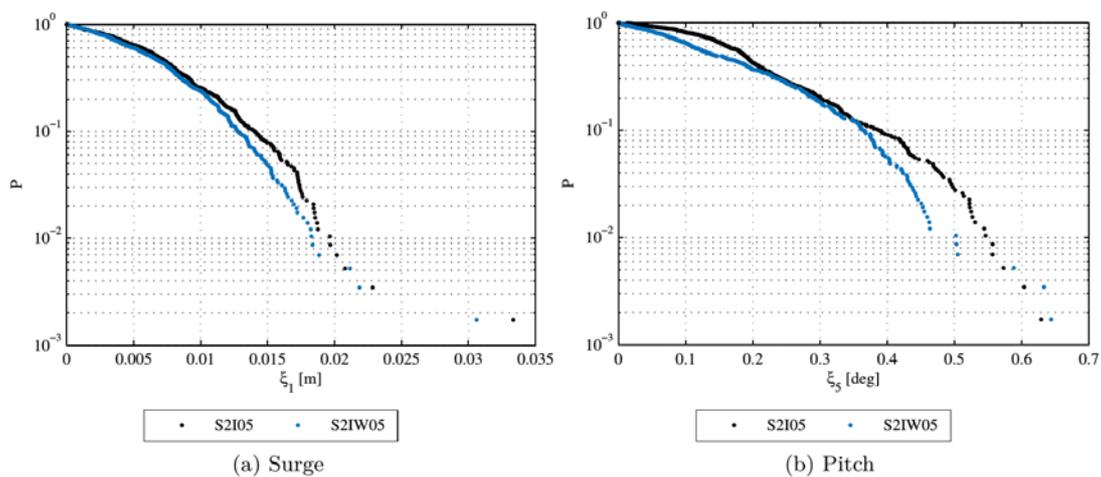
Figure 87 - : Motion of structure 2 in the irregular sea states 5 for $\overline{\Theta} = 0°$ with and without wind

INNWIND.EU D4.2.4: Floating Wind Model Tests at ECN and DHI

By comparison to Figure 84 (structure 1), it is seen that the surge responses for the two structures are similar for the case of no wind. The pitch motion, however, is much stronger for structure 2, due to the surge-pitch coupling of inclined tendons. The damping effect from wind on surge is quite similar for both structures too, while for the platform pitch, the wind-damping is less pronounced for structure 2. This is expected since the pitch motion of structure 2 is driven by the displacement in surge of the floater, opposed to structure 1 which is driven by nacelle displacement in relation to the floater surge. Since the nacelle has a greater displacement for structure 1 and hence expected to have a greater velocity, it is also expected that damping will have greater impact on structure 1.

(a) Nacelle acceleration in x (b) Nacelle acceleration in y
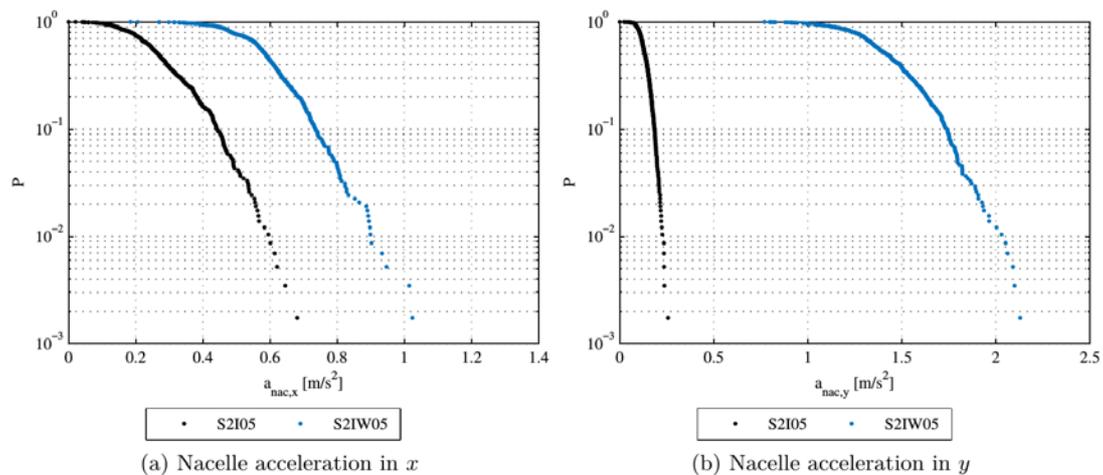
Figure 88 - Nacelle acceleration of structure 2 in the irregular sea states 5 for $\overline{\Theta} = 0°$ with and without wind

The acceleration of the nacelle is presented in Figure 88 that includes results with and without wind. The coresponding curves for structure 1 are provided in Figure 85. For no wind (black curves) the x-accelerations are 2-3 times smaller for structure 2 and also smaller for the y-acceleration. Addition of wind forcing leads to stronger x-accelerations for both structures, but most pronounced for structure 2. The y-accelerations are increased by a similar amount. As previously stated the nacelle motion of structure 2 is smaller, and therefore the effect of the induced vibrations from the rotor and the transmission mechanism will become more apparent.

A common trend in the acceleration signal in x for structure 1 and 2 is the offset in accelerations between no wind and with wind situations, indicating that the presence of wind causes a constant amplification of the acceleration.

3.10.4 The effect of 3D wave spreading on nacelle acceleration

2D waves are often used in model tests due to their reduced complexity and the subsequent ease of analysis. Ocean waves, however, are 3 dimensional, and it is therefore of great interest to determine which effect that might be missing, when conducting experiments in 2D wave climates. Here a comparative analysis of results for sea state 8 are presented. This is the largest sea state and the effects are therefore expected to be most pronounced. In order to single out the effect of having 3D waves the results from the tests with no wind are presented. Throughout this section the black curves represent the response in the unidirectional wave climate for $\Theta = 0°$, whereas the blue curves are the response in spread waves.

Ideally the wave climates are supposed to be comparable in terms of wave height at the location of the model, however as detailed in [16] the waves in the 3D wave climate are consistently smaller in magnitude up to the 97 % quantile, whereupon the two wave climate are comparable, ending with a couple of extra large waves for the 3D wave climate. This must be remembered when the results are interpreted.

(a) Nacelle acceleration in x (b) Nacelle acceleration in y
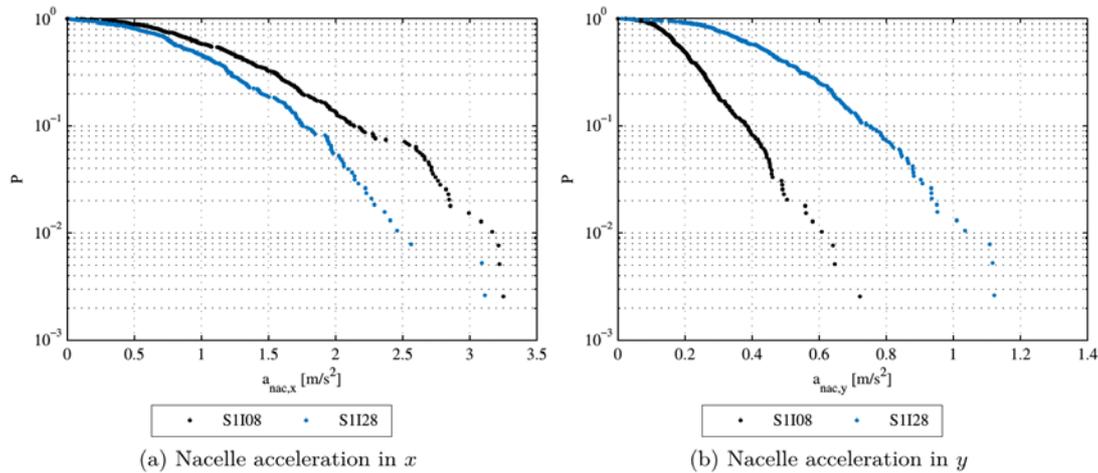
Figure 89 - Nacelle acceleration of structure 1 in the irregular sea state 8 with no wind for $\overline{\Theta} = 0^{\circ}$ and for spread waves

The acceleration of the nacelle is presented in Figure 89. The x - acceleration agrees with the decreased pitch motion of the model in 3D waves. Likewise the increase in acceleration in the y - direction for 3D waves is a result of the increased sway and roll motion. Moreover the fluctuation in the tendon tension for all three structures is lower in the 3D wave climate [16]. Hence conservative values for the pitch motion and the tendon tension are obtained when modelling in a 2D wave climate, whereas (see [16]) the yaw and in particular the sway and roll motion are underestimated.

3.10.5 The effect of wind-wave misalignment on the nacelle-accelerations

The change in response was investigated for the case where the wave direction and the wind direction are misaligned by an angle of 30°. This was accomplished by changing the wave heading angle to $\overline{\Theta} = 30^{\circ}$. Attention will in particular be given to changes in the wind damping.
To enable an appropriate comparison of the response for different wave heading angles it is requisite to consider the motion in a rotated coordinate system which is aligned with the wave heading direction. In the case of misaligned/oblique waves the surge and sway motion can be projected onto the rotated coordinate axes (x_{obl}, y_{obl}) by taking the dot product between a unit vector along the axes of the rotated coordinate system and the surge and sway motion in the original coordinates.

$$\xi_{1,obl} = \begin{Bmatrix} \xi_1 \\ \xi_2 \end{Bmatrix} \cdot \begin{Bmatrix} \cos(30°) \\ \sin(30°) \end{Bmatrix}$$

(17)

INNWIND.EU D4.2.4: Floating Wind Model Tests at ECN and DHI

$$\xi_{2,obl} = \begin{Bmatrix} \xi_1 \\ \xi_2 \end{Bmatrix} \cdot \begin{Bmatrix} -\sin(30°) \\ \cos(30°) \end{Bmatrix}$$

(18)

The roll and pitch motion angles are assumed to be small and hence the transformation of the roll and pitch motion is conducted by the transformation of a reference point at the tower 1 meter above the point of flotation to the oblique coordinate system.

$$\xi_{(15),obl} = \begin{Bmatrix} \xi_1 + \sin(\xi_5) \\ \xi_2 - \sin(\xi_4) \end{Bmatrix} \cdot \begin{Bmatrix} \cos(30°) \\ \sin(30°) \end{Bmatrix}$$

(19)

$$\xi_{(24),obl} = \begin{Bmatrix} \xi_1 + \sin(\xi_5) \\ \xi_2 - \sin(\xi_4) \end{Bmatrix} \cdot \begin{Bmatrix} -\sin(30°) \\ \cos(30°) \end{Bmatrix}$$

The computation is reversed in order to get the pitch and roll motion of the model in the oblique coordinate system.

$$\xi_{4,obl} = \arcsin(\xi_{(24),obl} - \xi_{2,obl})$$
$$\xi_{5,obl} = \arcsin(\xi_{(15),obl} - \xi_{1,obl})$$

(20)

A similar transformation is conducted for the nacelle acceleration signal, and throughout this section, the model motion will only be considered in a rotated coordinate system for tests with oblique waves. The rotation of the coordinates does not effect the heave or yaw motion as well as the tendon tensions.

To illuminate any discrepancies in the response caused solely by the change of wave heading angle, the response in the cases of no wind for $\overline{\Theta} = 0°$ to $\overline{\Theta} = 30°$ are included in the analysis. Since the impact from the thrust force is largest for sea state 5, this sea state forms the basis for the analysis of misalignment of wind and waves. To compare and highlight the differences of the platform response and the nacelle accelerations for wind and no-wind tests, the mean is subtracted from the signals before they are presented.

(a) Nacelle acceleration in x

(b) Nacelle acceleration in y
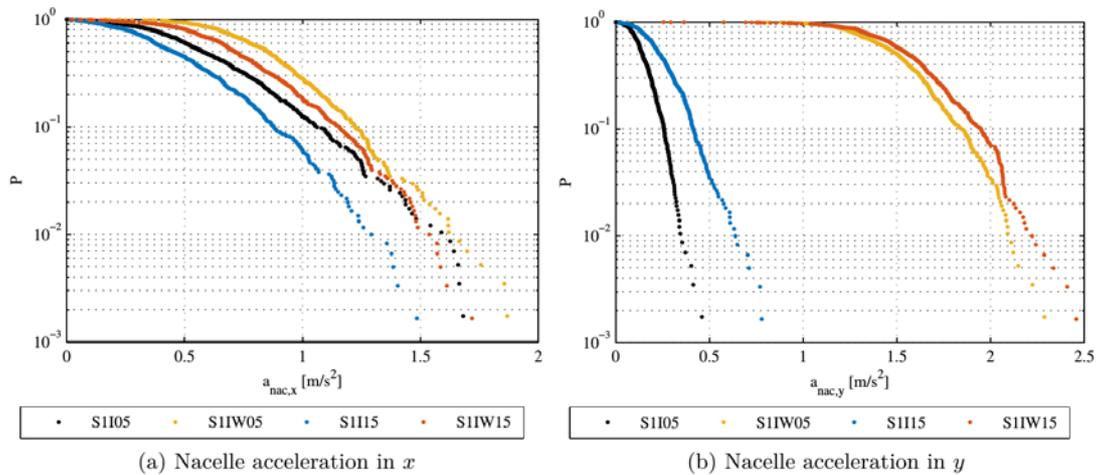
Figure 90 - : Nacelle acceleration of structure 1 in the irregular sea state 5 for $\overline{\Theta} = 0°$ and $\overline{\Theta} = 30°$ with and without wind

The nacelle accelerations presented in Figure 90 show that the change in wave heading angle (black to blue) entails a corresponding decrease in the x-acceleration, and an increase in the acceleration in the y-direction.

Next, the effect of added wind can be studied. For a wave heading of 0 degrees, addition of wind (black to yellow) leads to increased x-accelerations. The same occurs for a heading of 30 degrees (blue to red), but the change is larger. This is consistent with the smaller aero-dynamic damping in the wave-direction for a 30 degree misalignment. For the y-acceleration, added wind leads to stronger accelerations in the case of 0 degree heading (black to yellow) and 30 degree heading (blue to red). The increase, however, is smaller in the latter case where the wind and waves are misaligned. This is consistent with the existence of aerodynamic damping for the cross-wave direction in the misaligned case. The results for acceleration in mis-aligned conditions therefore supports the expectation of reduced damping in the main wave direction and increased damping in the cross-wave direction.

3.10.6 Platform response and nacelle accelerations for an extreme wave event

Extreme wave events have been studied in terms of focused wave groups. The focused waves were generated following the New Year Wave theory. An example of surge, pitch and acceleration response for a focused wave belonging to sea state 8 is shown in Figure 91. All measurements are presented in their time series to the left and with the corresponding power spectrum to the right.

INNWIND.EU D4.2.4: Floating Wind Model Tests at ECN and DHI
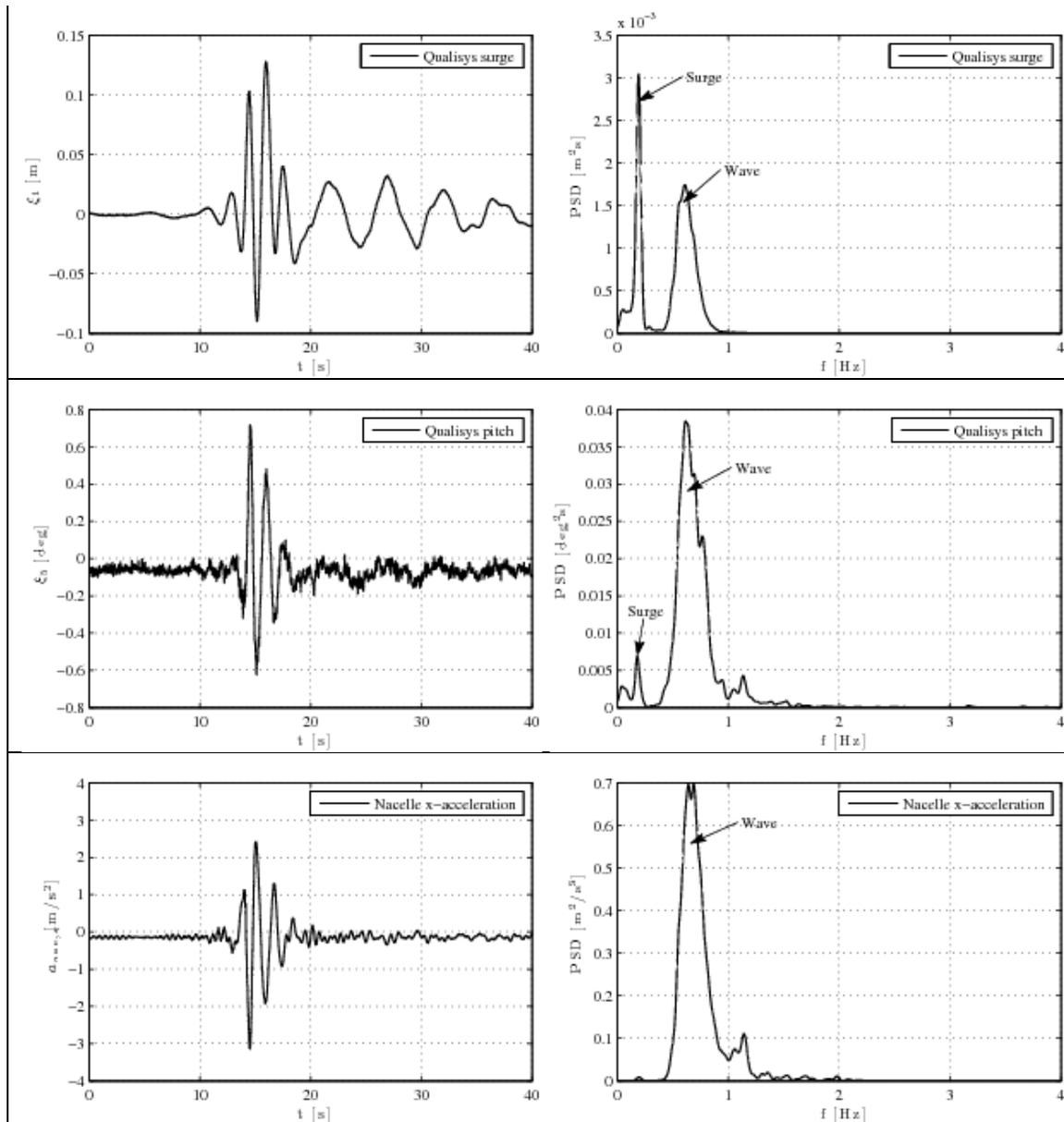
Figure 91 - Response of structure 1 to focused wave number 8 without wind (S1F08). From top to bottom: Surge, Pitch and Nacelle x-acceleration. Left column: time series. Right column: Power spectra.

The maximum surge peak response is obtained after the passing of the wave that follows the largest peak surface elevation. It can be seen that the platform after the passage of the wave group moves at its natural surge frequency. The structure has thus been excited by the wave group.

After the passing of the primary wave group, a weak surge frequency component is evident in the pitch response, and a corresponding peak in the spectrum is observed. Here it is also observed that the models pitch frequency is not excited by this wave, as opposed to focused wave number 5, see [16]. However, a small peak is observed at f=1.2 Hz, to which the most likely explanation is that it lies within the peak of the excitation force computed in WAMIT [16]. With a large wave excitation force, noticeable response can be observed despite a modest level of wave energy at this frequency.

This effect is also felt in the nacelle x-acceleration that shows a peak at 1.2 Hz.

INNWIND.EU D4.2.4: Floating Wind Model Tests at ECN and DHI

4. ISOLATED MOORING LINES TESTS

A set of tests with an isolated mooring line have been performed at the *LHEEA - Research Laboratory in Hydrodynamics, Energetics and Atmospheric Environment* of the Ecole Centrale de Nantes (ECN). The objective of these tests is to obtain a detailed database of the dynamic behaviour of a mooring line for the validation of dynamic mooring lines simulation codes and the adjustment of simulation models, for instance tuning the chain drag coefficients.

The tests consisted of a suspended chain submerged into a water basin. Two initial configurations of the chain, with different tension levels, were studied. The suspension point of the chain was excited with a prescribed harmonic motion with diverse periods. The tension at the suspension point and the motion of several point along the line length have been measured.

4.1 Lay-Out of the Experiment and Reference System

The chain was installed into the basin, submerged in water, forming a catenary shape with one of the ends anchored to the bottom of the tank and the upper one connected through a load cell to a mechanical actuator located at the water free surface.

Figure 92 shows the configuration of the experiment. During the test, the anchor remains fixed at the bottom of the basin, at a depth of 5m, and the upper end, located at the water plane, is excited by the mechanical actuator with a sinusoidal prescribed horizontal motion in the plane of the catenary, around a mean position. The distance d is the horizontal distance between the anchor and the mean position of the upper end during the tests. Two different configurations of the mooring chain have been tested. In the Configuration 1, the distance d is 19.364m and in the Configuration 2 d is 19.870m. The Figure also shows the reference system used to present the results.

INNWIND.EU D4.2.4: Floating Wind Model Tests at ECN and DHI
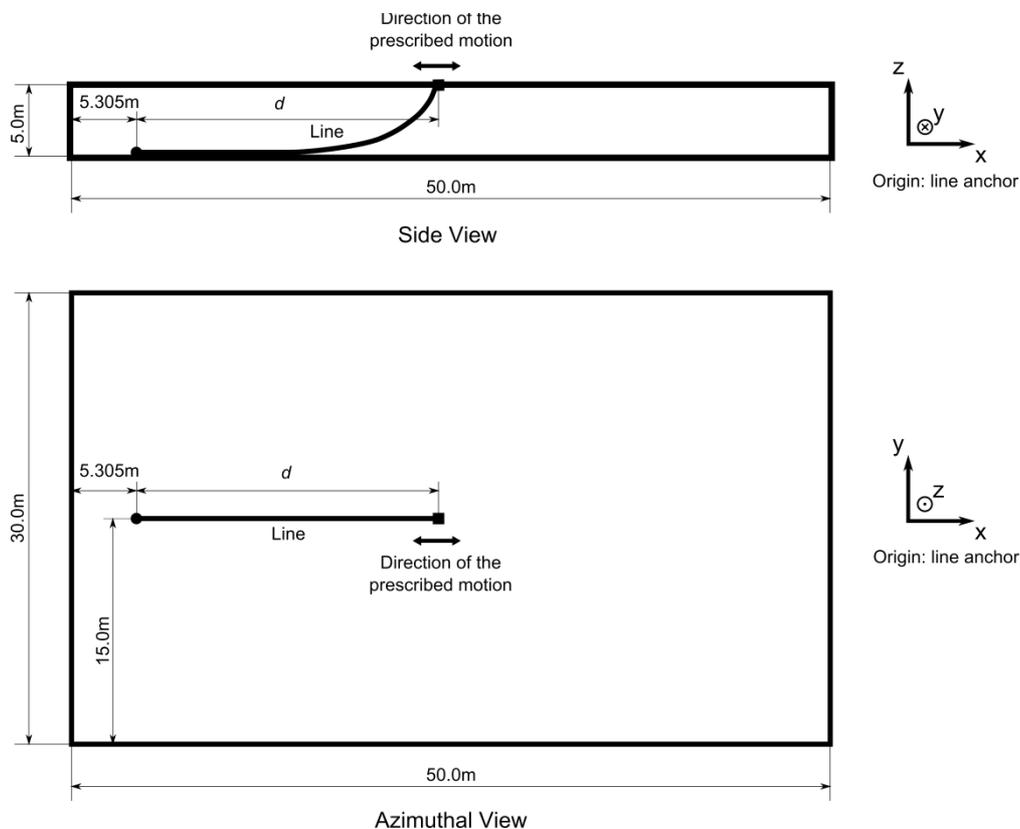
Figure 92 - Configuration of the Experiment and Reference System

4.2   Characteristics of the chain tested

The steel chain selected for the tests is a DIN5685A design with a link diameter of 2 mm. The length of the chain including the load cell at the fairlead is 21m. Some preliminary simulations have been performed in order to confirm that the presence of the load cell has not an important impact on the tension and dynamics of the chain. The mass per unit length was measured and a value of 69g/m was found, though the original manufacturer specification was 70g/m.

This chain model was chosen because the resulting full scale mass scales by an approximate factor of $1/40^2$ when compared to the properties of the OC4 floating model mooring lines [14]. With a scale factor of $1/40$, the 5m depth of the basin represents a 200m depth sea location. Therefore, this chain represents a typical scaled mooring line used in wave tank tests for floating wind turbines.

As has been mentioned the measured weight per unit length of the chain is 69g/m and the length is 21m. As many computational model the moorings as a line with a constant circular section, an equivalent hydrodynamic diameter has to be determined. To do this, the volume of the total length of the chain was measured and the diameter of the circular section
that provides that volume for the same length was calculated assuming that the material density (steel) had a value of 7850kg/m³. The resulting hydrodynamic equivalent diameter was 0.0034. This value is provided here to be used by modellers if they find it useful.

4.3 Lay-Out of the Experiment and Reference System

First, two static cases with the chain suspension point fixed corresponding to Configuration 1 and Configuration 2 are studied. In addition, 6 dynamic cases are simulated combining the 2 chain configurations with three different oscillation periods of the motion imposed at the fairlead. Similar criteria based on scale factors used for the chain dimensions were also used in the selection of the excitation periods of 1.58s, 3.16s and 4.74s. These periods correspond to oscillation periods of 10s, 20s and 30s in full scale when a 1/40 scale factor is used. As a matter of fact, a typical surge period of a moored platform is 10s or higher. The cases that have been considered are described in Table 40.

Table 40 - Description of the Test Cases

Case ID	Configuration	Anchor-Fairlead Mean Distance d (m)	Amplitude (m)	Period (s)
ML1	1	19.364	Static	
ML2	2	19.872	Static	
ML3	1	19.364	0.25	1.58
ML4	1	19.364	0.25	3.16
ML5	1	19.364	0.25	4.74
ML6	2	19.872	0.25	1.58
ML7	2	19.872	0.25	3.16
ML8	2	19.872	0.25	4.74

During the dynamic tests, the position of 8 reflecting markers located at different chain positions and the tension at the fairlead of the chain were measured.
The distance between two adjacent reflecting markers along the chain is approximately 0.5m. The exact position of these markers is provided in Table 41.

Table 41 - Position of the markers

Marker number	Fairlead position along the line (m)
1	0.656
2	1.155
3	1.655
4	2.149
5	2.646
6	3.152
7	3.655
8	4.164

For the static cases (cases 1 and 2), in addition to the markers in Table 2, the positions of 4 additional reflecting markers located at 180 the lower part of the chain were also monitored. The distance between these additional reflecting markers was also 0.5m approximately. The fairlead static tension was also measured.

INNWIND.EU D4.2.4: Floating Wind Model Tests at ECN and DHI

4.4 Acknowledgements

INNWIND.EU D4.2.4: Floating Wind Model Tests at ECN and DHI

5. DATABASE OF MEASUREMENTS

The measurement raw data is available in six different data files. These contain the wind and wave information and the 3D camera system by Ecole Centrale de Nantes, the measurements of the Froude-scaled wind turbine, the measurements of the platform, the fairleads sensors and accelerometers and the ducted fan measurements and results of the internal FAST simulation.

During all experiments log files have been written manually with an identifier of the test run, the exact date and time of the experiment and the name of the different data files.

The complete set of data including the tools to collect the data from all data loggers and the model and test description can be downloaded from a central webserver by all project partners. If agreed by the consortium this webspace can be made available for the public.

The address of the webspace is:

http://www.ifb.uni-stuttgart.de/windenergie/download_messdaten.en.html

5.1   Collection of all data files

An index file "DataIndex_INNWIND_ECN1409.xlsx" contains information on the sensors, (e.g. calibration factors, corresponding data file, sampling rate, etc.) the data files (e.g. header lines, separators) and the test runs (e.g. time, identifier, filenames). Based on this information all data is read in by the Matlab function "INNWINDReadData.m", which stores the data in a structure including all attributes defined in the Excel file. The data of each test run is then stored in individual Matlab files (.mat), see Figure 93. The data in these Matlab files is still not converted by the calibration functions but they are available as function files for each sensor. Thus, the calibrated data is not stored but can be converted directly by applying the corresponding calibration function. Up to four different calibration functions can be specified in the index file.

For the ducted fan test cases in week4 only three measurements, additionally to the wind, wave and Qualisys measurements are given: The tower base fore-aft and side-side moments and the commanded thrust force. However, the data files of the internal FAST simulations are available and can be used for further studies. The SIL_Interface file is a file where we store the value of several variables interchanged between the test and the software: measured motion, demanded thrust to the fan computed by the simulation, etc. We also store some control parameters (as the computational time of each time step) and the measurements of the tower base sensors. The time column is in full scale.
The "Time Delay File" specifies the time delay between measurements and simulation. As the trigger to start measuring data was not able to start running the FAST simulation, we had to start the simulation "by hand" once all the sensors were already measuring. This produced a certain delay between the time column of all the files with measured signals and the FAST_Output and SIL_Interface time columns. To register this time delay, we stored in this file the time of the trigger and the time the simulation starts.

5.2   Using the plot function

Place all Matlab functions in the working directory, if available, store all matlab-files with the collected data in a subfolder "CollectedData". Run INNWINDReadData(IndexFilePath, TestRunIndx , 0) from Matlab. The index (Excel) file is read again, so changes in the calibration function will be visible in the plots.

5.3 Exporting the data

The collected data in the Matlab (.mat) files can be exported to ASCII files when using the export flag. Run INNWINDReadData((IndexFilePath, TestRunIndx, 1) to export the data of the test run with the given index and leave for your annual vacation in the meantime...
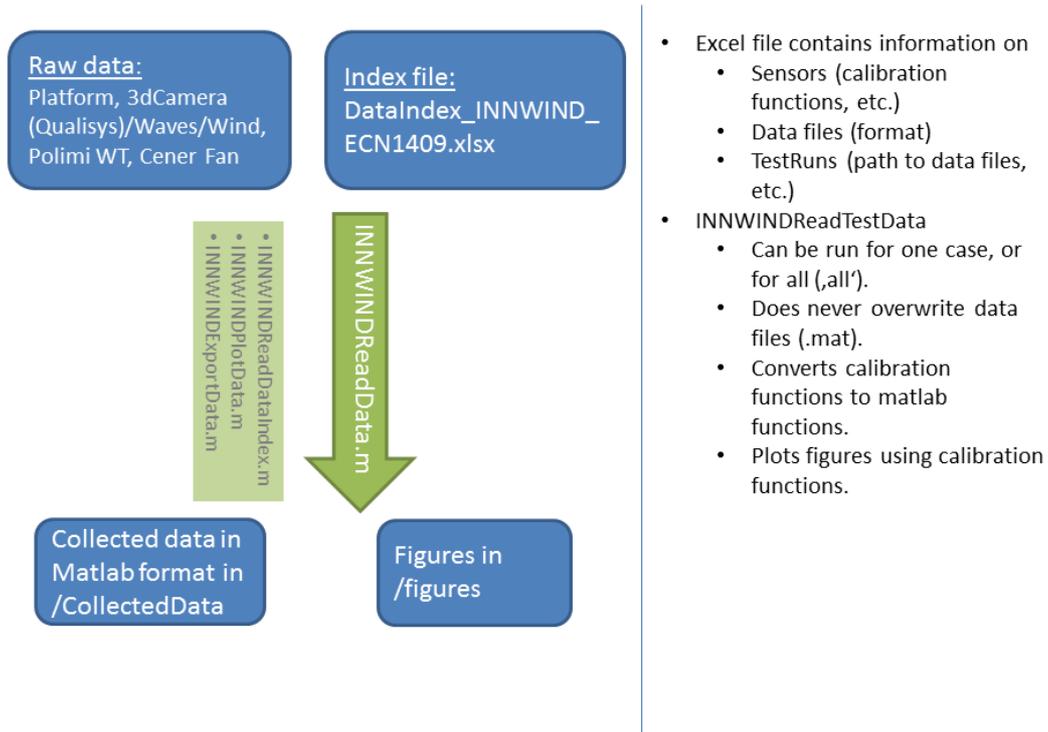
Figure 93 – Database setup and postprocessing

INNWIND.EU D4.2.4: Floating Wind Model Tests at ECN and DHI

6. CONCLUDING REMARKS

This document provides a detailed and comprehensive description of several test campaigns performed within the INNWIND.EU project. These test campaigns include the testing of the INNWIND 10MW wind turbine mounted on two different floating platforms. One of them is a semisubmersible floating substructure and the other one is a TLP platform with three different configurations for the mooring system. The testing of an isolated mooring line on a wave tank is also presented.

The document discuss in detail the scaling methodology applied to obtain a realistic representation of the different forces involved in the dynamics of floating platforms. The scaling of the rotor aerodynamic loads is a technical challenge in tests that combine wind and waves, due to the conflict between the scaling rules based on the Froude and the Reynolds numbers. Two approaches to include the realistic aerodynamic thrust have been implemented: a ducted fan located at the tower top that introduces the force computed by a real time simulation of the rotor and a Froude scaled rotor design.

A very detailed description of the design methodology of the Froude scaled rotor is given, including details on the manufacturing of the blades. This methodology uses the Blade Element Theory (BEM) for the computations of the rotor aerodynamics. NTUA has performed an independent analysis of the performance of the resulting scaled rotor designed by POLIMI using higher complexity CFD tools. The results have been positive, concluding that the design method is adequate and the scaled model correctly represents the target characteristics of the full scale rotor.

The Froude scaled rotor needs a certain equipment as the pitch actuators and the sensors, that increases the resulting weight and may be a limitation for matching the target tower top weight of the full scale rotor when low scale factors are applied. For this reason, the development of lighter Froude scaled rotor has to be pursued. The ducted fan system results in a lower tower top weight and this limitation is less likely to appear. In fact, adding ballast to the tower top was required for this test campaign when using the ducted fan.

The building of the platform is documented, including the materials that have been used for the different components. The matching of the target inertial properties requires a careful design of the scaled platform and also a verification of the resulting properties. The sensors included in the scaled platform can influence the dynamics noticeably, for this reason their masses, inertias and locations should be considered on the design phase. The use of a CAD model, which was updated constantly during the building phase, has been very useful. This analytical tracking of the properties was complemented with an experimental verification: experimental pendulum tests of the scaled platform once the building was finished confirmed the achievement of the objective properties.

Before performing the test cases using wind generators and the Froude scaled rotor model, an accurate evaluation of the wind flow created by the wind generator system is very important for a correct understanding of the results. In a wave tank the wind flow is injected by the generator system within a volume of steady air and high turbulence can be produced in the boundaries of the flow. In the test campaign presented in this document, the flow field has been carefully studied experimentally and computationally to understand the distribution of the wind speed and the turbulence in the space and how they interact with the rotor.

Typically, the undisturbed wind speed (understood as the wind speed at a distance upwind far enough not to be affected by the presence of the wind turbine) is taken as the reference wind speed. Nevertheless, when performing tests at a wave tank, the wind flow is generated by a system of fans and the definition of the reference wind speed has to be changed. The solution adopted in this research was to measure the wind speed at the location of the wind turbine and then adjust the pitch of the blades to achieve the desired C_T-λ **relationship**.

Many details on the building of a wind generator system for the DHI wave tank have been provided in the chapter related to the TLP test campaign. The building of this system from scratch was necessary, because the facilities were not equipped with such a system. Instead of installing one large wind generator, six smaller units were used. This option facilitated the test and construction of the system. A very compact solution was obtained introducing a corner section where the flow is turned 90º.

The setup of the sensors for the measurements and how they have been calibrated are provided. Particular attention is paid to the Qualisys system. This system acquires the motions of the platform using cameras that track a set of reflecting markers fixed at the platform. Some general criteria to setup this system and to choose the distances between markers are provided. It is also explained how the sampling frequency has been selected. To ensure a proper resolution of the data, the Nyquist criterion has to be obeyed. This criterion states that the sampling frequency must be at least twice the higher frequency present in the signal. The frequency of the alternating current should also be resolved and, at the same time, it should be kept in mind that the sampling frequency should not be divisible by the frequency of the alternating current.

A description of the test cases defined in the test campaigns is provided. The test campaign definition follows an increasing level of complexity on the tests to allow the stepwise identification of the different phenomena involved. The cases include regular, irregular and focused waves, cases with wind only and waves only and also combinations of waves and wind.

A preliminary presentation of some of the most relevant results of the tests campaigns is given in the report. Comparisons of the dynamic behaviour of the TLP platform with different configurations of the mooring system (including tendons perpendicular and not perpendicular to the seabed) under the same environmental conditions are shown. The comparison of probability exceedance plots reveals how the different configurations can greatly affect the motions of the platform and the accelerations of the nacelle. Comparisons of cases with wind and without wind and the same sea state shows the importance of the aerodynamic damping on the surge and pitch motions.

The test campaigns presented in this deliverable have been thoroughly documented and they cover two of the main concepts of floating wind turbines (semisubmersible and TLP) for a large 10MW wind turbine. In addition, the test campaign on the isolated mooring line provides a comprehensive measurement database of the behavior of a submerged line under different dynamic conditions. The measurements are unique because they include not only tension data but also measurements of the underwater motion of the chain at different positions.

Finally, it has to be highlighted that a very complete database is provided and has been made available online. This database is an important contribution to the INNWIND.EU project and provides very valuable information for the research on floating platform dynamics and for the validation of the simulation tools.

7. ANNEXES

7.1 Annex 1: Scaling laws used in the test campaigns

This Annex presents a Froude scaling methodology for model tests in simultaneous waves and wind.

When setting up a model experiment, the aim is to have dynamic and elastic similarity between the model and its prototype. The motion of a rigid body in a fluid, is generally governed by inertial forces, gravitational forces and viscous forces, and to obtain full dynamic similarity, the ratio of these forces must be conserved. This can be expressed as a preservation of the Froude number defined as the ratio of inertial forces to gravitational forces

$$Fr = \frac{\text{Inertial force}}{\text{Gravitational force}} = \frac{u}{\sqrt{gl}} \tag{21}$$

and the Reynolds number which is defined as the ratio of the inertial forces to the viscous forces:

$$Re = \frac{\text{Inertial force}}{\text{Viscous force}} = \frac{ul}{\nu} \tag{22}$$

where u is a characteristic velocity, l is a characteristic length, g is the acceleration of gravity and ν is the kinematic viscosity. Generally it is not possible to preserve both in model tests which represent a significant change in the length scale, which is clearly observed by considering the ratio of the Reynolds number to the Froude number,

$$\frac{Re}{Fr} = \frac{\sqrt{g}\sqrt{l^3}}{\nu} \tag{23}$$

As a consequence of the constant Re and Fr, this quantity must also be preserved, requiring either a substantial change in the acceleration of gravity or the fluid viscosity, but neither are considered possible for model tests ([35] p. 5). Surface waves are primarily governed by Fr, and hence it has become tradition to preserve this number in model tests of offshore structures and floating bodies, and this methodology will also serve as a starting point for the scaling of the wind turbine model in the present work.

Further, for a flexible structure, it is desired to scale it elastically, such that the natural frequencies of the model scale like the frequencies of the environment.

This section follows the authors' own work published in [22] and is consistent with Bredmose et al. [20] and Martin et al. [28], although the latter does not take into account the difference in prototype and model scale water density.

The geometric scaling factor, λ, is defined by

$$\lambda = \frac{l_p}{l_m} \tag{24}$$

where subscripts p and m refer to prototype and model lengths respectively. The ratio of gravitational force and buoyancy must be maintained, corresponding to preservation of the ratio of the structure mass to the mass of displaced water, such that

$$\frac{m_p}{\rho_{wp}\forall_p} = \frac{m_m}{\rho_{wm}\forall_m} \quad \Leftrightarrow \quad \frac{m_p}{m_m} = \frac{\rho_{wp}}{\rho_{wm}}\lambda^3 \tag{25}$$

where m is the wind turbine mass, ρ_w is the water density and $\forall$ is the displaced water volume. The displaced water mass is $\rho_w\forall$.

Further, the ratio of inertia forces to gravitational forces must be maintained. By virtue of (25) and for a cross sectional area $\tilde{A}$, this can be written

INNWIND.EU D4.2.4: Floating Wind Model Tests at ECN and DHI

$$\frac{\rho_{wp}\tilde{A}_p u_{wp}^2}{\rho_{wp}\forall_p} = \frac{\rho_{wm}\tilde{A}_m u_{wm}^2}{\rho_{wm}\forall_m}$$

(26)

corresponding to the aforementioned conservation of Fr

$$Fr_m = Fr_p \quad \Leftrightarrow \quad \frac{u_m^2}{gl_m} = \frac{u_p^2}{gl_p}$$

(27)

since $\dfrac{\tilde{A}_p}{\forall_p} = \dfrac{1}{l_p}$ and $\dfrac{\tilde{A}_m}{\forall_m} = \dfrac{1}{l_m}$. This leads to the scaling of velocity

$$\frac{u_{wp}}{u_{wm}} = \lambda^{1/2}$$

(28)

Further, the scaling of time is determined from the requirement that the travelled distance in a given time must scale as the geometric length

$$\frac{u_{wp}t_p}{l_p} = \frac{u_{wm}t_m}{l_m} \quad \Leftrightarrow \quad \frac{t_p}{t_m} = \lambda^{1/2}$$

(29)

Hence, the frequencies must scale like

$$f_p = \frac{1}{t_p} = \lambda^{-1/2}\frac{1}{t_m} = \lambda^{-1/2}f_m$$

(30)

which apply to the forcing of in the prototype environment and the model environment as well as to the structural natural frequencies for the prototype and the model.

The rotor aerodynamics are mainly governed by Re, and due to the large dissimilitude in Re, a geometrical scaling of the rotor will not give the correct aerodynamic performance of the blades. This will lead to a reduction in the aerodynamic thrust and mechanical power, where especially the first is of great importance to the overall dynamics of the structure. Hence, there is a need for a redesign of the rotor in model scale, which is able to deliver the right thrust at the low Re. This was also carried out as a part of the present work and is detailed in section 3.4. To maintain mass and gyroscopic effects, this must be combined with a distribution of mass as determined from the prototype distribution by (25), and ideally the stiffness must be scaled to give the right natural frequencies determined by (30).

The aerodynamic thrust can be expressed as $T = \frac{1}{2}\rho_{\text{air}}C_T A U^2$, where C_T is the thrust coefficient, A is the rotor area and U is the incident aerodynamic velocity. The ratio of aerodynamic thrust force to gravity force must be conserved for dynamic similarity, leading to

$$\frac{\frac{1}{2}\rho_{\text{air}}C_{Tp}A_p U_p^2}{m_p g} = \frac{\frac{1}{2}\rho_{\text{air}}C_{Tm}A_m U_m^2}{m_m g} \quad \Rightarrow \quad \frac{U_p}{U_m} = \sqrt{\frac{C_{Tm}}{C_{Tp}}\frac{\rho_{wp}}{\rho_{wm}}\lambda}$$

(31)

For consistency of wind and wave experimental environments, water and air particle velocities must scale equally like $\lambda^{1/2}$, by which (31) defines the scaling of the thrust coefficient.

$$\frac{U_p}{U_m} = \lambda^{1/2} \quad \Rightarrow \quad \frac{C_{Tp}}{C_{Tm}} = \frac{\rho_{wp}}{\rho_{wm}}$$

(32)

As angular frequency, ω, scales like the frequency, (30), $\dfrac{\omega_p}{\omega_m} = \lambda^{-1/2}$, this scaling method conserves the tip speed ratio, TSR.

$$\text{TSR}_p = \frac{\omega_p R_p}{U_p} = \frac{\omega_m R_m}{U_m} = \text{TSR}_m$$

(33)

INNWIND.EU D4.2.4: Floating Wind Model Tests at ECN and DHI

Based on the scaling of the fundamental quantities of length, mass and time the remaining relevant quantities can be scaled by expression of their units in terms of these fundamental quantities [36]. For force the unit of newton is $N = \dfrac{kgm}{s^2}$, corresponding to:

$$[force] = \frac{[mass] \times [length]}{[time]^2} \tag{34}$$

meaning that the scaling factor for force can be expressed by the factor for mass times the factor for length divided by the squared factor for time:

$$f_p = \Lambda f_m, \quad \Lambda = \frac{\dfrac{\rho_{wp}}{\rho_{wm}} \lambda^3 \times \lambda}{\left(\lambda^{1/2}\right)^2} = \frac{\rho_{wp}}{\rho_{wm}} \lambda^3 \tag{35}$$

Equivalently for bending stiffness, EI [Nm^2], the unit is expressed in terms of the fundamental parameters

$$[bendingstiffness] = \frac{[mass] \times [length]^3}{[time]^2} \tag{36}$$

and the resulting scaling parameter is

$$\{EI\}_p = \Lambda \{EI\}_m, \quad \Lambda = \frac{\dfrac{\rho_{wp}}{\rho_{wm}} \lambda^3 \times \lambda^3}{\left(\lambda^{1/2}\right)^2} = \frac{\rho_{wp}}{\rho_{wm}} \lambda^5 \tag{37}$$

It is noted however, that this method does not hold for the scaling of the dimensionless thrust coefficient as demonstrated above. A number of scaling factors are determined by this methodology and are presented in table 1. These factors are in agreement with results of [36] and [20]. Here it is seen that the acceleration in model scale is equal to the acceleration in prototype scale. The experimental environment and the wind turbine model scale equally, such that e.g. wave height scales like λ and wind speed scales like $\lambda^{1/2}$. This will ensure that the ratio of e.g. floater size to wave height is maintained and that relative velocities are correctly scaled.

8. BIBLIOGRAPHY

[1] J. Azcona, D. Bekiropoulos, H. Bredmose, A. Fischer, N. F. Heilskov, A. Krieger, T. Lutz, A. Manjock, D. Manolas, D. Matha, K. Meister, R. Pereira, J. Ronby, F. Sandner and S. Voutsinas, "INNWIND.EU D4.2.1: State-of-the-art and implementation of design tools for floating structures," 2014.

[2] J. Azcona, F. Sander, H. Bredmose, A. Manjock, R. Pereira and F. Campagnolo, "INNWIND.EU D4.2.2: Methods for performing scale-tests for method and model validation".

[3] A. Robertson, J. Jonkman, M. Masciola, H. Song, A. Goupee, A. Coulling and C. Luan, "Definition of the Semisubmersible Floating System for Phase II of OC4".

[4] K. Müller, F. Sandner, H. Bredmose, J. Azcona, A. Manjock and R. Pereira, "Improved Tank Test Procedures For Scaled Floating Offshore Wind Turbines," in *International Wind Engineering Conference IWEC*, Bremerhaven, 2014.

[5] H. Bredmose, S. E. Larsen, D. Matha, A. Rettenmeier, E. Marino and L. Saettran, "MARINET D2 .4: Collation of offshore wind-wave dynamics," 2012.

[6] F. Amann, "Skalierung, Auslegung und Konstruktion eines Modells einer Schwimmenden Windkraftanlage. Diploma Thesis (in German).," University of Stuttgart/Germany, SWE, 2014.

[7] M. Buhl, "WT Perf User Guide," pp. 1-4, 2004.

[8] C. A. Lyon, A. P. Broeren, P. Gigu`ere, A. Gopalarathnam and M. S. Selig, Summary of Low-Speed Airfoil Data, Vol. 3, SoarTech Publications, 1998.

[9] J. Azcona, F. Bouchotrouch, M. González, J. Garciandía, X. Munduate, F. Kelberlau and T. a. Nygaard, "Aerodynamic Thrust Modelling in Wave Tank Tests of Offshore Floating Wind Turbines Using a Ducted Fan," *Journal of Physics: Conference Series,* vol. 524, p. 012089, #jun# 2014.

[10] J. Jonkman, Dynamics Modeling and Loads Analysis of an Offshore Floating Wind Turbine, 2007.

[11] MIT, "MIT Open Courseware," 2005. [Online]. Available: http://dspace.mit.edu/bitstream/handle/1721.1/35268/13-022Spring-2002/OcwWeb/Ocean-Engineering/13-022Surface-Waves-and-their-Interaction-With-Floating-BodiesSpring2002/LectureNotes/index.htm. [Accessed 9.3.15].

[12] A. Courbois, "Étude expérimentale du comportement dynamique d'une éolienne offshore flottante soumise à l'action conjuguée de la houle et du vent (in French)," 2013.

[13] A. Courbois, O. Flamand, J.-l. Toularastel, P. Ferrant and J.-M. Rousset, "Applying relevant wind generation techniques to the case of floating wind turbines," in *European and African Conference on Wind Engineering*, Cambridge/UK, 2013.

[14] V. A. Riziotis and S. G. Voutsinas, "Modelling of wind tunnel interference on helicopter measurements and assessment of the currently used corrections based on the HeliNovi data base," in *32nd European Rotorcraft Forum*, Maastricht, The Netherlands, 2006.

[15] J. G. Schepers, K. Boorsma, T. Cho, S. Gomez-Iradi, P. Schaffarczyk, A. Jeromin, W. Z. Shen, T. Lutz, K. Meister, B. Stoevesandt, S. Schreck, D. Micallef, R. Pereira, T. Sant, S. A. Madsen and N. Sørensen, "Analysis of Mexico wind tunnel measurements," in *Final report of IEA Task 29, Mexnext (Phase 1)*, ECN-E–12-004, 2012.

[16] R. Laugesen, A. M. Hansen, H. Bredmose, R. Mikkelsen and N. Heilskov, "Experimental Study of the Dynamic Response of the DTU 10 MW Wind turbine on a Tension Leg Platform," *MSc Thesis,* Vols. DTU Wind Energy M-0065, 2015.

[17] H. Bredmose, R. Mikkelsen, A. M. Hansen, R. Laugesen, N. Heilskov, B. Jensen and J. Kirkegaard, "Experimental study of the DTU 10 MW wind turbine," in *EWEA Offshore 2015*, Copenhagen, Denmark, 2015.

[18] E. E. Bachynski, "Design and Dynamic Analysis of Tension Leg Platform Wind Turbines," *PhD thesis,* vol. Norwegian University of Science and Technology, 2014.

INNWIND.EU D4.2.4: Floating Wind Model Tests at ECN and DHI

[19] A. Myhr, C. Bjerkseter, A. Ågotnes and T. A. Nygaard, "Levelised cost of energy for offshore floating wind turbines in a life cycle perspective," *Renewable Energy,* vol. 66(0), p. 714 – 728, 2014.

[20] H. Bredmose, S. E. Larsen, D. Matha, A. Rettenmeier, E. Marino, R. Eichstaedt and L. Saettran, "D2.04: Collation of offshore wind wave dynamics," Marine Renewables Infrastructure Network, 2012.

[21] A. M. Hansen and R. Laugesen, "Experimental study of the dynamic response of a tlp wind turbine," BsC thesis, DTU, 2012.

[22] A. M. Hansen, R. Laugesen, H. Bredmose, R. F. Mikkelsen and N. Psichogios, "Small scale experimental study of the dynamic response of a tension leg platform wind turbine," *Journal of Renewable and Sustainable Energy,* vol. 6(5):053108, 2014.

[23] A. J. Goupee, B. Koo, R. W. Kimball, K. F. Lambrakos and H. J. Dagher, "Experimental comparison of three floating wind turbine concepts," in *31st International Conference on Ocean, Offshore and Arctic Engineering*, Rio de Janeiro, Brasil, 2012.

[24] G. R. Tomasicchio, F. D'Alessandro,, E. Musci, N. Fonseca, S. A. Mavrakos, J. Kirkegaard, G. M. Katsaounis, V. Penchev, H. Schüttrumpf, J. Wolbring and E. Armenio, "Physical model experiments on floating off-shore wind turbines," in *HYDRALAB IV Joint User Meeting*, Lisbon, Portugal, 2014.

[25] G. Kumar and . V. Ramachandran, "A Numerical Model for a Floating TLP Wind Turbine," PhD Thesis, DTU Wind Energy, 2013.

[26] E. E. Bachynski and T. Moan, "Design considerations for tension leg platform wind turbines," *Marine Structures,* vol. 29(1), p. 89 – 114, 2012.

[27] M. O. Hansen, Aerodynamics of wind turbines, Earthscan, 2008.

[28] H. R. Martin, R. W. Kimball, A. M. Viselli and A. J. Goupee, "Methodology for wind/wave basin testing of floating offshore wind turbines," in *31st International Conference on Ocean, Offshore and Arctic Engineering*, Rio de Janeiro, Brazil, 2012.

[29] R. F. Mikkelsen, "The DTU 10mw 1:60 model scale wind turbine blade," DTU Wind Energy.

[30] M. S. Selig, J. J. Guglielmo, A. P. Broeren and P. Giguere, Summary of low-speed airfoil data Vol1, SoarTech Publications, 1995.

[31] P. Giguere, C. P. Ninham, J. J. Guglielmo, M. S. Selig and C. A. Lyon, Summary of low-speed airfoil data, vol 2, SoarTech Publications, 1995.

[32] Fraser , M. S. Selig and X. Donovan, Airfoils at low speed, SoarTech Publications, 1986.

[33] B. Jensen, Internal DHI documentation. DHI, 2015.

[34] K. Johannessen, T. S. Meling and S. Haver, "Joint distribution for wind and waves in the northern north sea," in *Eleventh International Offshore and Polar Engineering Conference & Exhibition*, Stavanger, Norway, 2001.

[35] J. N. Newman, Marine Hydrodynamics, The MIT press, 1977.

[36] A. Jain, A. Robertson, J. M. Jonkman, A. J. Goupee and R. W. Swift, "Fast code verification of scaling laws for deepcwind floating wind system tests," in *22nd International Offshore and Polar Engineering Conference*, Rhodes, Greece, 2012.

[37] A. Robertson, J. Jonkman, F. Vorpahl, W. Popko, J. Qvist, L. Froyd, X. Chen, J. Aycona, E. Uzunoglu, C. Guedes Soares, C. Luan, H. Yutong, F. Pencheng and A. Heege, "Offshore Code Comparison Collaboration Continuation Within Iea Wind Task 30: Phase II Results Regarding A Floating Semisubmersible Wind System," in *Proceedings of the ASME 2014 33rd International Conference on Ocean, Offshore and Arctic Engineering*, San Francisco, USA, 2014.

[38] A. Robertson, A. Goupee, J. Jonkman, I. Prowell, P. Molta, A. Coulling and M. Masciola, "Summary Of Conclusions And Recommendations Drawn From The Deepcwind Scaled Floating Offshore Wind System Test Campaign," in *Proceedings of the ASME 2013 32nd International Conference on Ocean, Offshore and Arctic Engineering*, 2013.

INNWIND.EU D4.2.4: Floating Wind Model Tests at ECN and DHI